

University of Southampton
Faculty of Physical Sciences and Engineering
Physics and Astronomy

Force detection in levitated optomechanics

by

David William Hempston

Thesis for the degree of Doctor of Philosophy

October 2017

University of Southampton

Abstract

Faculty of Physical Sciences and Engineering

Physics and Astronomy

Doctor of Philosophy

by David William Hempston

The use of levitated optomechanical systems as force sensors is a growing field with great potential. This thesis presents a system that achieves a sensitivity of $\approx 10^{-22} \text{ N}/\sqrt{\text{Hz}}$ by using on-resonance forces and an optically levitated nanoparticle in a gradient force trap. It is possible to reach pressures of 10^{-6} mbar and trap particles with diameters of 50 nm to 300 nm. The particle's motion is detected with a homodyne-like detection system that measures the phase difference in the scattered and un-scattered, divergent, light. With this system it was possible to detect the changes in the particle's motion due to the application of an external AC and DC electric fields. DC electric fields showed a shift in the average position of up to 100 nm and also a shift of the relevant oscillator frequency of up to 1500 Hz. Applying an AC electric field resulted in the particle's motion being driven at the AC frequency. On resonance the detected signal increased by a factor of 200 which helps to measure smaller changes in the particle's motion compared to the undriven signal. Using the AC driving it was possible to detect a particle with a charge of just 4 ± 3 electrons. In addition to this, two vacuum sources were investigated, the first being an ablating source that generated particles directly in the chamber, and the second being a sonicating source that releases pre-made particles from a surface. The ablated source used a high power nano-second Neodymium-doped Yttrium aluminium garnet (Nd:YAG) laser that was able to remove material from a silicon wafer with a 200 nm layer of silicon dioxide. It was possible to trap a nanoparticle with a radius of 35 ± 3 nm at atmosphere but there was a large thermal distribution in the particle sizes. The sonicating source had the advantage that the particle's size range could be known before hand and also the source could be very close to the trap site. An acoustic horn was developed that focused the energy down to a 3 mm radius surface. It was possible to see a large release of 100 nm particles, however, none of them were trapped. It was assumed that the particles were still too large to trap so steps were taken towards a MHz source. This resulted in the first detection of a particle from an ultrasonic source at the trap site. The signal didn't last long but this still holds promise as a source once a transducer or even a horn have been designed.

Contents

Abstract	iii
List of Figures	ix
List of Tables	xiii
Declaration of Authorship	xv
Acknowledgements	xvi
1 Introduction	1
1.1 Motivation	1
1.2 Overview of other force sensors	3
1.2.1 Micro-Cantilevers	3
1.2.2 MEMS	3
1.2.3 Ion traps	3
1.2.4 Optomechanical cavities	4
1.3 Outline	4
1.4 Publications	5
2 Optical trapping and position detection	7
2.1 Basics of a single beam trap	7
2.1.1 Spot size and trap depth	9
2.2 Aberrations	14
2.3 Particle's Motion	15
2.3.1 Fluctuation-dissipation theorem	15
2.3.2 Returning to the particle	16
2.4 Detection	18
2.5 Characterising the system	19
2.6 Phase lock loop and cooling	21
2.6.1 Cooling basics	21
2.6.2 Phase locked loop	22
2.7 Cooling	23
2.8 Frequency Tracking error	25
2.9 Phase space	26
2.10 Non-linear dynamics	28
2.11 Thermalisation rate	29
2.12 Conclusion	32

3	Force detection	33
3.1	Sensitivity	33
3.1.1	Standard quantum limit	34
3.1.2	Quantum force detection	37
3.1.3	Ground state thermal noise	38
3.1.4	Photon recoil	38
3.1.5	Detector noise	40
3.2	Coulomb force	42
3.2.1	Electrostatic field - Mean position	42
3.2.2	Electrostatic field - Frequency shift	45
3.2.3	AC electric fields	49
3.3	Gravity	50
3.3.1	Gravitational Constant	51
3.3.2	Change in local gravity	54
3.4	Magnetic resonance force microscopy	55
3.5	Conclusion	61
4	Ablation	65
4.1	Overview of particle loading	65
4.2	Ejection Mechanisms	66
4.3	Laser and power control	67
4.4	Particle generation	69
4.4.1	Using 532 nm	70
4.4.2	Air trapping	73
4.4.3	Draw backs with ablation as a source	74
4.5	Thermo-mechanically induced lift	75
4.6	Desorption of Particles from Glass	75
4.7	Particle density control	77
4.8	Conclusion	79
5	Sonicated Source	83
5.1	Van de Waals force	83
5.2	Piezo electronics	87
5.3	40 kHz transducer	89
5.3.1	Particle release	90
5.4	Ultrasonic Horn	91
5.5	Surface finish	94
5.6	Loading	95
5.7	MHz	97
5.8	Conclusion	99
6	Particle focusing	101
6.1	Laser focusing of particles	101
6.2	Magnetic focusing	102
6.3	Electrical focusing	104
6.4	Conclusion	105

7 Conclusion	107
7.1 Summary	107
7.1.1 Force sensing	107
7.1.2 Vacuum source	109
7.2 Future work	110
A Derivation of trapping force	111
B Technical drawings	113
B.1 Parabolic mirror	113
B.2 Needle	114
C Driven Harmonic Oscillator	115
D Quantum harmonic oscillator	117
Bibliography	119

List of Figures

1.1	Example of optomechanical cavity.	2
2.1	Correction constant for a aspheric lens.	10
2.2	3d trap potential with 0.9 NA at 1 watt.	12
2.3	Heat map of total trapping force.	14
2.4	Focus aberrations and multiple trap sites due to mismatching design wave-lengths.	15
2.5	Parabolic mirror trap and phaser diagram of detection system.	19
2.6	PSD of z motion as the pressure is lowered.	20
2.7	Centre frequency for z as a function of power.	21
2.8	PPL flow diagram.	22
2.9	General experimental setup.	23
2.10	Cooling of $\varnothing 80$ nm particle down to mK.	25
2.11	The flat top effect seen due to frequency drift.	26
2.12	Time series before and after filtering.	27
2.13	Phase space of cooled particle.	28
2.14	Ring states generated by on resonance driving.	30
2.15	Multi-ring state from an unstable laser.	31
2.16	Amplitude increase as particle re-thermalises to 300 K.	31
3.1	Minimal detectable force for different combinations of particle size, Q and air temperature.	34
3.2	Total noise contributions.	42
3.3	Coulomb setup and expected electric field.	43
3.4	Displacement of average position due to DC electric field.	45
3.5	Frequency shift and skew for change and un-charge particle.	47
3.6	Extremes of frequency shift and skewness due to DC field.	48
3.7	Sweep of AC electric field driving frequency.	50
3.8	Fitting to peak heights as AC driving frequency is swept.	51
3.9	Expected gravitation force for increasing edge separation and test mass.	52
3.10	Force between 1 kg mass, 1 cm away against particle radius.	53
3.11	Schematic diagram of the proposed experiment to measure gravitational constant.	54
3.12	Schematic diagram of the proposed experiment to measure g.	55
3.13	Change in the gravitational force on a $\varnothing 300$ nm particle for a given change in altitude.	56
3.14	Magnetic moments, their alignment to a magnetic field and separation energy.	57

3.15	Available spins at 300 K and 4.2 K for a $\varnothing 300$ nm particle.	58
3.16	Force due to the interaction between spins and magnetic field gradient. . .	60
3.17	Two examples of possible spin experiments.	61
3.18	Expected increase in peak height against the gradient of the magnetic field. .	62
3.19	Damage to needle during electric field experiments.	63
4.1	Particle formation mechanisms for different pulse energies.	66
4.2	Comparison of holes drilled into glass from a ns pulse laser and a fs pulse laser.	68
4.3	Pulse energy control using a pair of two polarising beam splitters.	69
4.4	Hole ablated though $525\ \mu\text{m}$ of Silicon.	70
4.5	The absorption coefficient of silicon.	71
4.6	Laser power as a function of flash lamp voltage at 532 nm.	71
4.7	Ablation spot with a pulse energy of 75 mJ.	72
4.8	Ablation spot with a pulse energy of 192 mJ.	72
4.9	Ablation spot with a pulse energy of 308 mJ.	73
4.10	Ablation spot with a pulse energy of 425 mJ.	73
4.11	Ablation spot with a pulse energy of 542 mJ.	74
4.12	PSD of trapped particle generated by ablation.	74
4.13	SEM of chip after lift attempt.	76
4.14	Desorption of particles from a surface without density control.	76
4.15	Density control, Initial mix.	77
4.16	Density control, mix 2 with 8 mg of Silicon.	78
4.17	Density control, mix 3 with 5 mg of Silicon.	78
4.18	Density control, mix 4 with 2 mg of Silicon.	78
4.19	Density control, mix 5 with 1 mg of Silicon.	79
4.20	Damage seen due to ablation of glass slide.	79
5.1	Coordinate system used for energy between point and a plane.	84
5.2	Coordinate system used for energy between plane and a sphere.	86
5.3	Stress and strain from a 40 kHz ultrasonic transducer.	90
5.4	Frequency response of the 40 KHz transducers.	91
5.5	Early tests of particles leave transducers surface.	92
5.6	Ultrasonic horn using to increase surface amplitude.	93
5.7	Vacuum release of particle off of the surface of ultrasonic horn.	94
5.8	Before and after polishing the tip surface.	94
5.9	Chrome coating and diamond turning of horn tip.	95
5.10	Improvements to loading method to result particle clumping.	96
5.11	Large particle release seen at vacuum after improvements.	97
5.12	Electrical response of MHz piezo ring.	98
5.13	Particle seen travelling through focus after release from MHz piezo.	99
5.14	Summation of predicted amplitude, acceleration and minimum particle radius that can be released.	100
6.1	Simulation of focusing particles after release using gradient force.	102
6.2	Unfocused and magnetically focused particle beams.	103
6.3	Focusing of charged particles with pulsed electric field.	105

B.1	The Autocad drawing sent to the manufacturer to produce the parabolic mirrors.	113
B.2	Design drawing used to manufacture the needle using in the electric fields experiments.	114

List of Tables

3.1	Sensitivities for different combinations of particle size, Q and air temperature.	34
4.1	Dilution rates of $\phi 100$ nm Silicon particles in powder form with Isopropanol.	77
4.2	Desorption experiments performed with different concentrations and laser powers.	80
5.1	Velocity increases with driving power.	91
6.1	Simulation parameters used in COMSOL of magnetic focusing of particles.	104
6.2	Simulation parameters used in COMSOL of electrical focusing of particles.	105

Declaration of Authorship

I, David Willian Hempston, declare that this thesis titled, ‘Force detection in levitated optomechanics’ and the work presented in it are my own. I confirm that:

- This work was done wholly or mainly while in candidature for a research degree at this University.
- Where any part of this thesis has previously been submitted for a degree or any other qualification at this University or any other institution, this has been clearly stated.
- Where I have consulted the published work of others, this is always clearly attributed.
- Where I have quoted from the work of others, the source is always given. With the exception of such quotations, this thesis is entirely my own work.
- I have acknowledged all main sources of help.
- Where the thesis is based on work done by myself jointly with others, I have made clear exactly what was done by others and what I have contributed myself.

Signed:

Date:

Acknowledgements

Sometimes I feel that my PhD has been as much a group effort as it has been my own work, and so there is a long list of people I would like to thank. Firstly, I would like to acknowledge The Templeton Foundation for funding my PhD and allowing me to undertake the body of research presented here. I would like to thank Hendrik Ulbricht for his advice, supervision, motivation and of course for providing the opportunity to do a PhD. I must thank James Bateman for his near encyclopedic knowledge of so many subjects and convincing me to use Linux early in my PhD. For at least a year we, as a group, were stuck with low quality optics and it was his idea to switch to reflective optics that helped us move past this. Another issue that plagued us was particle loss at low mbar pressures, which was solved by a simple experiment by Nathen Cooper. Nathen is also the inspiration for the spin experiments along with causing confusion by offering wasps to wandering undergrads. As I said, at times this was a group effort and so the work by Mudassar Rashid and Jamie Vovrosh is strongly linked to my own. Without them nothing would have got anywhere but I also have to thank Mudassar for his positivity and Jamie for his help in pulling problems apart and for his hours of work with the cooling systems. I would like to thank Ash Setter for helping me with my Python scripts both in and out of the lab and Chris Timberlake for asking the questions I hadn't thought of. I need to thank Paul Clark for his help in the clean room and for getting our own mini-clean room set up. George Winstone's contributions to the electric fields experiments were very insight full and I would like to thank him for that, and for filling my inbox with memes. In fact on that, I would like to thank all of the above for creating such an enjoying working environment through the course of my PhD. I would like to thank everyone in the Physics and Astronomy Department, including the engineers in both the mechanical and electronics workshops. No matter what crazy idea I managed to come up with they were always ready to listen and find a way that it might work in the real world. I can't thank my friends and family enough for all of their support and encouragement. I have been lucky in having such supportive and loving parents that go out of their way to help me in everything I do, as only parents can. Thank you to my brother, Steven, for listening to me rant and for generally just being a good friend and to Katie for being an amazing sister. I have a number of great friends, some whom have been there for me for many years; so thank you to Sarah Jones, Chris (Neo) Morell, Jason Radford, Elizabeth Buckland. Lastly thank you to Emma Holt, the love of my life, for putting up with me talking about physics for many hours, for picking me up when I felt I couldn't continue and for being my best friend.

Chapter 1

Introduction

1.1 Motivation

This thesis will explore the use of optomechanical systems as force detectors. In its purest form, optomechanics is the study of the interaction between light and a mechanical system. A typical example being a cavity with one mirror mounted on a spring so that it is free to move in the optical axis, see Fig.(1.1). The photons in the cavity impart momentum to the mirror via photon pressure which causes the mirror to move. The mirror's displacement results in a change in the cavity length which in turn causes a detuning of the cavity frequency. This detuning results in a reduction of the cavity fitness and so a drop in photon pressure. This is a well studied example of the coupling between light and a mechanical system. This thesis will present work on levitated optomechanics (LOM) where laser light is tightly focused by a lens or a mirror to generate a large electric field gradient. In the presence of an electric field, a nanoparticle will behave as a dipole and the focused electric field will generate a gradient force on the dipole, pushing it towards the laser's focus. Particles with a radius less than the spot size can be trapped within this focus and their centre-of-mass motion can be manipulated by modulating the intensity of the laser[1]. If confined inside a vacuum chamber the air can be evacuated while confining the particle's motion and preventing it from escaping the trap. The particle will naturally oscillate around an average position and, as there is no mechanical coupling, the damping of this oscillation depends only on the pressure in the chamber. The quality factor (Q) is used to characterise the energy lost in an oscillator per oscillation relative to the stored energy, $Q = \Omega_0/\Gamma_0$ where Ω_0 is the oscillator frequency and Γ_0 is the damping on the oscillator. Levitated optomechanics are able to reach much higher Q factors, 4×10^7 [2], than Micro-electromechanical systems (MEMS), 10^4 [3], or cavity optomechanics, 5.8×10^5 [4].

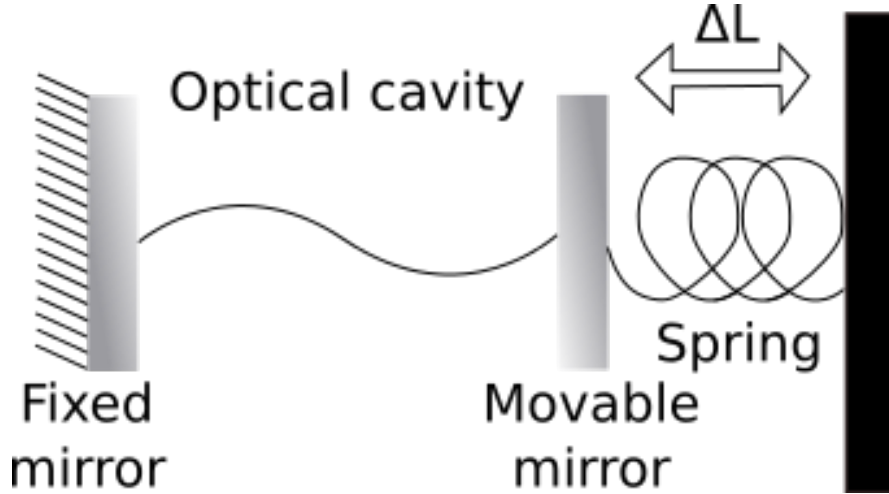


FIGURE 1.1: An example of an optomechanical cavity. One mirror is mounted on a spring so that it is free to move in the optical axis. The photons in the cavity impart momentum to the mirror via photon pressure which causes the mirror to move. This displacement results in a change in the cavity length which in turn causes a detuning of the cavity frequency. The detuning then causes in a reduction of the cavity fitness and so a drop in photon pressure.

In levitated optomechanics the motion of the particles can be controlled directly by simply modulating the power of the trapping laser. Without this, the kinetic energy of one degree of freedom is given by the thermal energy, $KE = 1/2k_B T$ where k_B is the Boltzmann constant and T is the thermal temperature of the surrounding gas. As the laser modulation is used to reduce the particles motion it is said to be cooled as the kinetic energy drops below the thermal energy. Once cooled sufficiently the particle's motion can be compared to the energy states of a quantum harmonic oscillator, with the mean occupation state given by $\langle n \rangle = k_B T / \Omega_0 \hbar$, where \hbar is the reduced Planck's constant. With this control, LOM systems have reached energy occupation states as low as 65 ± 5 ($T_{cm} = 450.5 \pm 33.1 \mu K$) without using cryogenic cooling[5] and have the potential to reach Quality factors of 10^{12} [6] at the ground state. The lack of cryogenics reduces running costs but also makes the system more portable compared to high sensitivity MEMS devices[7, 8] that have no other way of approaching the ground state. We are also able to change the test mass simply by trapping a different sized nanoparticle. This means that if the lowest force sensitivity is desired a small particle can be used, $r = 20 \text{ nm}$, but for forces that scale with mass, a larger particle can be used, up to $r \approx 300 \text{ nm}$ as shown in chapter 3. Levitated optomechanics operates in a relatively unique position where the trapping frequency is not dependent on the temperature of the surrounding medium (at least to a good approximation at high vacuum) meaning that if the use of cryogenics is desired it doesn't affect the trapping frequency. This allows for high force sensitivity in a frequency band (10 kHz-500 kHz) that many other force detectors can not operate in. For these reasons levitated optomechanics holds promise for precision measurements

in magnetic spin resonance [9], non-Newtonian gravity [10], high frequency gravitation waves [11], thermodynamics [12] and the limits of quantum mechanics [13].

1.2 Overview of other force sensors

1.2.1 Micro-Cantilevers

A micro-cantilever (MC) device typically involves a suspended component that is $\approx 100 \mu\text{m}$ in length and width but less than a few μms in thickness. This is mechanically coupled to the rest of the device at one end while being free to move at the other. The free end will oscillate at a frequency given by the shape and stiffness of the suspended beam, with an amplitude dependent on the thermal temperature. A dilution refrigerator is often used to reduce the thermal energy, allowing the MC to reach mk. Active feedback has also been used to push the mode temperature from 2.2 K to 2.9 mK [14]. MCs are typically made from silicon, silicon nitride, or silicon oxide [15] and have a force sensitivity of $10^{-19} \text{ N}/\sqrt{\text{Hz}}$ [16] allowing them to detect single spins [17]. Attempts to improve the sensitivity further have involved using an electrical detection system that can beat shot noise [18] and making MCs out of other materials such as diamond [19]. Even so cantilever systems have struggled to reach zepto-newton sensitivity.

1.2.2 MEMS

A micro-electromechanical system (MEMS) has a mechanical component that is free to move in at least one degree of freedom, and this movement is either induced or manipulated in the presence of an external force. The mechanical change is detected electrically either has a change in capacitance, resistance, or a shift in the natural frequency. MEMS come in many different configurations and are used in many different applications including accelerators [20], gyros [21], pressure sensors [22] and bio-medical [23]. Commercial devices are becoming common place, however, they are still in active development in science. MEMS devices have been able to detect the Casimir force [24] and the motion of the tides [8], while nanotube based resonators have achieved a sensitivity of $12 \times 10^{-21} \text{ N}/\sqrt{\text{Hz}}$.

1.2.3 Ion traps

Charged particles are attracted/repulsed by a surface that has the opposite/matching charge and they can also be made to perform orbits in a homogeneous magnetic field. By

combining these effects charged ions can be confined in a number of different traps, the two most common being Penning traps[25] and quadrupole traps (Paul trap)[26]. Laser cooling can be used to remove thermal energy from the ion(s), but it can only be used with a few kinds of ions that have a compatible energy level structure. Other methods, such as resistive cooling, active-feedback cooling, collisional cooling, radio frequency side-band cooling, or sympathetic laser cooling, can be applied to a larger range of ions[27]. Due to the ions small mass, ion traps have achieved impressive sensitivities into the $10^{-24} N/\sqrt{Hz}$ range[28][29] and there are schemes to reach as low as $10^{-27} N/\sqrt{Hz}$. Ion traps often have limited optical access, however the Stylus ion trap has shown that it is possible to improve this while still having yotto-newton sensitivities[30].

1.2.4 Optomechanical cavities

There is a large range of cavity based systems used for detecting different effects, varying from macroscopic transducer based devices[31] to using micron scale resonating disks[32]. This also results in a large range of sensitivities across many frequency bands. For example, Krause et al.[33] built an accelerometer using a photonic-crystal optomechanical cavity, resulting in an acceleration sensitivity of $10 \mu g/\sqrt{Hz}$, a centre frequency of 27.5 kHz and a bandwidth of ≈ 20 kHz. Another system uses a microwave optomechanical cavity to reach below the standard quantum limit using interferometric detection[34]. With this they achieve a force sensitivity of $5.1 \times 10^{19} N/\sqrt{Hz}$ with a centre frequency of 1 MHz. Micro-disk resonators can reach positional sensitivities of $4.4 \times 10^{-16} m/\sqrt{Hz}$ with a centre frequency of just 2 Hz[35]. By making the disk out of a magnetostrictive material a system can be built to measure magnetic field strength, with Forstner et al.[36] able to reach $400 nT/\sqrt{Hz}$.

1.3 Outline

The rest of this thesis is divided into 6 chapters. Chapter 2 starts from the basics of optical trapping and builds to explain our system including trapping with a parabolic mirror, parametric feedback and our homodyne-like detection. Chapter 3 details the force detection experiments that have been completed and the other forces that could be detectable with the given improvements. One of the biggest challenges in levitated optomechanics is loading single nanoparticles into the trap at ultra high vacuum (UHV). Chapters 4 and 5 cover the methods that were employed to attempt to load the trap at UHV. Chapter 4 covers direct particle generation near the trap site via surface ablation, while chapter 5 describes the work done with ultrasonic devices and releasing pre-made particles from a surface. Chapter 6 covers ideas to increase particle density near the

trap site using focusing techniques while Chapter 7 is the overall conclusion and gives an outlook for the future work.

1.4 Publications

The work detailed in this thesis contributed to the following papers:

Force Sensing with an optically levitated charged nanoparticle

David Hempston, Jamie Vovrosh, Marko Toro, George Winstone, Muddassar Rashid, Hendrik Ulbricht

Applied Physics Letters, Vol. 111, Issue 13, **2017**

Summary: Here I was able to demonstrate force detection by the direct application of an external field. Prior to this paper most other work in levitated optomechanics used theoretical values based on the thermal limit. I showed the detection of both constant and time varying forces and how these give rise to different effects. The majority of this work is my own with Jamie helping with feedback control, Marko contributing to the discussion of CSL, George helping with reviewer comments and Muddassar with the general writing.

Parametric feedback cooling of levitated optomechanics in a parabolic mirror trap

Jamie Vovrosh, Muddassar Rashid, David Hempston, James Bateman, Mauro Paternostro, Hendrik Ulbricht

Journal of the Optical Society of America B, Vol. 34, No. 6, **2017**

Summary: This paper detailed how we were able to trap and cool particles down to 10^{-6} mbar and a few millikelvin. My work was focused on trapping particles with diameters from 26 to 160 nm without feedback. Previously, it was assumed that a particle would always be lost below 1 mbar in the absence of feedback cooling. However, by using a parabolic mirror and a higher laser power I was able to reach 10^{-5} mbar, much lower than other work, with particles remaining trapped for hours before loss.

Experimental realization of a thermal squeezed state of levitated optomechanics

Muddassar Rashid, Tommaso Tufarelli, James Bateman, Jamie Vovrosh, David Hempston, M.S. Kim, Hendrik Ulbricht

Physical Review Letters 117 (27), 273601, **2016**

Summary: By applying pulses at $\omega_0/2$ it was possible to squeeze the particles motion. This is a rapid, nonadiabatic, process that could be used to reach lower energy states

for short periods of time. My work was mostly in helping in the lab and building the general experiment.

Chapter 2

Optical trapping and position detection

In levitated optomechanics a single nanoparticle is suspended in free space solely by a focused laser beam. This is possible due to the interaction between the dielectric properties of the nanoparticle and the gradient of the laser's electric field. This chapter will explain this interaction in more detail before explaining how to detect the trapped particle and its motion. Throughout this work nanoparticles are assumed to be spherical and so their size will be quoted as either a radius or a diameter. There is a common practice in engineering of preceded the size with the symbol \oslash when a size is referring to a diameter and this thesis will use it to emphasis when a diameter is being quoted, e.g. $\oslash 100$ nm is a 100 nm diameter particle.

2.1 Basics of a single beam trap

As the diameter of the particle is much smaller than the wavelength of the trapping light, ($\oslash 100$ nm versus 1550 nm respectively) it is appropriate to assume that the trapping light would undergo Rayleigh scattering[37]. The electric field causes the particle to become polarised, where the electron cloud of the atoms is shifted and a dipole is formed by the charge separation. As the particle is sub-wavelength the details of this distribution shift can not be resolved and so the nanoparticle can be treated as a single dipole within an inhomogeneous electromagnetic field. A dipole is equivalent to two charges separated by some distance. The total trapping force is then the sum of the Lorentz forces acting on this electric dipole as given by,

$$\begin{aligned}
\mathbf{F}_{trap} &= \sum_i \mathbf{F}_i \\
&= \sum_i q_i \left(\mathbf{E}_i + \frac{d\mathbf{x}_i}{dt} \times \mathbf{B} \right) \\
&= q \left(\mathbf{E}_1 - \mathbf{E}_2 + \frac{d(\mathbf{d})}{dt} \times \mathbf{B} \right), \tag{2.1}
\end{aligned}$$

where \mathbf{x} is the position, \mathbf{d} is the separation distance of the charges, \mathbf{E}_1 and \mathbf{E}_2 are the electric field of the charges, \mathbf{B} is the magnetic field, t is time, and q is charge. By noting that the dipole moment of the particle is given by $\mathbf{p} = q\mathbf{d} = \alpha\mathbf{E}$ (α is the polarisability and E is the total electric field) and writing \mathbf{E}_2 in terms of \mathbf{E}_1 it is possible to simplify Eq.(2.1) to,

$$\begin{aligned}
\mathbf{F}_{trap} &= q \left(\mathbf{E}_1 + \mathbf{d} \cdot \nabla \mathbf{E} - \mathbf{E}_1 + \frac{d(\mathbf{d})}{dt} \times \mathbf{B} \right) \\
&= \mathbf{p} \cdot \nabla \mathbf{E} + \frac{d\mathbf{p}}{dt} \times \mathbf{B} \\
&= \alpha \left(\mathbf{E} \cdot \nabla \mathbf{E} + \frac{d\mathbf{E}}{dt} \times \mathbf{B} \right).
\end{aligned}$$

A useful vector identity, Eq.(2.2), can then be used along with Faraday's law of induction, Eq.(2.3), to give Eq.(2.4).

$$(\mathbf{E} \cdot \nabla) \mathbf{E} = \nabla \left(\frac{\mathbf{E}^2}{2} \right) - \mathbf{E} \times (\nabla \times \mathbf{E}) \tag{2.2}$$

$$\nabla \times \mathbf{E} = -\frac{d\mathbf{B}}{dt} \tag{2.3}$$

$$\begin{aligned}
\mathbf{F}_{trap} &= \alpha \left(\nabla \frac{\mathbf{E}^2}{2} + \mathbf{E} \times \left(\frac{d\mathbf{B}}{dt} \right) + \frac{d\mathbf{E}}{dt} \times \mathbf{B} \right) \\
&= \alpha \left(\nabla \frac{\mathbf{E}^2}{2} + \frac{d}{dt} (\mathbf{E} \times \mathbf{B}) \right). \tag{2.4}
\end{aligned}$$

The second term is the time derivative of the Poynting vector which, for a stable laser, should be zero. Therefore the trapping force due to the focusing of the laser is given by,

$$\mathbf{F}_{trap} = \frac{\alpha}{2} \nabla E^2. \quad (2.5)$$

The laser also introduces a scattering term from Rayleigh scatter which is proportional to the scattering cross section given in Eq.(2.6). As this term is proportional to the sixth power of the radius, this force can be neglected for the particles used here. It is possible to trap larger particles using this scattering force and indeed it is how the early traps of A. Ashkin and J. M. Dziedzic [1] were performed. However, this is not covered in this thesis as it is not possible to scale down this technique to sub-wavelength particles.

$$\sigma_R = \frac{8\pi^3}{3\epsilon_0^2} \frac{\alpha^2}{\lambda^4}, \quad (2.6)$$

where α is the polarisability given by Eq.(2.10) and λ is the wavelength of the scattered light. Eq.(2.5) shows that the particle feels a force towards the focus proportional to the gradient of the electric field at that point. This force is always towards the focus and the particle's motion maps out the shape of the laser focus. For small oscillations this follows a sinusoidal pattern as seen in a harmonic oscillator. It is sensible to use Hooke's law to derive the frequency of oscillation,

$$f = \sqrt{\frac{k}{m}} \frac{1}{2\pi}, \quad (2.7)$$

where m is the mass of the nanoparticle and k is the trap stiffness. k can be obtained by taking the second derivative of the potential. The potential is also related to the trap depth but first the spot size of the focus needs to be calculated.

2.1.1 Spot size and trap depth

The larger the gradient, the larger the trapping force and so the better the nanoparticle is confined to the trap. This can be seen from the energy point of view as well. Neutral dielectric particles are high field seeking, meaning they will move towards areas with a high energy density. For a Gaussian beam, the larger the numerical aperture (NA) of the focusing element, the smaller the waist and so the higher the energy density at the focus. The calculation of the waist is,[38],

$$w_0 = \frac{C\lambda}{\pi N.A} = \frac{C\lambda}{\pi \tan^{-1}(\frac{r}{f})}, \quad (2.8)$$

where r is the radius of the lens, f is the focal length, λ is the wavelength of the light and C is a constant given by Fig.(2.1). C is a result of scalar diffraction theory for a large NA aplanatic lens system, for example condenser lenses on microscopes, and it is assumed to be 1 for reflective optics. Away from the focus the beam waist goes as,

$$w(z) = w_0 \sqrt{1 + \left(\frac{z}{z_R}\right)^2}, \quad (2.9)$$

where z is the distance from the focus along the optical axis and $z_R = \frac{\pi w_0^2}{\lambda}$ is the Rayleigh range with λ as the wavelength of the trapping light.

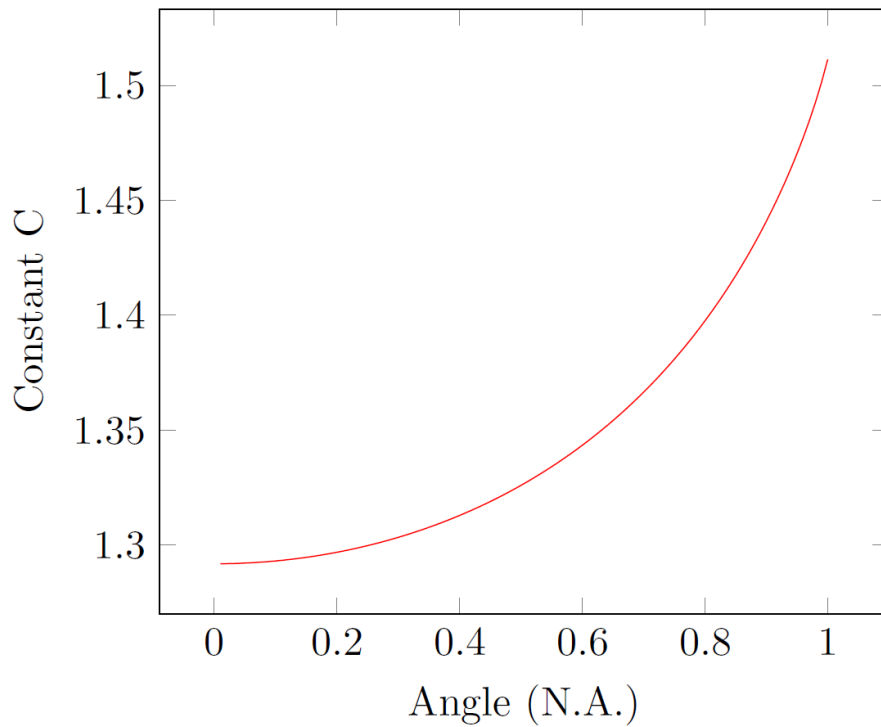


FIGURE 2.1: Curve for constant C [39] as used in Eq.(2.9). C is a result of scalar diffraction theory for a large NA aplanatic lens system, e.g. condenser lenses on microscopes, that is free from spherical aberrations. An single aplanatic lens has two aspherical surfaces optimised for a single design wavelength[40] and so commercially are known as an aspheric lens.

The energy of a dipole is $U = -\mathbf{p} \cdot \mathbf{E}$ where \mathbf{p} is the dipole moment. Substituting in $\mathbf{p} = \alpha \mathbf{E}$ and taking the differential gives Eq.(2.5), but more interesting things can be done with the energy representation. The polarisability of the nanoparticle is given by the Clausius-Mossotti relation,

$$\begin{aligned}
\alpha &= \epsilon_0 \frac{3}{N} \frac{n^2 - 1}{n^2 + 2} \\
&= 3\epsilon_0 \frac{m_{Pa}}{\rho} \frac{n^2 - 1}{n^2 + 2} \\
&= 3V\epsilon_0 \frac{n^2 - 1}{n^2 + 2}, \tag{2.10}
\end{aligned}$$

where m_{pa} is the mass of the nanoparticle, ρ is the density of nanoparticle, ϵ_0 is the permittivity of free space, V is the volume of the particle, and $n \approx \sqrt{\epsilon_r}$ at optical wavelengths[41]. The laser light is unable to resolve any of the features of the particle so it acts as a single dielectric particle rather than a collection. The potential is therefore given by,

$$U = -3V\epsilon_0 \frac{n^2 - 1}{n^2 + 2} |\mathbf{E}|^2. \tag{2.11}$$

Note that the intensity of the laser focus can be written as $I_0 = \frac{P}{\pi w_0^2}$ or $I_0 = \frac{1}{2}cn_0\epsilon_0|\mathbf{E}(\mathbf{0})|^2$, where P is the laser power, c is the speed of light and n_0 is the refractive index of the medium the laser is focused in. These can be combined to give $|\mathbf{E}(\mathbf{0})|^2 = \frac{2P}{\pi\epsilon_0cw_0^2}$, where $n = 1$ for air. It should be noted that an assumption has been made that the focus is the same with and without a particle. For particles with a small radius compared to the focus waist this is fine, but if $r \approx w_0$ a more complete model for the 3 dimensional intensity would have to be used [42][43]. Using the simple intensity equation with Eq.(2.11) and expanding for volume gives,

$$\begin{aligned}
U_0 &= -3V\epsilon_0 \frac{n^2 - 1}{n^2 + 2} |\mathbf{E}(\mathbf{0})|^2 \\
&= -3V\epsilon_0 \frac{n^2 - 1}{n^2 + 2} \frac{2P}{\pi\epsilon_0cw_0^2} \\
&= -3\frac{4}{3}\pi a^3\epsilon_0 \frac{n^2 - 1}{n^2 + 2} \frac{2P}{\pi\epsilon_0cw_0^2} \\
&= \frac{8P}{w_0^2c} a^3 \frac{n^2 - 1}{n^2 + 2}, \tag{2.12}
\end{aligned}$$

where a is the radius of the particle[44]. Typically, a $\varnothing 100$ nm Silicon dioxide nanoparticle is used with a density of 2650 kg/m^3 and a laser power of 1 W. This is trapped with a $1.55 \mu\text{m}$ laser at 0.5 W using either a 0.9 NA mirror or a 0.6 NA aspheric lens. For the mirror the focus waist is $0.55 \mu\text{m}$ with a peak potential of 3.5×10^{-18} J. For the aspheric lens the focus waist is $1.1 \mu\text{m}$ and the peak potential is 8.8×10^{-19} J. Using

$k_b T$ even the aspheric gives a maximum trap depth of 6×10^4 K, which is significantly above the background temperature showing that it should be able to generate a stable trap. Assuming a Gaussian beam, $|E|^2$ is given by,

$$|\mathbf{E}(r, z)|^2 = |E_0|^2 \left(\frac{w_0}{w(z)} \right)^2 e^{\left(\frac{-2r^2}{w(z)^2} \right)}, \quad (2.13)$$

where r is the radial direction and $|E_0|^2 = \frac{2P}{\pi \epsilon_0 c w_0^2}$ as before. Combining this with Eq.(2.11) gives the 3 dimensional equation for the potential,

$$U(r, z) = \frac{8Pa^3}{cw_{(z)}^2} \frac{n^2 - 1}{n^2 + 2} e^{\left(\frac{-2r^2}{w(z)^2} \right)}. \quad (2.14)$$

Fig.(2.2) shows this plotted in 3 dimensions using the same $\varnothing 100$ nm silica nanoparticle with 0.5 W with a 0.9 NA focusing element.

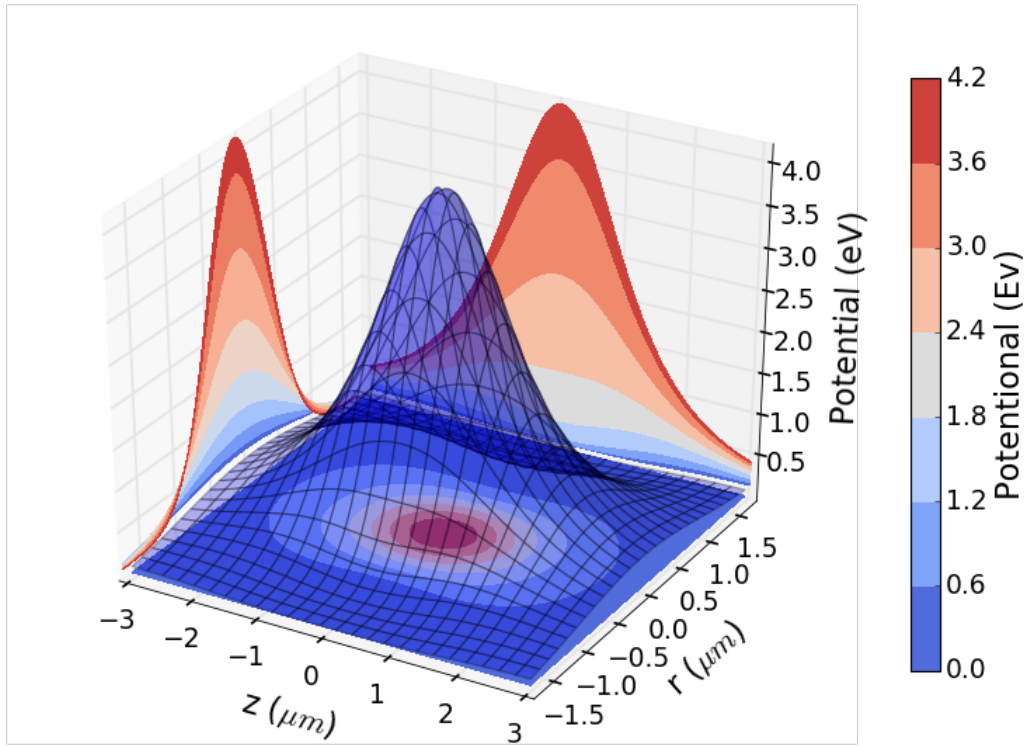


FIGURE 2.2: A plot of Eq.(2.14) with contour projections in z and r . r ranges across $\pm 2w_0$, z varies over $\pm 2z_R$, and z is scaled in electron-volts. z_R is the Rayleigh range given by $z_R = 2w_0^2/\lambda$ and $1\text{ev} = 1.6 \times 10^{-19}\text{J} = 11600\text{K}$. For oscillations where the amplitude is much less than the spot radius the potential can be approximated as a classical harmonic oscillator.

The difference in the longitude (Z) and radial (X, Y) directions is clearly visible with the radial being much narrower. This will result in the radial directions having higher trap

frequencies and now that the potential is known the relation for the trapping frequencies can be given as,

$$\begin{aligned}\left.\frac{\partial^2 I}{\partial z^2}\right|_{r=0} &= \frac{4P\lambda^2}{\pi^3 w_0^6} z^2 = \frac{1}{2} m \omega_z^2 z^2 \\ \therefore \omega_z &= \sqrt{\frac{8P\lambda^2}{\pi^3 m w_0^6}},\end{aligned}\quad (2.15)$$

$$\begin{aligned}\left.\frac{\partial^2 I}{\partial r^2}\right|_{z=0} &= \frac{4P}{\pi w_0^4} r^2 = \frac{1}{2} m \omega_r^2 r^2 \\ \therefore \omega_r &= \sqrt{\frac{8P}{\pi m w_0^4}},\end{aligned}\quad (2.16)$$

where ω_z is the centre frequency for z motion, ω_r is the same for the radial motion and w_0 is the trap waist so that $\frac{\omega_r}{\omega_z} = \frac{\pi w_0}{\lambda}$. This is assuming a Gaussian beam but it doesn't include the differences in trap size due to polarisation. This causes the radial frequencies to separate but the centre of the two should still follow the relation $\frac{\omega_y - \omega_x}{2\omega_y} = \frac{\pi \omega_0 \omega_z}{\lambda} + 1$. The force equation given in Eq.(2.5) now becomes,

$$F(r, z) = \frac{8Pa^3}{c} \frac{n^2 - 1}{n^2 + 2} \nabla \left(\frac{1}{w(z)^2} e^{\frac{-2r^2}{w(z)^2}} \right). \quad (2.17)$$

In cylindrical coordinates $\nabla = \hat{r} \frac{\partial}{\partial r} + \hat{z} \frac{\partial}{\partial z}$ so Eq.(2.17) can be broken down into two parts. For simplicity let β equal the leading constant so that the force component in the \hat{r} direction is,

$$\begin{aligned}\mathbf{r} &= \beta \frac{\partial}{\partial r} e^{\frac{-2r^2}{w(z)^2}} \\ &= \beta \frac{-4r}{w(z)^2} e^{\frac{-2r^2}{w(z)^2}}.\end{aligned}\quad (2.18)$$

The longitudinal direction is a little more involved as it makes use of the product rule so the full derivation is given in Appendix.(A) but the final result is,

$$\mathbf{z} = -\beta 2z w_0^2 e^{\frac{-2r^2}{w(z)^2}} \left(\frac{1}{w(z)^4} + \frac{2r^2}{w(z)^6} \right). \quad (2.19)$$

Combining Eq.(2.18) and Eq.(2.19) gives,

$$\mathbf{F}(r, z) = 2\beta e^{\frac{-2r^2}{w(z)^2}} \left(\hat{r} \frac{2r}{w(z)^4} + \hat{z} \left(\frac{w_0^2}{w(z)^4} - \frac{2r^2 w_0^2}{w(z)^6} \right) \right) \quad (2.20)$$

The magnitude of the total force is $|\mathbf{F}| = \sqrt{\mathbf{r}^2 + \mathbf{z}^2}$ and is plotted in Fig.(2.3). Again the difference between z and r is prominent and means that a particle will move more for a given force in z than in r . It is for this reason that this thesis will focus on the z motion. The Gaussian assumption used to obtain these equations is not always true with a common example being due to lens aberrations.

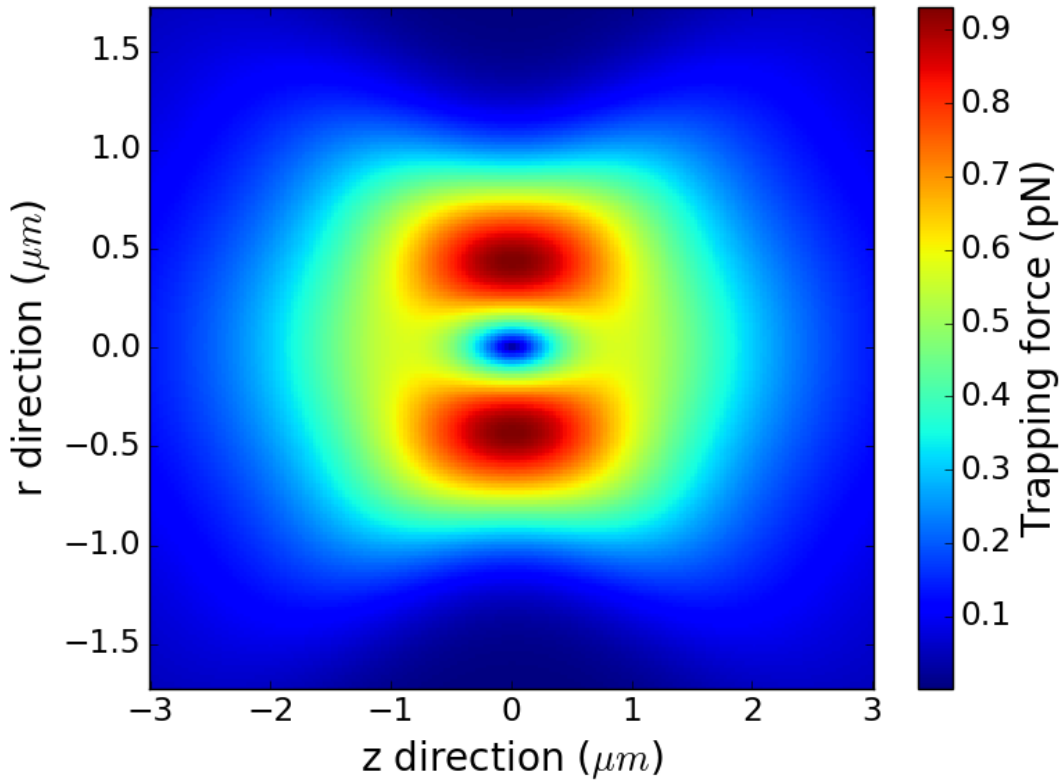


FIGURE 2.3: A plot of the magnitude of Eq.(2.20) from $\pm 2w_0$ for r and $\pm 2z_R$ for z . The difference in trapping strength between z and r is clear with the largest z force being almost half the maximum r force. This will result in the particle being more responsive to external forces in the z direction resulting in a larger signal.

2.2 Aberrations

For most of this work the focusing element is a parabolic mirror as this allows the NA to be close to 1. It was designed to minimise spherical aberrations and as a mirror it also doesn't suffer from the chromatic aberrations refractive optics suffer from. Before this the main focusing element was an aspheric lens from Thorlabs (AL1210-C) with an NA of 0.6 and a focal length of 10 mm. However, it was discovered that the design

wavelength was 780 nm and so there was significant chromatic aberration resulting in multiple, low intensity trap sites rather than the desired single high intensity focus. These aberrations are shown in Fig.(2.4) where A shows the particles trapped at the multiple trapping sites and B shows a ray tracing of the focus of a lens designed at 780 nm focusing 1550 nm light. The Strehl ratio is a 0 to 1 measure of the image quality used to quantify aberrations[45]. Using 780 nm this lens gives a Strehl ratio of 0.82 but with the 1550 nm laser the Strehl ratio drops to 0.20. This means that at the design wavelength the focus waist is $0.6 \mu\text{m}$ and has a clean focus with minimal aberrations. With 1550 nm laser light however, the focus waist is $66 \mu\text{m}$ generating a trap depth of just 17 K for a $\varnothing 100 \text{ nm}$ particle. In order to just beat the 300 K background energy a diameter of $\varnothing 300 \text{ nm}$ would be needed at 1 W. Even then this particle is unlikely to stay trapped as it will be very susceptible to thermal fluctuations. It is for this reason that the parabolic mirror was developed to avoid this chromatic aberration. An aspheric with the correct design wavelength was eventually developed by Thorlabs (C660TME-C) and when a lens is mentioned in this thesis it is this lens that was being used.

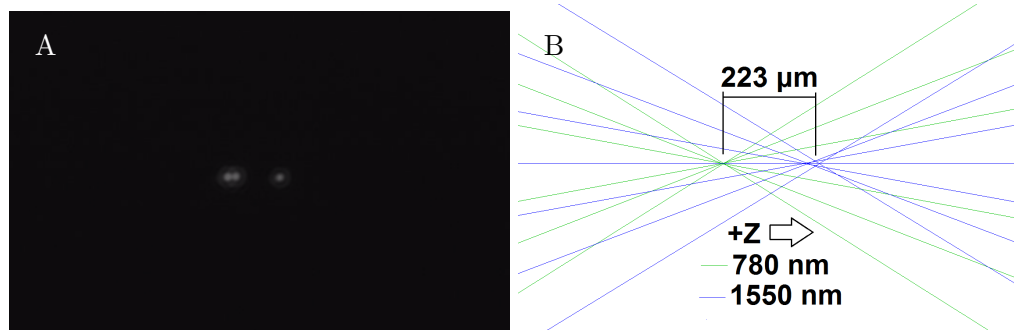


FIGURE 2.4: **A:** Composite image of particles trapped at the multiple sites. This is a side on image of nanoparticles trapped with 4 watts. **B:** Ray tracing diagrams of the focus for both the design wavelength of 780 nm and the trapping laser's wavelength of 1550 nm. The 780 nm is very clean and has a waist of $0.6 \mu\text{m}$ with a Strehl ratio of 0.82. However, for 1550 nm the focus is moved out in z by $223 \mu\text{m}$, the waist radius increases to $66 \mu\text{m}$ and the Strehl ratio decreases to 0.2.

2.3 Particle's Motion

2.3.1 Fluctuation-dissipation theorem

Before continuing it is useful to explain a theorem in statistical physics that is used to relate effects that come from the same physical origin, that is the fluctuation-dissipation theorem. Kubo[46] gives a good example that is useful here and relevant to this work. Take a small mirror, suspend it in a fluid, and let the system come to thermal equilibrium. If the angular rotation of the mirror is measured, say with a reflected laser, then it will be observed that the mirror is in fact moving irregularly around an average position. This

is the fluctuating force due to the random motion of the particles in the fluid colliding with the mirror. If the mirror is rotated deliberately, then there will be a force that goes against that motion. This is due to impacts from the particles in the fluid hitting the mirror as it is moved through it. Although the motion of the particles is random, the movement of the mirror results in an average resistive force that is proportional to the velocity of the mirror's motion. There are therefore two forces that originate from the motion of the particles in the fluid. The fluctuation-dissipation theorem therefore relates how a system will respond to an external disturbance to the internal fluctuation of the system in the absence of the disturbance.

2.3.2 Returning to the particle

Once a particle is trapped it will oscillate as a damped harmonic oscillator. Even at UHV there will be some damping of the particle's motion due to collisions with air molecules, given by $m\Gamma_0 x'(t)$ where Γ_0 is the damping rate and $x'(t)$ is the particle's velocity in a given direction of motion. This damping will cause a broadening of the frequency peak and limit the amplitude of oscillation. There is also a stochastic driving force, F_{th} , as the air molecules move around randomly and collide with the nanoparticle. The motion of the molecules is thermally driven and so F_{th} is assumed to satisfy the Fluctuation-dissipation theorem[47] as both the damping and driving forces are a result of Brownian motion.

Bringing these forces together gives a full equation for the particle's motion in each degree of freedom,

$$F = mx''(t) = F_{th} - m\Gamma_0 x'(t) - m\omega_0^2 x(t). \quad (2.21)$$

For small amplitudes the harmonic approximation holds so that $x(t) = \sin \omega_0 t$. The force equation is more commonly rearranged to give,

$$x''(t) + \Gamma_0 x'(t) + \omega_0^2 x(t) = \frac{F_{th}(t)}{m}. \quad (2.22)$$

Taking the Fourier transform of Eq.(2.22) gives Eq.(2.23)

$$-\omega^2 x(\omega) - i\omega\Gamma_0 x(\omega) + \omega_0^2 x(\omega) = \frac{F_{th}(\omega)}{m}. \quad (2.23)$$

Solving for $x(\omega)$ then taking the squared magnitude will give the power spectral density (PSD) of the motion as $S_{xx} = \langle |x(\omega)|^2 \rangle$,

$$S_{xx}(\omega) = \frac{1}{m^2} \frac{\langle |F_{th}(\omega)|^2 \rangle}{(\omega_0^2 - \omega^2)^2 + \Gamma_0^2 \omega^2}. \quad (2.24)$$

This shows how the energy is distributed across frequency space. The thermal term can be calculated by taking the integral of Eq.(2.24) and comparing it to the total energy of that degree of freedom.

$$\begin{aligned} \langle x^2 \rangle &= \int_0^\infty S_{xx} d\omega \\ &= \frac{1}{2} \int_{-\infty}^\infty S_{xx} d\omega \\ &= \frac{\langle |F_{th}(\omega)|^2 \rangle}{2m^2} \int_{-\infty}^\infty \frac{d\omega}{(\omega_0^2 - \omega^2)^2 + \Gamma_0^2 \omega^2} \\ &= \frac{\langle |F_{th}(\omega)|^2 \rangle}{2m^2} \frac{\pi}{\omega_0^2 \Gamma_0}. \end{aligned} \quad (2.25)$$

From the equipartition theorem, $E = \frac{1}{2} k_B T_0 = \frac{1}{2} m \omega_0^2 \langle x^2 \rangle$ where k_B is the Boltzmann constant and T_0 is the internal temperature. This can be used with Eq.(2.25) to give $\langle |F_{th}(\omega)|^2 \rangle = 2m k_B T_0 \Gamma_0 / \pi$ and so Eq.(2.24) becomes,

$$S_{xx}(\omega) = \frac{k_B T_0}{\pi m} \frac{\Gamma_0}{(\omega_0^2 - \omega^2)^2 + \Gamma_0^2 \omega^2}. \quad (2.26)$$

The damping rate comes from kinetic theory and is given by Eq.(2.27)[48], where $Kn = l/L$ is the Knudsen number given by the mean free path (l) divided by the relevant length scale and $\xi = 18.6 \mu Pa$ is the viscosity of air[49]. For this thesis $L = r$ was used.

$$\Gamma_0 = \frac{6\pi\xi r}{m} \frac{0.619}{0.619 + Kn} \left(1 + \frac{0.31Kn}{0.785 + 1.152Kn + Kn^2} \right). \quad (2.27)$$

For a Boltzmann gas the mean free path is $l = \frac{k_B T}{\sqrt{2} \pi a^2 p}$, where p is the pressure of the surrounding gas and a is the radius of the gas particles. At high pressures, e.g. atmosphere, $Kn \approx 1$ and Γ_0 is large. As the pressure drops so does the damping and the particle's motion can be seen. To detect this motion an interferometric detection scheme was devised. There is a conversion factor, γ , needed to convert the voltage change measured at the detector into displacement in metres. This can be obtained directly by fitting Eq.(2.26) to the measured PSD and assuming that the particle is in thermal equilibrium with the environment, i.e. $T = 300$ K. This only needs to be done once for a given particle so long as the alignment is not changed. This gives a

full mathematical description of how the particle moves in the trap that can be used to characterise the trapped nanoparticle. In order to do this though a setup is needed to detect the particle's motion with as high a degree of precision as possible. For this reason an interferometric detection system was built and this will be discussed next.

2.4 Detection

As covered in Sec.(2.2) for most of this work a parabolic mirror was used as the focusing element to avoid chromatic aberrations and to achieve the highest NA. The mirror setup that was used is detailed in Fig.(2.5.A). The trapping field, E_{Trap} , comes in collimated and is focused by the parabolic mirror. Most of this light is divergent after the focus but when a particle is trapped a small amount is scattered back to the mirror. This scattered light is then re-collimated by the mirror and sent to the detector. Here the detection system is Homodyne-like as the backscattered signal from the particle, E_{Scat} , is mixed with the divergence light that is not scattered by the particle, E_{Div} . This results in a signal that is proportional to the phase difference between the two paths. This is shown in Fig.(2.5.B) as a phasor diagram where we have boosted into the frame of E_{Div} and normalised to 1. The magnitude of E_{Scat} doesn't change as the particle is sub-wavelength and doesn't move far in the focus, however the phase does change due to the change in path length. This changes the angle, θ , causing a change in the length of E_{Total} as its magnitude is $|E_{Total}|^2 = |E_{Scat}|^2 + |E_{Div}|^2 + |E_{Scat}||E_{Div}|e^{i\theta(t)}$. It is this modulation that is detected with a photodiode.

The number of photons scattered for a given particle position should be approximately constant across the full range of motion, assuming the particle remains in the linear regime. The number of photons scattered per second can be obtained by multiplying the Rayleigh cross section as given in Eq.(2.6) by the intensity and then dividing by the energy of a single photon,

$$n = I(z, r)\sigma_R \frac{\lambda}{hc}, \quad (2.28)$$

where $I(z, r)$ is the Gaussian distribution as used in Eq.(2.12), h is Planck's constant and c is the speed of light. For 1 watt of laser power this varies from $2 - 4 \times 10^{11}$ 1/s over the whole $1.55 \mu m$ focus but the particle typically only moves 100 nm or less once it is cooled. $|E_{Total}|$ is therefore just a constant plus $|E_{Scat}||E_{Div}|e^{i\theta(t)+\phi}$ where $\theta(t) = \frac{2\pi}{\lambda}e^{i\omega_0 t} \approx \frac{2\pi}{\lambda}x(t)$ and ϕ is some fixed phase difference. It is this interference term that gives the high positional sensitivity and using this the characteristics of the system can now be examined.

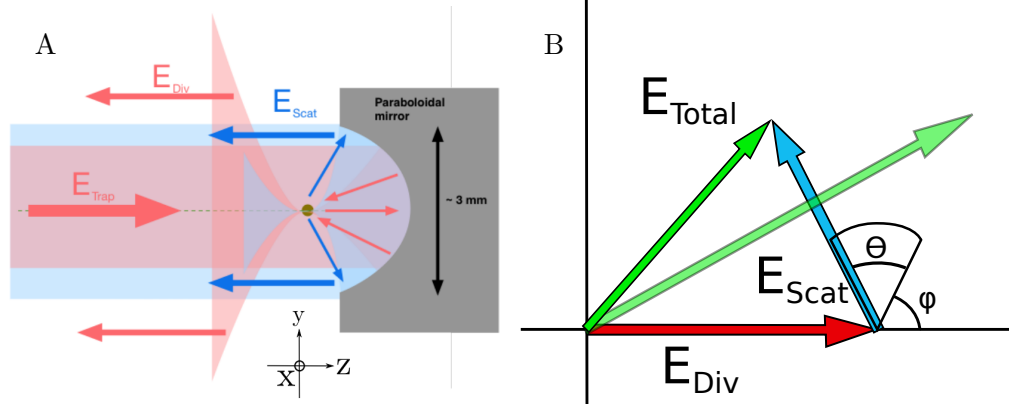


FIGURE 2.5: **A:** Parabolic mirror trap. The incoming laser is E_{Trap} and is collimated before being focused by the mirror. This focus is the trap site for the nanoparticle and after this the electric field is divergent as it leaves the trap E_{Div} . When a nanoparticle is trapped it will scatter some of E_{Trap} back to the mirror which will re-collimated it as E_{Scat} . E_{Scat} and some of E_{Div} as then mixed and the resulting interferometric signal detected by a photodiode. **B:** Phasor diagram boosted into the frame of E_{Div} and normalised to 1. The length of E_{Scat} is constant as the particle is sub-wavelength and doesn't move far in the focus, however the phase does change due to the change in path length. This changes the angle, θ , causing a change in the length of E_{Total} . Composite image of particles trapped at the multiple sites. This is a side on image of nanoparticles trapped with 4 watts.

2.5 Characterising the system

It is now possible to begin to characterise the system with the mathematical description given earlier and the measurements from the detection method. An important parameter of any oscillator is its Quality factor, $Q = \frac{\omega_o}{\Delta\omega}$, which gives the energy loss per cycle of the oscillator as a fraction of the peak energy. Higher Q indicates a lower rate of energy loss relative to the stored energy of the oscillator and also implies that the oscillator will remain in phase with itself for longer allowing for long integration times from a single event. For example, a pendulum suspended from a high-quality bearing in vacuum has a high Q ($Q \gg 1/2$) and will ring for a relatively long time if struck with a hammer, while a pendulum immersed in oil has a low Q ($Q \ll 1/2$) and the motion will be damped almost immediately. The Q of the system should be very high at high vacuum (HV) as the particle is not mechanically connected to anything. Even at HV there will be some damping from air collisions as given in Eq.(2.27) with the inverse pressure relation shown in Fig.(2.6.C). As the pressure drops the full width at half maximum (FWHM given by $\Delta\omega$) also decreases leading to an improvement in Q . At a pressure of 7.3×10^{-5} mbar, Fig.(2.6.A) shows $Q \approx 66$ making it a high Q , underdamped resonator. A narrow $\Delta\omega$ also allows for precision measurements of frequency shifts that might result from the application of an external force. The frequency shift seen both in the theory, Fig.(2.6.B), and experiment, Fig.(2.6.A), is due to the reduction in the $1/f$ noise and an increased signal from the particle as the pressure is reduced. The peak at 3×10^{-3} mbar has a

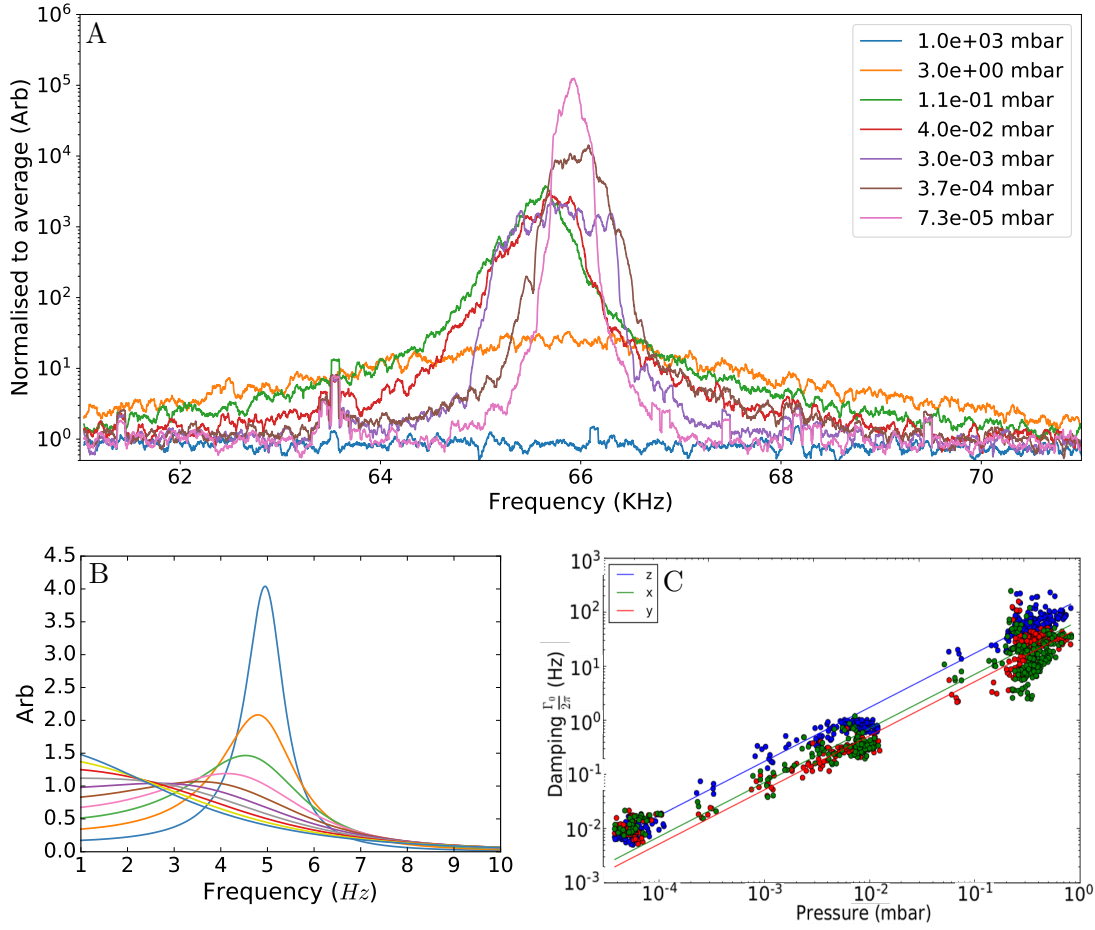


FIGURE 2.6: **A:** As the damping, Γ_0 in Eq.(2.26) is reduced the oscillation frequency is revealed. There is a small change in centre frequency with decreasing damping and this can be seen in the theory as well. At the lowest pressure of 7.3×10^{-5} mbar the $Q \approx 66$. **B:** Theory plot of Eq.(2.26) with a centre frequency of 5 Hz with damping from 10 to 1 Hz. **C:** Damping vs pressure from 3 mbar to 5×10^{-5} mbar showing the linear relationship expected. This was done by pumped down to HV and slowly letting the pressure build back to atmosphere. It is difficult to control the pressure which is why there are more measurements at some pressures than other.

much larger FWHM than might be expected. This is due to the vibrations from the turbo pump at low RPMs and resonances with the vacuum chamber.

The $\omega_i \propto \sqrt{P}$ relation seen in Eq.(2.15) and Eq.(2.16) is shown in Fig.(2.7). The power is increased from 1 to 5.5 Watts and examples of the shift of the z frequency peak is shown in Fig.(2.7.A) while the overall trend is shown in Fig.(2.7.B). The fit line is A/\sqrt{P} , where A is a constant, and there is strong agreement between this and the measured values with $R^2 = 0.99$. There is some change in the heights of the peaks themselves, although the general trend of increasing peak height with power is due to the increase in detection signal as there is more laser power. The more random variations are due to the instabilities in the detection system at the time the measurements were made. This data is still the best example of the power shift however, as it has the largest power range

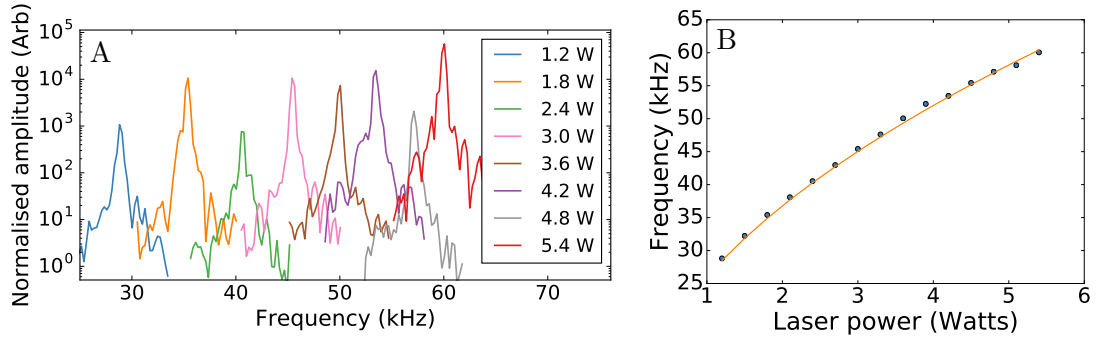


FIGURE 2.7: **A:** 400 ± 1 nm particle trapped using a Thorlabs C660TME-C Aspheric lens. The power is varied with 1-5.5 watts resulting in a frequency shift of the z natural frequency from 28 kHz to 60 kHz. **B:** Centre frequency against power, shows a strong agreement to the $\omega_i \propto \sqrt{P}$ relation given in Eq.(2.15) and Eq.(2.16 with $R^2 = 0.99$ and a standard error of 0.2 kHz.)

when compared with work on the more stable laser used for later work. Although this is already a high Q system it can be improved significantly by introducing the cooling system.

2.6 Phase lock loop and cooling

2.6.1 Cooling basics

As shown in Fig.(2.6), when the pressure drops the mean free path of the trapped particle increases. If the mean free path becomes larger than the trap region then the particle may even be able to escape the trap completely. To prevent this, a negative feedback system is used to reduce the particle's motion. Recall that the trapping force is proportional to $|E|^2$ which can be written in terms of laser power (P), and focus waist ($w(z)$). This Eq.(2.5) to be written as,

$$F_{Trap} = \frac{\alpha P}{\pi c \epsilon_0} \frac{1}{\nabla w(z)^2}, \quad (2.29)$$

where ϵ_0 is the vacuum permittivity and $\nabla w(z)^{-2}$ is the grad of the squared waist at a position z . This is for the z direction, for the radial direction the intensity will be the off-axis intensity at z and r . This allows the trapping force to be modulated by simply modulating the laser power. When the particle is near the centre of the trap the power can be turned down, as the particle is already in the trap. As the particle leaves the trap centre, the power can be turned back up, pulling the particle back towards the centre. This removes energy from the particle compared to a static laser power as the trap is

now non-conservative, i.e with a static laser power the particle is accelerated through the centre but with the modulated laser this acceleration can be prevented. This is seen as an additional damping source and is often described as a cooling term as it reduces the particle's kinetic energy. This turns Eq.(2.26) into,

$$S_{xx}(\omega) = \frac{k_B T_0}{\pi m} \frac{\Gamma_0}{((\omega_0 + \delta\omega)^2 - \omega^2)^2 + \omega^2(\Gamma_0 + \delta\Gamma)^2}, \quad (2.30)$$

where $\delta\omega$ is a frequency shift as a result of mismatching between the feedback signal and the natural frequency, and $\delta\Gamma$ is the damping from the feedback signal. The feedback needs to modulate the laser power at twice the natural frequency of the selected degree of freedom, as the particle passes through the centre twice in a single oscillation, and needs to be in-phase with the particle's motion. Even at very low pressures random collisions with air particles will cause the phase to change with time so a tracking system needs to be employed.

2.6.2 Phase locked loop

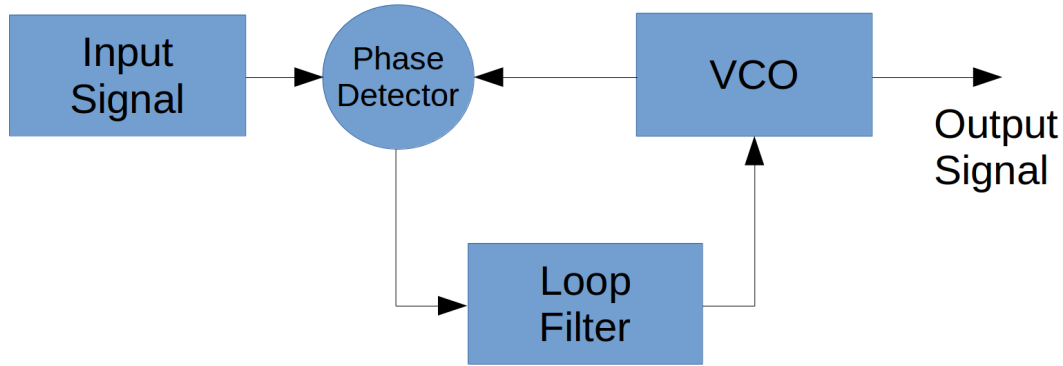


FIGURE 2.8: The phase difference between the VCO signal and the input signal is passed through a filter to remove noise. This is then passed back to the VCO and modifies the output frequency forming a closed loop. This continues so long as there is a phase difference. The output signal is also from the VCO and in the feedback system this also passes through a frequency doubler before leaving the control electronics.

A phase locked loop (PLL) uses a local oscillator, normally a voltage controlled oscillator (VCO), and a phase comparator to maintain a constant phase difference between the local oscillator and an input signal. Fig.(2.8) shows the flow diagram for a general PPL. The VCO will have some starting phase and a phase detector determines the difference between this and the input signal. This error signal is then passed through a filter system that removes phase noise and produces a DC signal. This is fed into the VCO and is used to change the VCO output frequency. This loop continues until the phase difference between the input and VCO signal is minimised (or it reaches some set phase difference).

The output signal is then simply split off from the VCO signal and amplified as needed. To cool the particle the second harmonic of the trap frequency is needed so the VCO feeds into a second system that both frequency doubles and amplifies the output signal as necessary. This signal then drives an acousto-optical modulator (AOM), as shown in the setup diagram in Fig.(2.9), that controls the input laser power to the particle trap. The trapping laser passes through the acousto-optical modulator (AOM), a polarising beam splitter (PBS) and a quarter waveplate into the parabolic mirror to be focused. Once a particle is trapped the detection signal, as described earlier, travels through the quarter waveplate so that the polarisation is now in the horizontal plane and is reflected at the PBS onto the photodiode. This completes the loop and allows the PLL to control the laser power with respect to the particle's position and so reduce the kinetic energy which is characterised as a reduction in T_{com} .

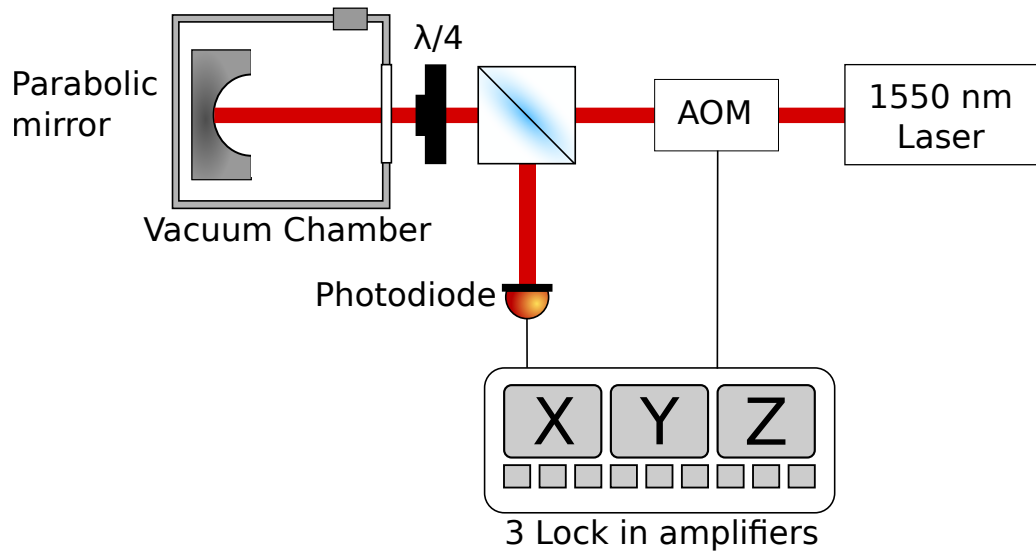


FIGURE 2.9: General experimental setup. The trapping 1550 nm laser passes through an acousto-optical modulator (AOM), a polarising beam splitter (PBS) and a quarter waveplate into the parabolic mirror. There it is focused to generate the trap site. Once a particle is trapped the detection signal travels through the quarter waveplate, so that the polarisation is now in the horizontal plane, and is reflected at the PBS to the photodiode. The detected signal is inputted to the Lock-in amplifiers that contain the PLL system given in Fig.(2.8). The output of the control electronics is then used to modulate the input laser power and slow the particle's motion.

2.7 Cooling

The energy of the particle in a given degree of freedom is $E_i = m(\omega_i + \delta\omega_i)^2 \langle x_i^2 \rangle$, with $\langle x_i^2 \rangle$ given by the integral of the PSD over all frequencies. $\delta\omega_i$ is a result of an effect similar to injection locking, where the centre frequency can shift a small amount when the feedback signal is close to but not exactly at the natural frequency. This should be

minimised to achieve the best cooling but there may always be some small frequency shift. It is known that $\langle x^2 \rangle = \int_{-\infty}^{+\infty} S_{xx} d\omega$ so using Eq.(2.30) as the PSD the energy of a degree of freedom becomes,

$$\begin{aligned}
 E_i &= m(\omega')^2 \langle x^2 \rangle \\
 &= m(\omega')^2 \int_{-\infty}^{+\infty} S_{xx} d\omega \\
 &= m(\omega')^2 \frac{k_b T \Gamma_0}{\pi m} \int_{-\infty}^{+\infty} \frac{d\omega}{((\omega')^2 - \omega^2)^2 + (\Gamma' \omega)^2} \\
 &= m(\omega')^2 \frac{k_b T \Gamma_0}{\pi m} \frac{\pi}{2(\omega')^2 \Gamma'} \\
 &= k_b T \frac{\Gamma_0}{\Gamma_0 + \delta \Gamma}
 \end{aligned} \tag{2.31}$$

where $\omega' = \omega_i + \delta\omega_i$ and $\Gamma' = \Gamma_0 + \delta\Gamma$. Using the equipartition theorem $E = 1/2 k_b T$, this energy can be related to a change in the effective temperature of the nanoparticle's centre of mass motion (T_{com}) as,

$$T_{com} = T \frac{\Gamma_0}{\Gamma_0 + \delta \Gamma}, \tag{2.32}$$

where $T = 300$ K for room temperature. By implementing the feedback system T_{com} can be reduced to sub-kelvin temperatures and the resulting motion amplitude to sub-nanometer. Fig.(2.10) shows a 80 nm, radius, particle that has been cooled from room temperature at 3 mbar down to 3 K at 5×10^{-5} mbar.

If the kinetic energy is reduced sufficiently then the energy becomes quantized and the nanoparticle becomes a quantum harmonic oscillator (QHO) with energy levels given by,

$$E_n = \frac{\hbar \omega'}{2} (n + 1), \tag{2.33}$$

where $n \in \mathbb{Z}^+$ is the energy level. n can be obtained by dividing the kinetic energy by the energy of the ground state for a QHO and recalling the solution for $\langle x_i \rangle$ used in Eq.(2.31).

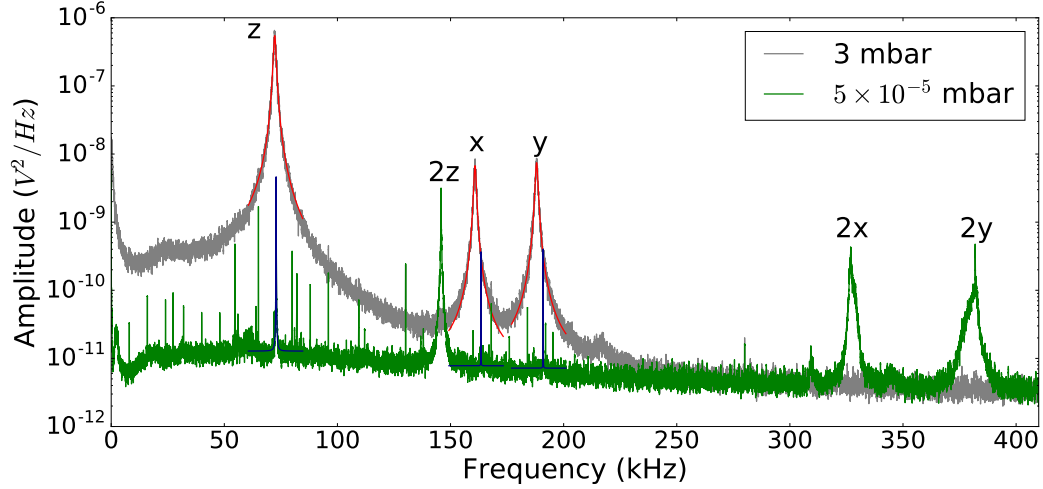


FIGURE 2.10: $\varnothing 100$ nm particle, at 3 mbar and 3.3×10^{-5} mbar. The particle is taken to be 300 K at 3 mbar as there is no cooling and it is able to thermalise with the remaining gas. At 3.3×10^{-5} mbar the cooling is enabled resulting in the large peak seen at twice the respective trap frequencies. The largest cooling is seen for Z, reaching $T_{com} = 3$ mk.

$$\begin{aligned}
 \langle n \rangle &= \frac{k_b T_{com}}{\hbar \omega_0} \\
 &= \frac{k_b T}{\hbar \omega_0} \frac{\Gamma_0}{\Gamma_0 + \delta \Gamma} \\
 &= \frac{k_b T \Gamma_0}{\hbar \omega_0 \delta \Gamma} .
 \end{aligned} \tag{2.34}$$

For Fig.(2.10) this would result in an energy level of $\langle n \rangle \approx 9000$ which is far from quantum. However, $\langle n \rangle < 100$ once $T_{com} < 100 \mu K$ which has been achieved by Jain et. al.[5] and is something others in the group are pushing for. Reaching ground state has implications for the force sensitivity as it results in an increased Q. The quantum force sensitivity will be discussed in more detail in Char.(3.1.2). The PLL helps to reduce the energy of the particle but it also introduces a new source of error due to the limitations of the frequency tracking.

2.8 Frequency Tracking error

The effectiveness of the cooling is dependent on the ability of the PLL to detect and track the natural frequency of the particle. For example, if the frequency changes more than the detection bandwidth, the PLL will not be able to lock to the signal and so that degree of motion would not be cooled. The natural frequency is dependant on laser power, the wavelength of the laser (via beam waist for radial directions) and polarisation

(again via beam waist although the relation is not presented here). All of these can vary by small amounts over time causing the centre frequency to oscillate around an average value. Another big factor is the phase of the two detection arms, that is the scattered and divergent light. The two paths are closely correlated so that changes in one arms should be mirrored in the other but small differences will still occur giving a variation in peak height. All of this together leads to the peak of the PSD looking like Fig.(2.11), where instead of having a single peak as for a Lorentzian curve (the fitting line), the top looks more flat due to multiple peaks. This limits the cooling and so limits the minimum pressure that can be reached. To counter this, a laser with a power stability longer than the measurement time must be used, while still also having minimal noise near the trapping frequencies.

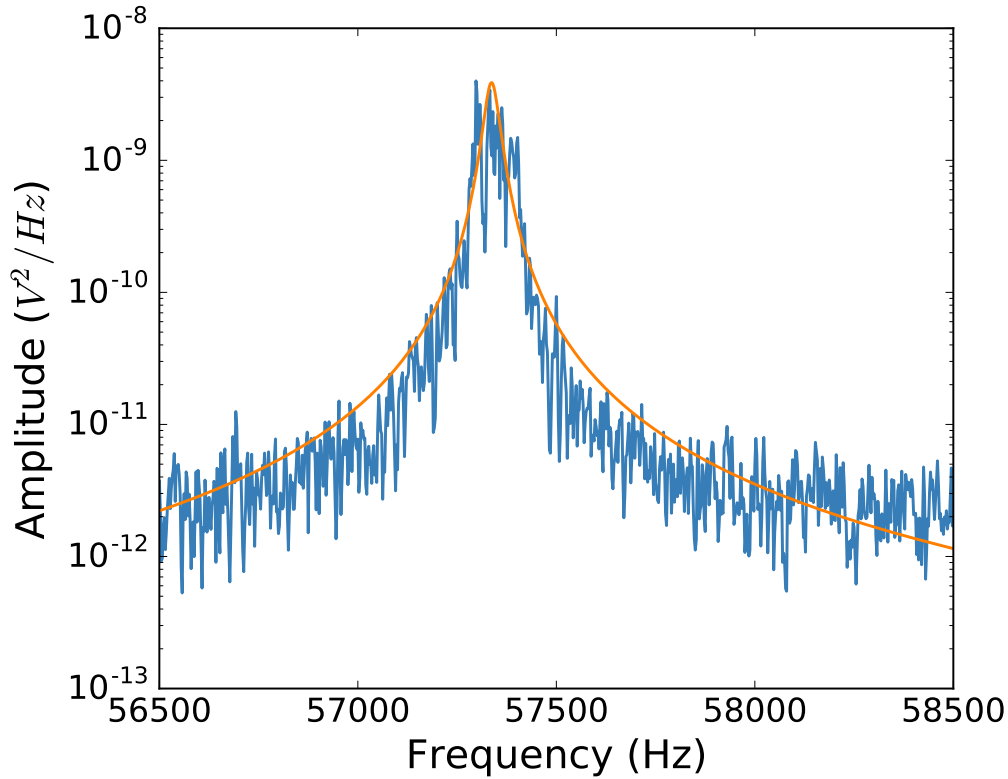


FIGURE 2.11: The z peak at 5×10^{-5} mbar showing the frequency drift that causes the peak to be flat topped. This limits the effectiveness of the cooling and so the minimum pressure that can be reached.

2.9 Phase space

When fitting Eq.(2.26) to the measured PSD there is a required fitting factor to convert from V^2/Hz to m^2/Hz . The conversion factor, γ , therefore has units of m/V and the fitted equation is,

$$Sxx(\omega) = \gamma^2 \frac{k_B T_0}{\pi m} \frac{\Gamma_0}{((\omega_0)^2 - \omega^2)^2 + \omega^2 (\Gamma_0)^2}. \quad (2.35)$$

Once the conversion factor is known, the position of the particle relative to the centre of the motion is simply

$$x_i = V_i / \gamma_i, \quad (2.36)$$

where V_i is the voltage amplitude for a given degree of freedom, $i \in x, y, z$. To get the amplitude for a given degree of freedom the detection signal is passed through a 5th order Butterworth filter from the SciPy python module. This type of filter is designed to have a flat frequency response across the pass band. A sample of time data is shown in Fig.(2.12.A) and then the same data is shown after a 70 ± 10 KHz band filter in Fig.(2.12.B). The time trace is much cleaner after the filter although there is some phase shift due to the way the filter is applied. This phase shift isn't an issue for the work presented here as there is no need to compare data before and after the filter directly.

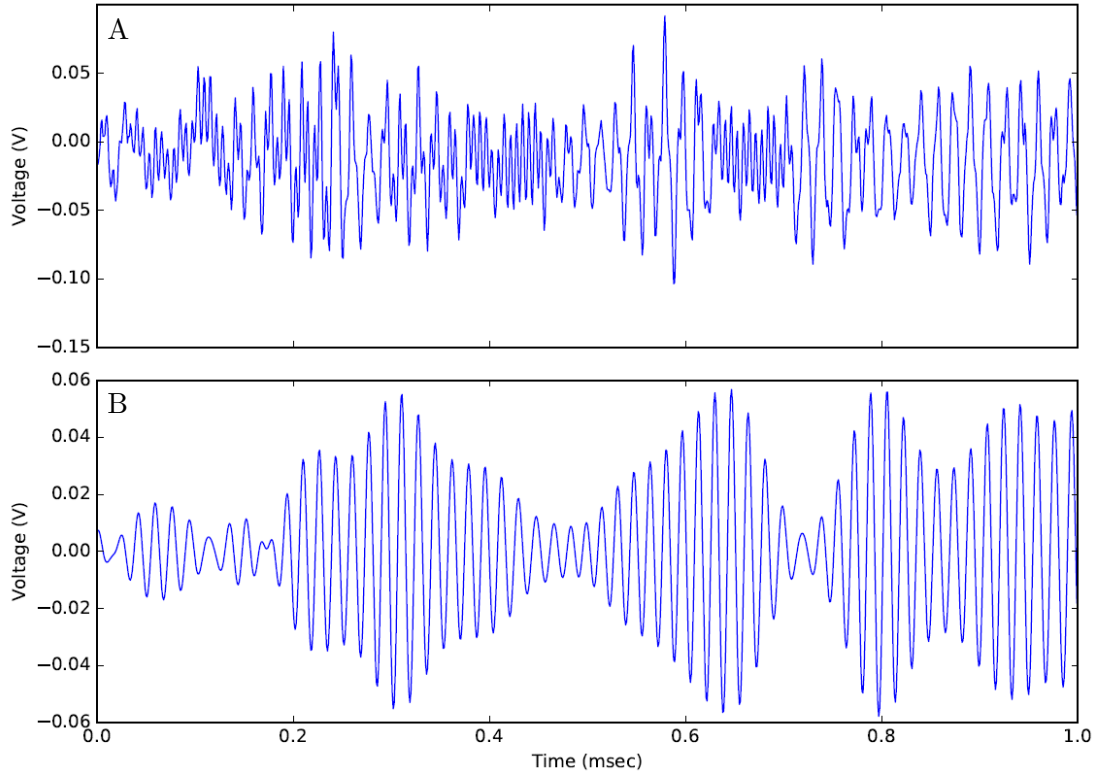


FIGURE 2.12: Time series before (**A**) and after (**B**) the application of a 5 order Butterworth bandpass filter centred at the z trap frequency of 70 kHz with a bandwidth of 10 kHz. There is a phase shift due to this filtering but as we only look at a narrow band and don't compare before and after filter data it shouldn't be an issue.

The velocity of the particle can be computed by the change in the particle's position at the sample frequency. The momentum is then just the product of this with mass,

$$p_i = m f_s \Delta V_i / \gamma_i. \quad (2.37)$$

where f_s is the sampling frequency and $\Delta V = V(t) - V(t + 1/f_s)$. Fig.(2.13) shows the phase space distribution of the z data from Fig.(2.10) where the momentum as be plotted in units of $1/(\omega_i m)$ so that the distribution should be circular if there are no other effects on the particle. There is a notable reduction in the area enclosed by the circle as well as a smoothing of the distribution. The change in the energy of the particle is then related to the change in the area of the two areas. In a phase-space diagram the total energy of the particle is $E = \pi r^2 = \pi(x^2 + (p/m\omega_0)^2)$ where r is the radius of a ring around zero. This allows the change in energy to be measured by simply measuring the change in the FWHM of the 2D Gaussian. This gives circles with radii of $r_{3mbar} = 6$ and $r_{HV} = 0.06$. The final centre-of-mass temperature is then $T = 300 \left(\frac{r_{HV}}{r_{3mbar}} \right)^2 = 0.03$ K, which is in agreement with the earlier method of determining temperature.

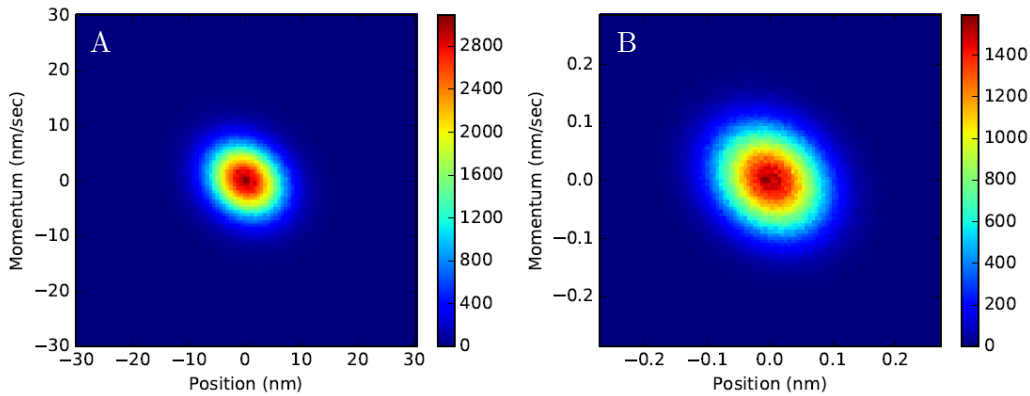


FIGURE 2.13: Phase space histograms with momentum in units of distance. By fitting a 2 dimensional Gaussian the radius can be obtained and used to measure the change in energy. **A:** $r = 6$ at 3 mbar. **B:** At 5×10^{-5} mbar $r = 0.06$ and if the particle is at 300 K at 3 mbar then the temperature is now 0.03 K.

2.10 Non-linear dynamics

The primary function of the PLL is to cool the particle allowing for increased force sensitivity. However, it can also be used to drive the motion into a non-thermal (non-Gaussian) state. To observe this a nanoparticle measuring \varnothing 68 nm was trapped and cooled as normal. Once the pressure was reduced to $\approx 10^{-5}$ mbar another output channel from the PLL was used to drive the particle's motion on resonance and the phase was tuned to maximise the resulting heating effect. This combination of cooling

and heating confines the particle's motion due to the cooling while accelerating it away from the centre due to the driving. The particle therefore spends very little time near the centre of the trap but an increased amount of time near its edges. This results in the emergence of a ring state as shown in Fig.(2.14) where the axis have been normalised against their standard deviation. Just as with the thermal state, these ring states could be pushed to reach a low $\langle n \rangle$, but now with a population inversion which could imply a negative temperature[50]. It is possible, with care, to pump down to high vacuum (HV) without the feedback system at all. In this case, the particle's velocity becomes so large that it spends very little time within the trap centre but now it reaches into the non-linear areas of the trap focus and so ring states form.

Towards the end of the work for this thesis the high power laser began to break down. This resulted in an interesting beam profile where the bright centre varied within the beam. This was mapped into a movement of the focus at a number of time scales. The chamber was evacuated down to 10^{-5} mbar without cooling from the PLL. This produced multiple ring states due to the mixing of the non-linear behaviour and the movement of the trapping site. Fig.(2.15) shows the change in the phase space distribution between the normal ring state and the one resulting from the system described above. This shows multiple rings due to the beating of the two frequencies but these are not stable and change from one instance to the next. This does at least imply that other distributions, for example Lévy noise[51], could be generated by manipulating the position and power of the trap in a more controlled manner.

2.11 Thermalisation rate

Once the particle is cooled the feedback can be turned off and the thermalisation of the particle to room temperature can be observed. This thermalisation is driven by the random collisions with air particles, but it would also be sensitive to any other external driving forces. However, if the feedback is off for too long then the particle will enter the non-linear regime, as discussed above, and can quickly be expelled from the trap. To prevent this, the feedback is generally just pulsed off for 1 second. That said, if the non-linear motion can be modelled and the particle retained reliably, then the non-linear motion could be more sensitive as there is a larger signal change expected for a given applied force. An attempt to measure the re-heating rate is shown in Fig.(2.16), where the cooling of Z has been pulsed off for 0.5 sec. The switch off and switch on timing of the PLL is not reliable at these resolutions due to network delays, so that the scans had to be aligned in post-processing. This re-alignment is shown in Fig.(2.16.A) but also shows the other difficulty. The time it takes for the particle to become non-linear also varies

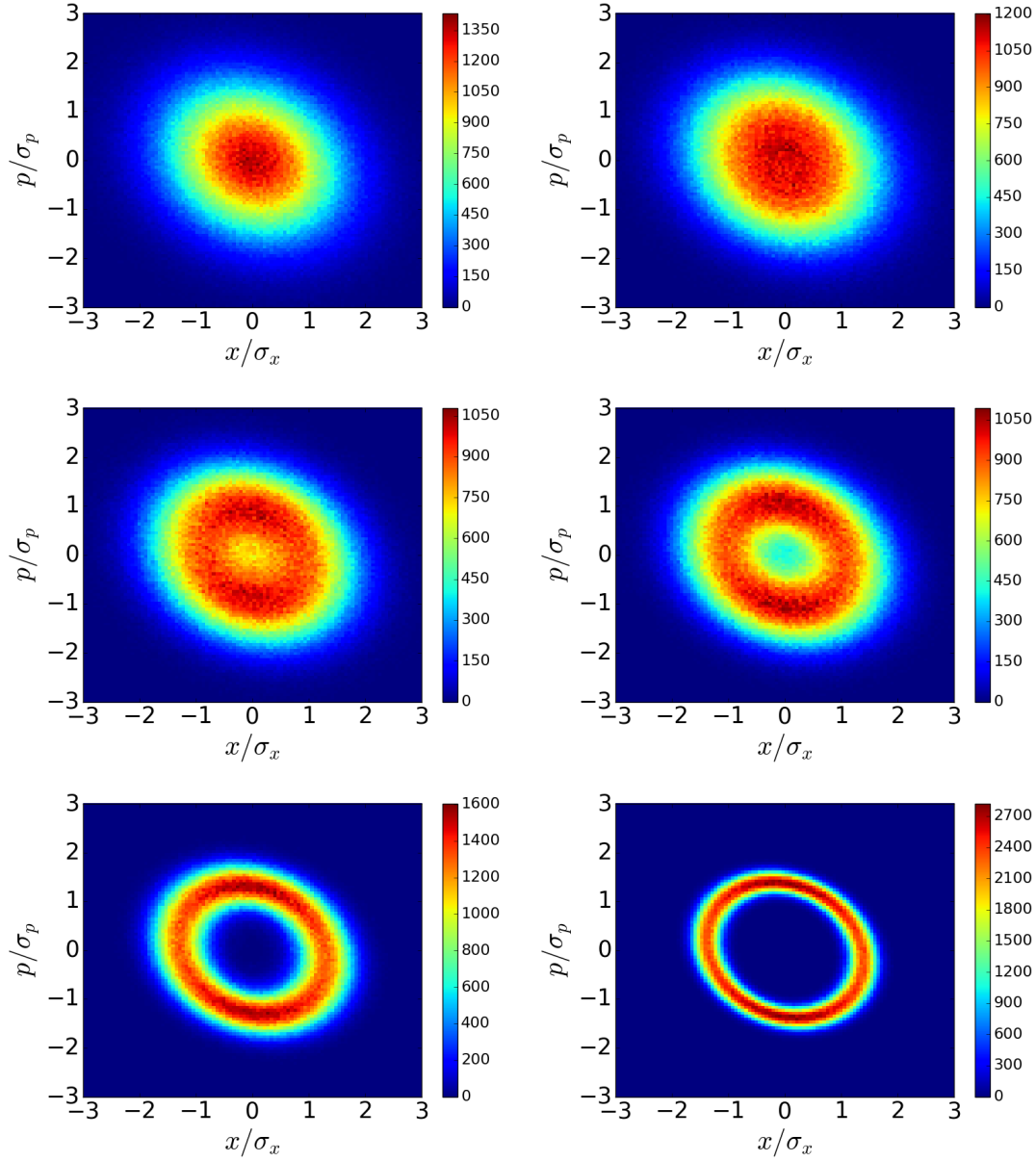


FIGURE 2.14: $\varnothing 68$ nm particle at 10^{-5} mbar. The particle is cooled as normal with the PLL but it is also driven by a second PLL output. This results in the particle being confined by the cooling but accelerated through the focus so that it spends very little time in the centre of the trap. As the driving and cooling is increased the Gaussian thermal state transitions into a non-thermal ring state.

considerably, and it is even possible for the random kicks to knock the particle back into the linear regime. Taking the simple assumption that the heating rate is similar to a decay function, the maximum amplitude is given by,

$$z_{max} = z_{300}(1 - e^{-\Gamma_t t}), \quad (2.38)$$

where z_{300} is the amplitude at 300 K, t is time, and Γ_t is the reheating rate. Fitting

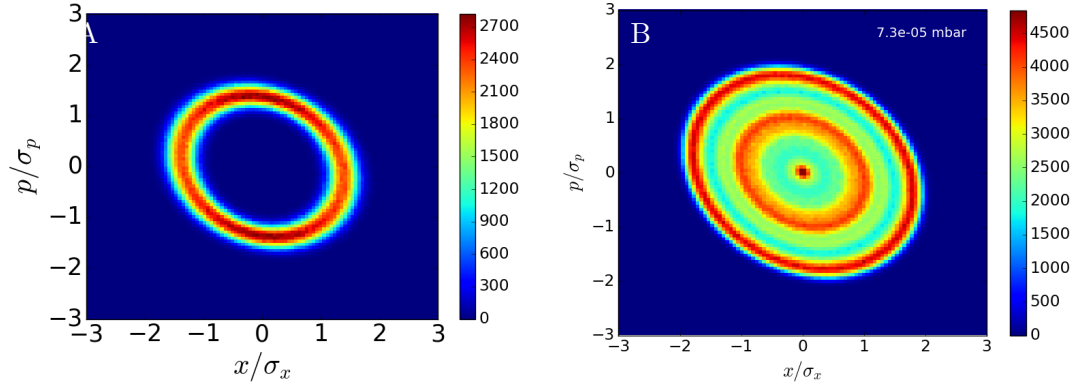


FIGURE 2.15: **A:** \varnothing 68 nm particle with 24 mV cooling and 2.5 mV driving at 10^{-5} mbar. This results in a clear single ring state with minimal centre states. **B:** \varnothing 52 nm with no cooling or driving at 10^{-5} mbar. The laser focus was varying in time randomly which results in a beating between the multiple focus oscillation frequencies and the trap frequency. Here we see two rings and a small central peak but these are stable in time and the whole distribution changes from instant to instant.

this to the curve in Fig.(2.16.B) gives a rate of 4.3 Hz, although given the amount of variation in the scans this is only an estimate.

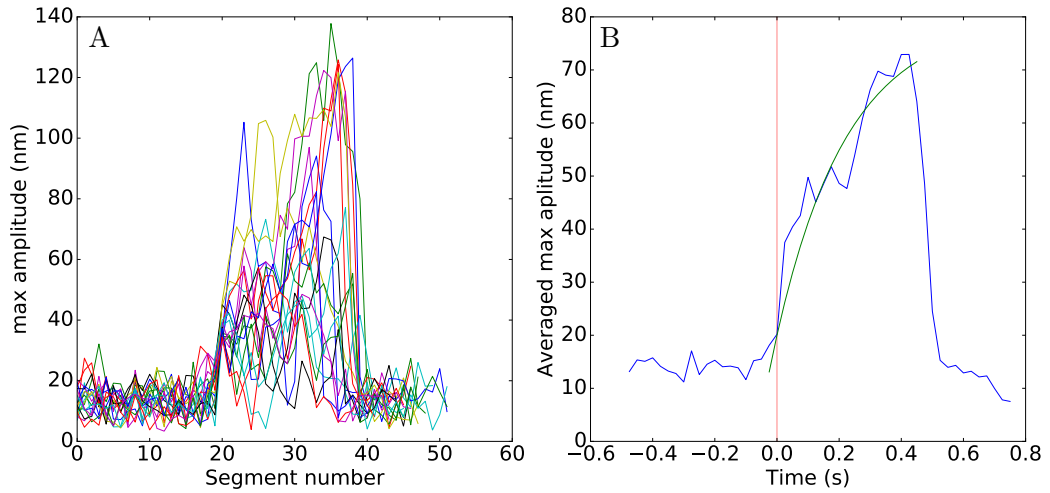


FIGURE 2.16: **A:** 20 thermalisation scans. These have been aligned in post. The delay between triggering the cooling to turn off and when the control electronics turns off is unpredictable due to network lag. For this reason the x axis is offset for each line but also the time at which the cooling turns back on again is also unpredictable. For each scan the time data is cut into 200 sections of 0.05 seconds and a PSD taken. The y axis is then the maximum value converted into displacement. **B:** Mean of the aligned re-thermalisation runs gives a reheating rate of 4.3 Hz. Due to the large variation in the runs, this number is only an approximation at best. A more reliable method of controlling the PLL system is need to progress with this as a method of force detection.

2.12 Conclusion

This chapter has detailed the physics and practical aspects of optically trapping silica nanoparticles. A full mathematical description is given for the particle's motion in the optical trap and for the trapping potential itself. The particle's motion is detected using a balanced photodiode and an interferometric setup. The scattered light from the particle is mixed with the divergent light to give a homodyne-like detection method that measures the phase difference of the mixed beams. This allows for high resolution position measurements of the particle's motion even near the ground state. By fitting Eq.(2.26) at 3 mbar it was possible to obtain both the radius of the particle and the conversion constant (γ). Once a particle has been trapped and characterised the centre-of-mass motion can be cooled using a PLL to modulate the laser power at twice the trapping frequency. With this cooling system it was possible to reach $T_{com} = 0.03$ K for the z degree of motion. This is measured by fitting both the PSD equation (Eq.(2.26)) and verified by changes in phase-space. By using γ to convert the voltage signal to position and Eq.(2.37) to obtain the momentum, a phase-space heat map was produced showing the reduction in area as the particle is cooled. By mapping the change in area, the change in T_{com} was verified, but there was another interesting effect that can be observed with the phase-space diagrams. By driving the particle in-phase with another PLL channel it was possible to confine the motion, while also driving the particle through the focus. This produced non-Gaussian ring states as shown in Fig.(2.14), where the particle now has a greater chance of being outside the trap centre than within it. The width of these ring states can be reduced by increasing both the cooling and driving rates, and at high levels could lead to a low $\langle n \rangle$ state just as with the Gaussian distributions. Ring states can also be generated by simply turning off the cooling at low pressures, and then letting the system self drive out of the linear regime. The position of the focus can also be manipulated to produce interesting phase-space distributions. Fig.(2.15) shows a higher order ring state mode that was generated by an unstable laser towards the end of its operational life. While this state was unstable, it does demonstrate the possibility of manufacturing other effective potentials by changing both laser power and focus position. Finally the re-thermalisation rate was approximated by pulsing the PLL off for 0.5 seconds. There were problems with timing but a value of 4.3 Hz was measured for the reheating rate. Once the timing issues have been resolved this method holds promise for force detection as all forces drive the particle in some way and so the reheating should be sensitive to this. With this understanding of the optomechanical system in normal operating conditions it is now possible to see how external forces affect it, and just how low the sensitivity really goes.

Chapter 3

Force detection

3.1 Sensitivity

For a force to be detectable the change in the resulting signal must be greater than the noise. The largest source of classical noise on the particle is from the thermal noise,

$$\sigma_{th} = F_{th} = \sqrt{\frac{4k_B T m \omega_0}{Q}}, \quad (3.1)$$

where m is the mass of the particle, T is the temperature of the environment, ω_0 is the trap frequency and Q is the quality factor[52]. The Q factor has been used in place of Γ_0 as in Eq.(2.25) as this more accurately represents the cooling from the PPL. This thermal noise comes from Brownian motion, where T is the temperature of the gas, i.e. it represents the random collisions between the particle and the air particles. From our paper, we claimed a position resolution of $200 \text{ fm}/\sqrt{Hz}$ which gives a force sensitivity of $2 \times 10^{-21} \text{ N}/\sqrt{Hz}$ using $F_{sense} = m x_{sense} (\omega/2\pi)^2$. This is in approximate agreement with that predicted by Eq.(3.1) for that particle, $3.9 \times 10^{-21} \text{ N}/\sqrt{Hz}$. This shows that the thermal limit had been reached for that particle, and so to progress the pressure or temperature of the chamber would need to be reduced. Tab.(3.1) gives an idea of the sensitivity for different parameters and Fig.(3.1) shows this graphically as a function of integration time. By using cryogenic cooling, a smaller particle and increasing Q to 10^9 , it should be possible to reach a sensitivity of $10^{-24} \text{ N}/\sqrt{Hz}$. This will be explored in the next subsection as quantum noise needs to be considered at this level of sensitivity. Interesting though, for forces that scale with mass it is generally better to use a larger particle, as the decrease in sensitivity is offset by the increase in the force itself. This applies to both gravity and spin forces (which scales with the number of particles) but it does not apply to electric forces, where the force scales with the charge-mass ratio.

System	Diameter	Trap freq	Q	Force sensitivity
Current	100 nm	100 KHz	10^7	$10^{-20} \frac{N}{\sqrt{Hz}}$
Large particle	$1 \mu m$	100 KHz	10^9	$10^{-20} \frac{N}{\sqrt{Hz}}$
Small particle	10 nm	100 KHz	10^9	$10^{-23} \frac{N}{\sqrt{Hz}}$
Small particle at 3k	10 nm	100 KHz	10^9	$10^{-24} \frac{N}{\sqrt{Hz}}$

TABLE 3.1: Sensitivities for different combinations of particle size, Q and air temperature. The smallest particle has the best sensitivity but there maybe times when a larger particle would be preferable as some forces scale faster with radius than the drop off in sensitivity.

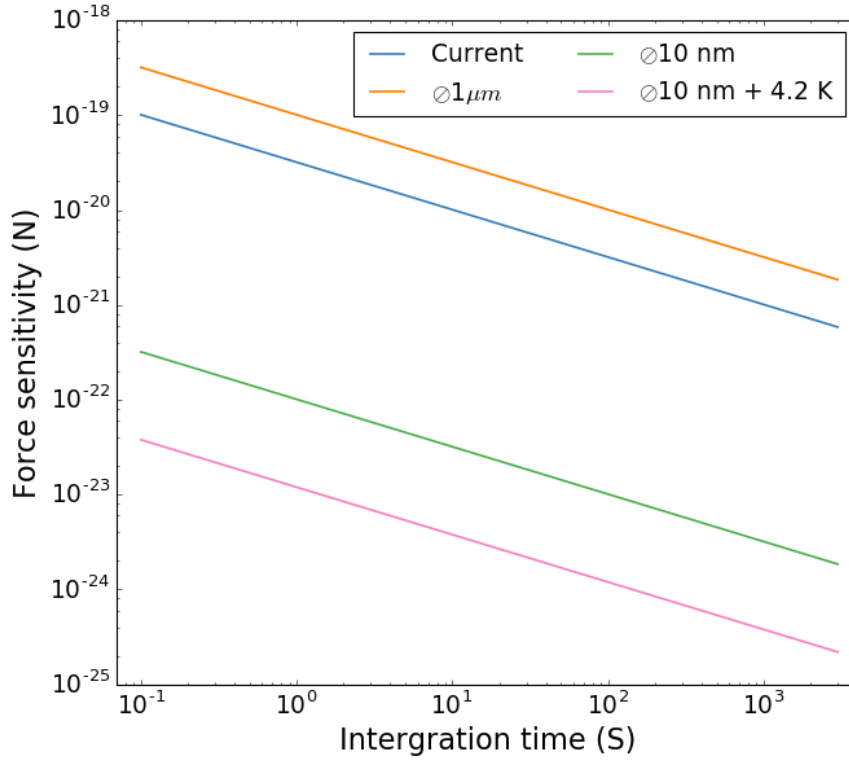


FIGURE 3.1: Minimal detectable force due to thermal noise for different conditions. The larger particle has reduced sensitivity but may be preferable if the force scales with mass. A $\varnothing 10$ nm particle at 4.2 K has the best sensitivity likely to achieved, approaching 10^{-25} N after an hour of integration time.

3.1.1 Standard quantum limit

Once the system approaches the quantum regime it can be described by the Hamiltonian for a quantum harmonic oscillator,

$$\hat{H} = \frac{m\omega_0^2}{2}\hat{x}^2 + \frac{\hat{p}^2}{2m} \quad (3.2)$$

where \hat{x} is the position operator and \hat{p} is the momentum operator. To simplify some of the later maths let,

$$\hat{X} = \hat{x} \sqrt{\frac{m\omega_0}{\hbar}} \quad (3.3)$$

$$\hat{P} = \frac{\hat{p}}{\sqrt{m\hbar\omega_0}}. \quad (3.4)$$

The Hamiltonian can then be written as,

$$\hat{H} = \frac{\hbar\omega_0}{2}(\hat{X}^2 + \hat{P}^2) \quad (3.5)$$

but this can be taken one step further using a pair of operators,

$$\hat{a} = \frac{1}{\sqrt{2}}(\hat{X} + i\hat{P}) \quad (3.6)$$

$$\hat{a}^\dagger = \frac{1}{\sqrt{2}}(\hat{X} - i\hat{P}), \quad (3.7)$$

so that the Hamiltonian then becomes,

$$\hat{H} = \hbar\omega_0(\hat{a}^\dagger\hat{a} + 1/2) \quad (3.8)$$

where \hat{a} is the "lowering" operator as it lowers the system by one level and \hat{a}^\dagger is the raising operator as it raises the energy level. They also have the relation that the commutator is 1, $[\hat{a}, \hat{a}^\dagger] = 1$, and that $\hat{a}\hat{a}^\dagger|n\rangle = n|n\rangle$ where $|n\rangle$ is some number state. These relations are proven in Appendix.(D). If \hat{a} lowers the state then at the ground state it will give 0 as there is no lower state, i.e. $\hat{a}|0\rangle = 0$. With this the ground energy can be obtain,

$$\begin{aligned} E_0 &= \langle 0 | \hat{H} | 0 \rangle \\ &= \langle 0 | \hbar\omega_0(\hat{a}^\dagger\hat{a} + 1/2) | 0 \rangle \\ &= \hbar\omega_0(\langle 0 | \hat{a}^\dagger\hat{a} | 0 \rangle + 1/2 \langle 0 | 0 \rangle) \\ &= \frac{\hbar\omega_0}{2}, \end{aligned} \quad (3.9)$$

which for a particle at 100 kHz gives $6.6 \times 10^{-29} J$ or $4.7 \mu K$ as $T = \frac{\hbar\omega_0}{k_B}$. The position operator can also be redefined using the raising and lowering operators,

$$\hat{x} = \sqrt{\frac{\hbar}{2m\omega_0}}(\hat{a}^\dagger + \hat{a}). \quad (3.10)$$

The standard deviation (Δx) of the position gives the minimum position resolution for a given energy level. Generally, $\Delta x = \sqrt{\langle x^2 \rangle + \langle x \rangle^2}$ but for this work $\langle x \rangle = 0$ so only the first term is important. At the ground state this is known as the standard quantum limit (SQL) and is given by,

$$\begin{aligned} \Delta x &= \sqrt{\langle x^2 \rangle} \\ &= \sqrt{\langle 0 | x x | 0 \rangle} \\ &= \sqrt{\frac{\hbar}{2m\omega_0} \langle 0 | (\hat{a}^\dagger + \hat{a})^2 | 0 \rangle} \\ &= \sqrt{\frac{\hbar}{2m\omega_0} \langle 0 | (\hat{a}^\dagger \hat{a}^\dagger + \hat{a} \hat{a} + \hat{a}^\dagger \hat{a} + \hat{a} \hat{a}^\dagger) | 0 \rangle} \\ &= \sqrt{\frac{\hbar}{2m\omega_0} \langle 0 | \hat{a} \hat{a}^\dagger | 0 \rangle} \\ &= \sqrt{\frac{\hbar}{2m\omega_0} \langle 0 | (\hat{a}^\dagger \hat{a} + 1) | 0 \rangle} \\ &= \sqrt{\frac{\hbar}{2m\omega_0}}, \end{aligned} \quad (3.11)$$

where the relations $\langle i | j \rangle = 0$ if $i \neq j$, $\hat{a} | 0 \rangle = 0$, and the commutator have been used. Assuming that position and momentum are measured equally, then the uncertainly relation, $\Delta x \Delta p = \hbar/2$, can be used to get the Δp ,

$$\begin{aligned} \Delta p &= \frac{1}{\Delta x} \frac{\hbar}{2} \\ &= \sqrt{\frac{\hbar m \omega_0}{2}}. \end{aligned} \quad (3.12)$$

Eq.(3.11) gives a position resolution of $3.8 \times 10^{-12} m$ for a $\oslash 100$ nm particle at 100 KHz and Eq.(3.12) gives a momentum resolution of $5.5 \times 10^{-24} \text{ kg m/s}$.

3.1.2 Quantum force detection

If it was possible for the particle to be in a state so that $\langle n \rangle \approx n$, then it may be possible to implement a quantum measurement protocol. This is a very difficult experimentally and it is not clear if it is even possible, however it is an interesting idea to explore. The following is based on a review by Degen et al.[53], where it is assumed that the Hamiltonian is given by,

$$\hat{H} = \hat{H}_0 + \hat{H}_v(t) \quad (3.13)$$

where \hat{H}_0 is the normal Hamiltonian given in Eq.(3.8) and \hat{H}_v is the Hamiltonian associated to some external signal $V(t)$. For simplicity, it is assumed that there are just two energy levels that the system can be in, $|0\rangle$ and $|1\rangle$. $V(t)$ is also assumed to be small so that it adds a perturbation to \hat{H}_0 and so can be split into two parts,

$$\hat{H}_v(t) = \hat{H}_{v\parallel}(t) + \hat{H}_{v\perp}(t) \quad (3.14)$$

where $\hat{H}_{v\parallel}(t)$ is the parallel (commuting, secular) component and $\hat{H}_{v\perp}(t)$ is the transverse (non-commuting) component. The form for these can be assumed without loss of generality,

$$\hat{H}_{v\parallel}(t) = \frac{1}{2}\gamma V_{\parallel}(t)(|1\rangle\langle 1| - |0\rangle\langle 0|) \quad (3.15)$$

$$\hat{H}_{v\perp}(t) = \frac{1}{2}\gamma(V_{\perp}(t)|1\rangle\langle 0| - V_{\perp}^{\dagger}(t)|0\rangle\langle 1|) \quad (3.16)$$

$$(3.17)$$

where $V_{\parallel}(t)$ and $V_{\perp}(t)$ are the relative potentials and γ is the coupling constant. To give examples of common coupling constants, this could be the gyromagnetic ratio for spins in a magnetic field or the linear Stark shift parameter for electric dipoles in an electric field. The parallel and transverse components have different effects. The former shifts the energy levels and changes the transition frequency. While the later can induce transitions between levels by increasing the transition rate. This generally requires a time dependant signal that is resonance with the transition frequency.

These ideas are all still dependant on being able to reach a state where $\langle n \rangle \approx n$ and it is unclear if the sensitivity will even be increased in doing so. What is clear though, is that

reducing the temperature of the surrounding gas will result in a reducing in Brownian noise.

3.1.3 Ground state thermal noise

If all of the classical limitations have been overcome then there are still quantum effects that limit the sensitivity that can be achieved. To see this let's take a force that has the form,

$$F(t) = F_0 \sin(\Omega_0 t), \quad (3.18)$$

where F_0 is the amplitude, Ω_0 is the forces resonant frequency and t is time. If the duration of the force is τ then the force is pulsed when $\Omega_0 \tau < 1$ and a constant wave (CW) force when $\Omega_0 \tau \gg 1$. For all of the work presented here it is enough to focus on CW forces but work has been done by others in the group on pulses. The integration times will also be long relative to both the trap frequency and the force duration.

If the air particles in the vacuum chamber are colder than the c.o.m temperature of the nanoparticle, then thermal energy will flow from the nanoparticle into the remaining air. If this additional heat is not removed then the air will heat up to the same temperature as the nanoparticle. At ground state this gives the zero temperature heat reservoir[54],

$$\sigma_{ZTHR} = \sqrt{4\hbar m \Omega_0 \Gamma_0}, \quad (3.19)$$

where $k_B T$ in Eq.(3.1) has been replaced with the ground state energy, $\hbar \Omega_0$. For higher energy levels this would also include the factor of $(n + 1/2)$. This gives a lower limit for the $Q = 10^9$ system of $4.6 \times 10^{-25} \text{ N}/\sqrt{\text{Hz}}$. However, there are a number of other noises that need to be overcome before this limit can be tackled.

3.1.4 Photon recoil

Every time a photon scatters off the nanoparticle there is a momentum transfer up to $p = h/\lambda$ depending on the angle of scatter. As this angle is quasi-random (there is a small preference in the forward direction) the resulting force can be equated to a stochastic driving force. Starting with the equation for Rayleigh scattering cross-section used earlier, Eq.(2.6), and the polarisability, Eq.(2.10), the power of the scattered photons comes out to be,

$$P_{scatt} = \sigma_R I_0 = \frac{128\pi^5}{3} \frac{r^6}{\lambda^4} \left(\frac{n^2 - 1}{n^2 + 2} \right)^2 I_0, \quad (3.20)$$

where r is the radius of the nanoparticle and I_0 is the intensity at the laser focus given by,

$$\begin{aligned} I_0 &= \frac{2P_0}{\pi w_0^2} \\ &= \frac{8P_0(NA)^2}{\pi \lambda^2}, \end{aligned} \quad (3.21)$$

where P_0 is the laser power and w_0 is the beam waist at the focus. Combining Eq.(3.20) and Eq.(3.21) for a $r = 50 \text{ nm}$ particle in a 1 W laser focus with an NA of 0.9 gives $P_{scatt} = 2.4 \text{ } \mu\text{W}$. From Jain et al.[5] the photon recoil heating rate is,

$$\gamma_{recoil} = \frac{1}{5} \frac{2\pi P_{scatt}}{mc\lambda\Omega_0}, \quad (3.22)$$

where m is the mass of the particle and c is the speed of light. For the above example this gives a recoil heating rate of $\gamma_{recoil} = 2\pi \times 2.1 \text{ kHz}$ with a trap frequency of $\Omega_0 = 2\pi \times 100 \text{ kHz}$. If all the momentum of the photons are transferred to the particle then this results in a force of $3.4 \times 10^{-24} \text{ N}$. Given the strong dependence on the particle's radius the recoil force can vary from 4.3×10^{-25} to $1.1 \times 10^{-23} \text{ N}$ for a radius change from 25 nm to 75 nm. This is similar to the distribution range seen for the 50 nm radius particles used in this thesis and shows the importance in measuring the radius accurately. If all other sources of driving are less than this then the minimum occupation level is given by $n = \gamma_{recoil}/\delta\Gamma = 20$. It would therefore be impossible to reach ground state with a $\text{O}100 \text{ nm}$ particle and it would be much worse for larger particles. For smaller particles the recoil force drops off very quickly because of the overall $\gamma_{recoil} \propto r^3$ relation and so isn't the limitation of the system. There are other practical limitations that might introduce noise and prevent ground state cooling and limit force sensitivity. The difficulty with the frequency tracking of the PPL has already been discussed but there are more fundamental challenges in the form of 1/f noise, Johnson-Nyquist (thermal) noise, and shot noise.

3.1.5 Detector noise

There are many sources of electrical noise, from thermal fluctuations to reflections from impedance mismatching. This noise, often described as pink noise or $1/f$ noise, is caused by the condensed matter interactions within the detector. These include fluctuating configurations of defects in metals, trapped charges in semiconductors, and domain structures in magnetic materials. These interactions have a relatively large activation energy leading to a low rate in the Arrhenius equation,

$$\gamma_{pink} = A_0 e^{\frac{-E_A}{k_B T}}, \quad (3.23)$$

where γ_{pink} is the rate at which the interaction will occur, A_0 is a constant for each chemical reaction, E_A is the activation energy in joules, T is temperature and k_B is the Boltzmann factor. If the distribution of activation energies is uniform then the resulting frequency distribution is exactly $1/f$. It can be seen that decreasing the temperature would decrease the rate but it would also decrease other sources of noise, for example the Johnson-Nyquist noise found in all electrical devices. This is an application of the fluctuation-dissipation theorem to the motion of the electrons in the device, and it gives the variance in the output voltage of the detector as,

$$\sigma_{thermal} = \sqrt{4k_B T R \Delta f}, \quad (3.24)$$

where R is the resistive load and Δf is the detection bandwidth taken as $10 \times 2\pi \times \omega_0$ to satisfy the Nyquist limit. This represents the random motion of the charges in the detector due to their thermal kinetic energy. Assuming a resistive load of $50 \, \Omega$ the detector noise is $0.88 \, \mu V$ at 300 K. Many specialist detectors use some form of cooling to mediate this affect with the most sensitive using cryogenic liquids. Once these levels of sensitivity have been reached then shot noise might become an issue if the detection voltage is very low. This arises when the statistical uncertainty, variance, in the number measuring events is significant when compared to the number of measurement events. Using the Poisson distribution this can be given mathematically as,

$$\Delta N \approx \sqrt{N}, \quad (3.25)$$

where N is the number of measurement events. Even at ground state the number of photons scattered by the particle is of the order $10^{11} \, s^{-1}$, however, the phase difference between the scattered photons at the centre and those at the extremes of the particle's

motion becomes small. As the detection system is interferometric this results in a small detection signal. The number of electrons for a given current is $N_e = i/e$, where e is the elementary charge. This gives the variance in the detected voltage as,

$$\sigma_{shot} = R\sqrt{2ei_{det}\Delta f}, \quad (3.26)$$

where i_{det} is the output current of the detector, R is the resistive load, and Δf is the detection bandwidth as before. The current generated by the detector is given by,

$$\begin{aligned} i_{det} &= \chi A_{det} I_{det} \\ &= \chi p_{scatt}, \end{aligned} \quad (3.27)$$

where χ is the responsivity of the detector (1 A/W for the balanced photodiode used here), A_{det} is the area of the detector, I_{det} is the intensity of light on the detector, and p_{scatt} is the scattered power from the particle. Using the relation $I_{dec} = 1/2c\epsilon_0|E|^2 = p_{scatt}/A$ it can be seen that $p_{scatt} \sin(\phi) \propto |E|_{scatt}^2 \sin(\phi)$ so the change in current as the particle moves is,

$$\Delta i_{det} = \chi p_{scatt} \sin(\Delta\phi), \quad (3.28)$$

where $\Delta\phi = 2\pi\Delta x/\lambda$. For the SQL where $\Delta x = 8.9 \times 10^{-12}$ m then $\Delta\phi = 3.6 \times 10^{-5}$ rad/s. With a 10^5 V/A transimpedance gain this gives a detection voltage of $8.7 \mu V$ with a shot noise error from Eq.(3.26) of $0.24 \mu V$. However, this assumes that all of the back-scattered light is collected. From fitting it is known that only 1% of the total light scattered by the particle results in a detection voltage, with the rest lost through other scattering/absorption events before the light reaches the detector. At ground state the detection voltage will therefore be 87 ± 2 nV with the error given just by shot noise. This shows that shot noise could be a problem if the laser power has to be lowered to reduce photon recoil, however at present it is not believed to be a limiting factor.

Bring these detection noise sources together gives Fig.(3.2) where the amplifier noise is given by Eq.(3.24). It is clear the the amplifier noise will be a problem once the phonon energy level nears $\langle n \rangle = 36$ and a cooled detector would be required. Comparing this to the force sensitivity shows that the system has great potential to detect ultra-small forces, with the current limits being imposed by technology rather than physics. With this in mind the next section will explore what kind of forces this system can detect.

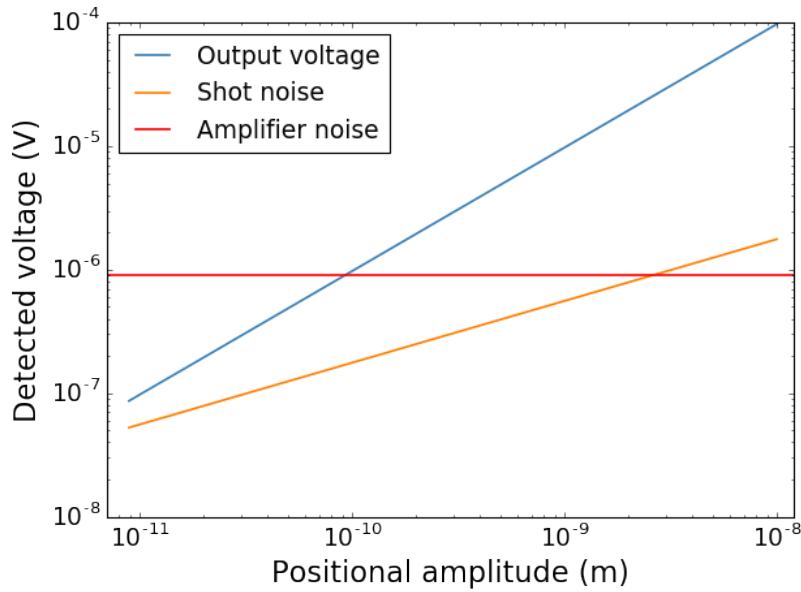


FIGURE 3.2: Total noise contributions against amplitude. As the particles motion is cooled, it is likely to reach the detector noise limit at $\langle n \rangle = 36$ but should not be limited by shot noise.

3.2 Coulomb force

Electrical forces are a natural starting point for force detection in levitated optomechanics. It is a strong force that is well understood and also relatively easy to control with some groups even using it as the cooling mechanism[55]. This thesis will focus on the Coulomb force. The setup is given in Fig.(3.3.A) where a sharp and polished steel needle (see Fig.(B.2) for design) is placed a distance from the trap centre. A potential is then applied to the needle, at vacuum, so that the needle becomes charged. To check the electric field a comsol simulation was made, with Fig.(3.3.B) showing the electric field for a potential of 1000 V. The electric field at the focus of the mirror is ≈ 500 V/m which will be used to compare measured values later. It is also interesting to see that the field lines curve around the earthed mirror. This will lead to some differences between the computational and analytical solutions but it is still interesting to follow them both through. The vacuum chamber is kept at high vacuum when the high voltage is on to prevent electrical and corona discharge.

3.2.1 Electrostatic field - Mean position

As the potential is uniform across the needle, the largest charge will be at the tip due to its small radius. This charge can be obtain from Gauss's law if the tip is approximated as being a sphere with a radius equal to half the tips width,

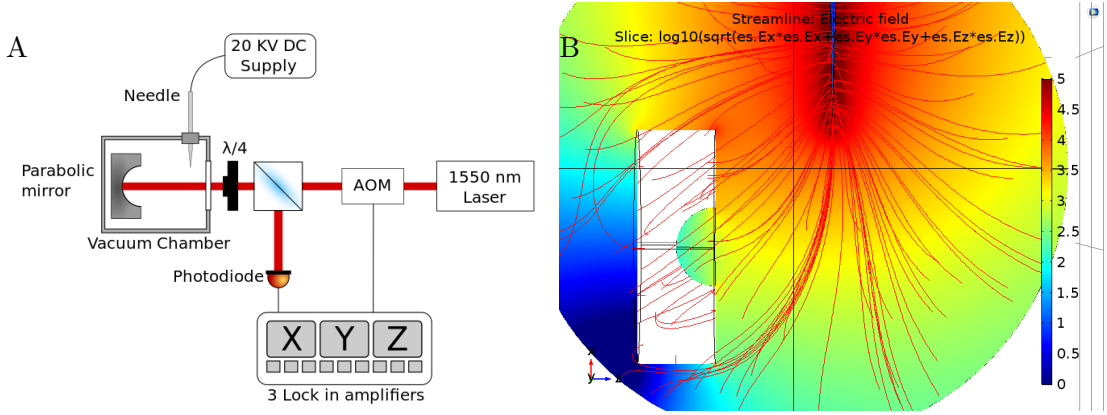


FIGURE 3.3: **A:** Setup of the electric fields experiment. A stainless steel needle is placed in the chamber and connected to a HV power supply. The distance from the needle to the trap is $z = 27$ mm, $y = 28$ mm, $z = 0.5$ mm and the needle tip has a radius of $100 \mu\text{m}$. **B:** Electric field from the needle at 1000 V. The field at the trap site is ≈ 500 V/m and it can be seen that the field lines curl around the earthed mirror.

$$\begin{aligned}
 \frac{q_t}{\epsilon_0} &= \oint_s \mathbf{E} \cdot \mathbf{s}_t \\
 \frac{q_t}{\epsilon_0} &= \oint_r \mathbf{E} \cdot 4\pi r_t d\mathbf{r}_t \\
 \frac{q_t}{\epsilon_0} &= \oint_r \frac{dv}{dr} \cdot 4\pi r_t d\mathbf{r}_t \\
 \frac{q_t}{\epsilon_0} &= \int_V 4\pi r_t dv \\
 q_t &= 4\pi\epsilon_0 r_t V,
 \end{aligned} \tag{3.29}$$

where r_t is the tip radius, q_t is the charge on the needle, V is the applied voltage, S is the Gauss surface and ϵ_0 is the vacuum permittivity. $\mathbf{E} = -\nabla V$ has also been used to get from electric field to applied voltage. This is a familiar result and it can then be inserted into the equation for Coulomb's force.

$$\begin{aligned}
 F_c &= \frac{q_p q_t}{4\pi\epsilon_0 d^2} \\
 &= \frac{q_p V r_t}{d^2},
 \end{aligned} \tag{3.30}$$

The Coulomb force is not a restorative force and so the average position shifts to a new trap centre. The displacement of the average position can be studied by looking for where the trapping force balances the Coulomb force. For most of this work it is simpler

to focus on one degree of freedom, in this case z . The time average equation is now non-zero,

$$k_z \langle z \rangle = \frac{qVr_t}{d^2}, \quad (3.31)$$

where $k_z = \omega_z^2 m$ is the trap stiffness in the z direction and $\langle z \rangle$ is the average position from the trap centre. Letting $d = d' - \langle z \rangle$ where d' is the fixed distance from the needle tip to mirror focus. Substituting this into Eq.(3.31) and re-arranging gives,

$$\begin{aligned} \omega_z^2 m \langle z \rangle &= \frac{qVr_t}{(d' - \langle z \rangle)^2} \\ \langle z \rangle (d' - \langle z \rangle)^2 &= \frac{qVr_t}{\omega_z^2 m} \\ \langle z \rangle d'^2 + \langle z \rangle^3 - 2d' \langle z \rangle^2 &= \frac{qVr_t}{\omega_z^2 m} \\ \langle z \rangle &= \frac{qVr_t}{\omega_z^2 m d'^2}, \end{aligned} \quad (3.32)$$

where $\langle z \rangle^2$ and $\langle z \rangle^3$ are taken to be small enough to be ignored. This displacement will result in a change in the DC level from the photodiode, that can then be mapped onto the 3 degrees of freedom using trigonometry. The z displacement for a $\varnothing 82$ nm particle is shown in Fig.(3.4.A) where the voltage was varied from 0 V to 10 kV and back down to 0 V. The particle has a charge of 50 ± 20 elementary charges and has a maximum displacement of 71 nm. The theory for a similar particle is given in Fig.(3.4.B) where the charge is varied, showing that even for 100's of charges the particle should still be within the $\approx 1.5 \mu m$ trap. Fig.(3.4.C) shows the displacement as a phase space distribution. The distribution maintains its circular shape but there is an increase in T_{com} as the cooling efficiency drops off as the particle moves away from the trap centre.

A charge of 50e gives a force of 1×10^{-15} N at 1000 kV, which is the smallest voltage that resulted in an observable voltage change. The reason for this low sensitivity is that there are a lot of slow time scale variations in the detection signal even without an applied field. This limits the usefulness as a force sensor for the average position detection method and makes oscillating forces strongly preferable. However, there is one other effect that might also be useful for detecting static fields.

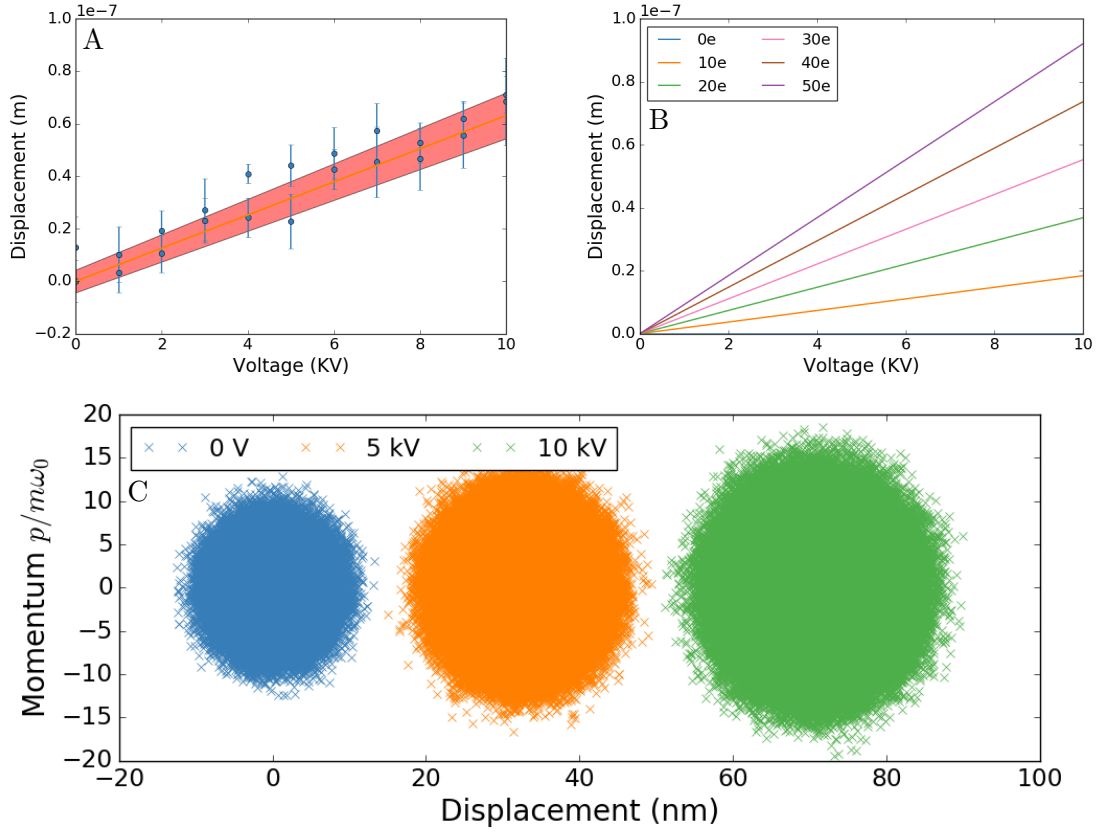


FIGURE 3.4: **A:** z displacement for a $\varnothing 82$ nm particle with a charge of 50 ± 20 elementary charges. The voltage was varied from 0 V to 10 kV and back down to 0 V. **B:** Theoretical displacement for a $\varnothing 82$ nm particle from a number of charges as the voltage is varied. Even for 100's of charges the displacement will be less than the trap size. **C:** Phase-space distribution for the same particle as in **A** for 0, 5 kV and 10 kV. It shows not only the relative shift in the trap centre but also the increase in T_{com} as the cooling efficiency drops.

3.2.2 Electrostatic field - Frequency shift

Under the DC field the particle oscillates around a new trap centre but now the trap is no longer symmetric. When the particle is closest to the needle the Coulomb force pulls the particle further from the centre and conversely, when the particle is on the other side of the trap to the needle it is pulled back towards the trap centre. This can be seen as a shift in the oscillation frequency, as shown by taking the full force equation for the center of mass motion,

$$\ddot{x}(t) + \Gamma_0 \dot{x}(t) + \frac{k}{m} x(t) + \frac{q_p V r_t}{d^2} = \frac{F_{th}(t)}{m}. \quad (3.33)$$

Let $x = d' - d$ where d' is the distance between the centre of the laser focus and needle tip and d is the distance from the needle to the particle. In the resulting quadratic equation

x^2 can safely be taken as small and the Taylor expansion can be used to linearise, so that the force becomes,

$$\begin{aligned}
 F(t) &\approx \frac{q_p V r_t}{d'^2 - 2d'x(t)} \\
 &\approx \frac{q_p V r_t}{d'} \frac{1}{d' - 2x(t)} \\
 &\approx \frac{q_p V r_t}{d'} \left(\frac{1}{d'} - \frac{2x(t)}{d'^2} + O(x^2(t)) \right). \tag{3.34}
 \end{aligned}$$

The first term is just a constant that isn't useful but the second term can be compared Hooke's law to give,

$$\begin{aligned}
 F(t) &= \frac{4q_p V r_t}{d'^3} x(t) \\
 &= k_{DC} x(t). \tag{3.35}
 \end{aligned}$$

Using this as the external force and taking the Fourier transform as normal shows that the normal spring constant has been modified,

$$-\omega^2 x(\omega) + i\omega\Gamma_0 x(\omega) + \frac{(k_0 + k_{DC})}{m} x(\omega) = \frac{F_{th}}{m}. \tag{3.36}$$

Let $\omega' = \sqrt{\omega_0^2 + k_{DC}/m}$ as in reality k_0 is difficult to obtain directly. The PSD is then,

$$S(\omega) = \frac{k_b T}{2m} \frac{\Gamma_0}{(\omega'^2 - \omega^2)^2 + \Gamma_0^2 \omega^2}. \tag{3.37}$$

To test this a $\phi 100$ nm particle was trapped and the pressure reduced to 8×10^{-5} mbar. The potential on the needle was raised from 0 to 10 kV in 1 kV steps but it was also reduced to 0 kV between each step. By doing this the drift in frequency due to thermal fluctuations in the alignment can be cancelled out. The voltage was then reversed and the same procedure performed down to -10 kV. The largest frequency shifts are shown in Fig.(3.5.A) with the positive potential giving a shift of 1500 Hz while the negative potential resulted in a maximum shift of 1100 Hz. That level of shift would result in a charge of 10^5 using Eq.(3.37). Not only does this charge not agree with the DC measurements (and later AC work) but would result in a force of 10^{-11} N that would rip the particle from the optical trap at only 10^{-13} N at 1 μm from the trap centre.

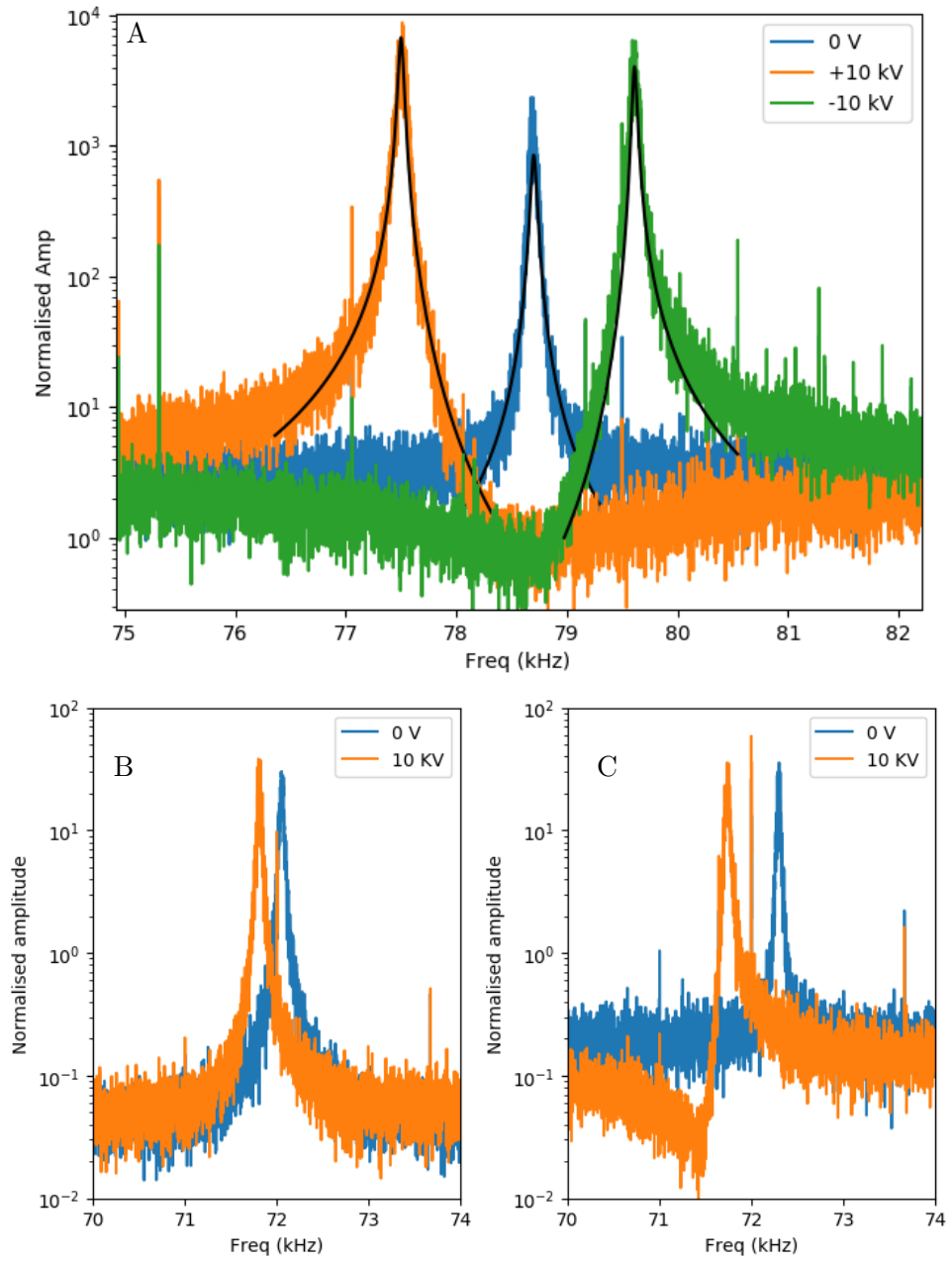


FIGURE 3.5: **A**: PSD of Z motion with 0, +10, -10 kV applied to the needle. A clear shift is seen in the centre frequency as well as a small skew affect. **B**: Z frequency peak for a un-charged particle. **C**: Z frequency peak for a charged particle. There is a frequency shift and a skew for the charged particle but the uncharged particle also shows a small frequency shift. The change in frequency in the uncharged case is on different time frames and is likely due to the alignment of the trap changing due to thermal drifts.

Even though this is unrealistic, Fig.(3.6.B) still shows the correct linear relationship between the frequency shift and the applied voltage for a number of particles. As the magnitude of the electric field is increased a small skewness of the frequency peak can be seen. The peak is no longer symmetric around the centre frequency and even goes

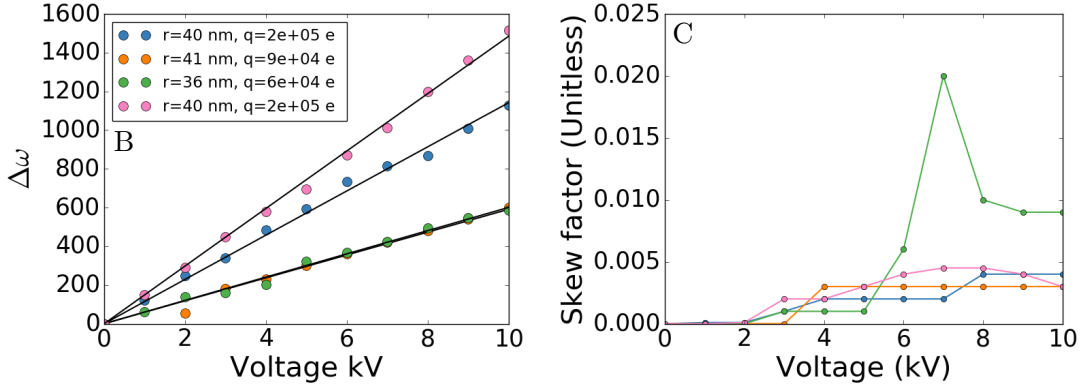


FIGURE 3.6: **A**: Frequency shift for a one of different particles showing the range in size and charge. The charges come from fitting Eq.(3.39) and are much larger than measured using DC and are also unrealistic as they would result in forces stronger than the trap. **B**: Skewness for the same particles. The skewness seems to increase with voltage but there doesn't seem to be any relation to charge. This is unexpected and further investigation is underway to find the physics of this effect.

below the noise floor at high voltages. This skewness can be included in to Eq.(3.37) by introducing the cumulative distribution function (CDF),

$$CDF(\omega) = \frac{1}{\pi} \tan^{-1} \left(\frac{\kappa(\omega_0^2 - \omega^2)}{\Gamma_0} \right) + \frac{1}{2}, \quad (3.38)$$

where κ is the skewness factor. In the general case a distribution is twice the product of the CDF and the probability distribution function. The PSD equation then becomes[56],

$$S(\omega) = \frac{k_b T}{2m} \frac{\Gamma_0}{(\omega'^2 - \omega^2)^2 + \Gamma_0^2 \omega^2} \times \left(\frac{2}{\pi} \tan^{-1} \left(\frac{\kappa(\omega_0^2 - \omega^2)}{\Gamma_0} \right) + 1 \right). \quad (3.39)$$

The skewness is seen to change linearly with voltage in Fig.(3.5.C) where κ has been used as a fitting parameter. It is unclear what effect charge has on the skewness as there is a lot of overlap between data sets. Intuitively, it would be expected that the skewness would increase linearly with charge as the force does, but here the effect seems independent for charge. It may just be that there isn't the resolution and data to see the relation with charge. The physical case of this skew on the distribution is also unclear and at the time of writing there were two leading ideas that also hope to explain why the measured charge value is so large.

- The particle has been pulled far enough from the trap centre to now be in a non-symmetrical trap. This would lead to an asymmetry in the trap stiffness and so the skewed frequency response.

- The other is Fano resonance where one state is scattering off another. Here the two states might be the shifted frequency and the natural frequency of the trap. More work is needed if this is the physics but much of the mathematics has been done[57].

So far only static electric fields have been used but as shown earlier the best sensitivity will be with a force that is modulated at the trap frequency. For the Coulumb force this can be achieved by using an AC electric field.

3.2.3 AC electric fields

If the force is AC then the trap centre doesn't move and $\langle z \rangle$ is zero as normal. However, now the particle is a driven harmonic oscillator with the maximum driving amplitude given by Eq.(3.30). The full equation of motion is then,

$$x''(t) + \Gamma_0 x'(t) + \omega_0^2 x(t) = \frac{F_{th}}{m} + \frac{F_{ac}}{m} e^{i\omega_{ac}t}, \quad (3.40)$$

where $F_{ac} = \frac{q_p V r_t}{d^2}$ and ω_{ac} is the ac driving frequency. The particle's motion now has an additional frequency at ω_{ac} . To focus on the relation of this frequency and the natural frequency let,

$$x(t) = x_0 e^{i\omega_{AC}t}, \quad (3.41)$$

so that Eq.(3.2.3) transforms into,

$$S_{AC}(\omega_{AC}) = \frac{1}{m^2} \frac{|F_{th}|^2 + |F_C|^2}{(\omega_{AC}^2 - \omega_0^2)^2 + \Gamma_0^2 \omega_{AC}^2}, \quad (3.42)$$

where $|F_{th}|^2 = k_B T 2m\Gamma_0/\pi$. This gives the peak height at exactly the driving frequency. When ω_{ac} is far from ω_0 then the signal is weak but as the two converge there is a strong signal enhancement allowing much smaller forces to be detected. Fig.(3.7) shows the frequency response as ω_{ac} is swept from 73-83 kHz in 0.5 kHz steps, as well as driving the particle on resonance. There is a clear increase in the driving signal as it approaches ω_0 .

Fig.(3.8) shows the peak heights change as a function of detuning from ω_0 . Fitting Eq.(3.42) gives a charge of $4 \pm 3e$, which is less than given by the DC field but is still

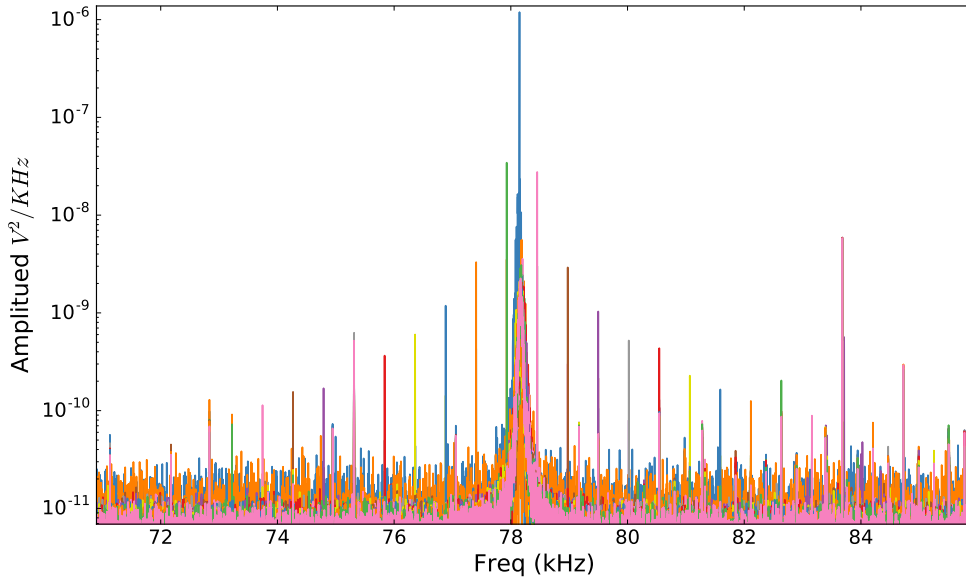


FIGURE 3.7: ω_{ac} is swept from 73 kHz to 83 kHz in steps of 500 Hz and also on resonance to show the full spectrum. The height of the driving peak increases the closer together ω_{ac} and ω_0 become. This increase is Lorentzian but there are also outliers where ω_{ac} matches other noise peaks.

a reasonable value. The AC force on the $\varnothing 100$ nm particle is $8 \pm 6 \times 10^{-20}$ N with an integration time of 10 seconds. The near resonance the signal-to-noise is 10:1 so the noise floor is at $8 \pm 6 \times 10^{-21}$ N which (with the integration time) gives a sensitivity of 10^{-20} N/ \sqrt{Hz} . Thermal limit of the sensitivity, as given by Eq.(3.1), is 3×10^{-20} N/ \sqrt{Hz} (assuming damping from air to be $2\pi * 10^{-2} Hz$) so this is the origin of the noise floor. It is a little higher than other work because the particle could not be retained at lower pressures, dropping if the pressure was below 10^{-5} mbar). On resonance the signal is 200 times larger than the undriven signal, which allows forces down to 4×10^{-22} N to be measured and gives a sensitivity of 4×10^{-21} N/ \sqrt{Hz} , achieving on-resonance zeptonewton sensitivity with just 1 second of integration. This is below the off resonance noise floor and clearly shows the enhancement effect. This method of detection could potentially measure yoctonewton forces with 2×10^4 seconds of integration. Due to this enhancement and because both ω_{ac} and ω_0 can be moved to areas in frequency space that have lower noise, this method of detection is strongly preferred. However, there is one force where it might not be practical to use.

3.3 Gravity

Gravity is the weakest of the four fundamental forces of nature and yet it is also the one people are most familiar with. It is responsible for the creation of planets[58], drives the nuclear fusion at the heart of stars[59] and even distorts space-time[60][61]. There has

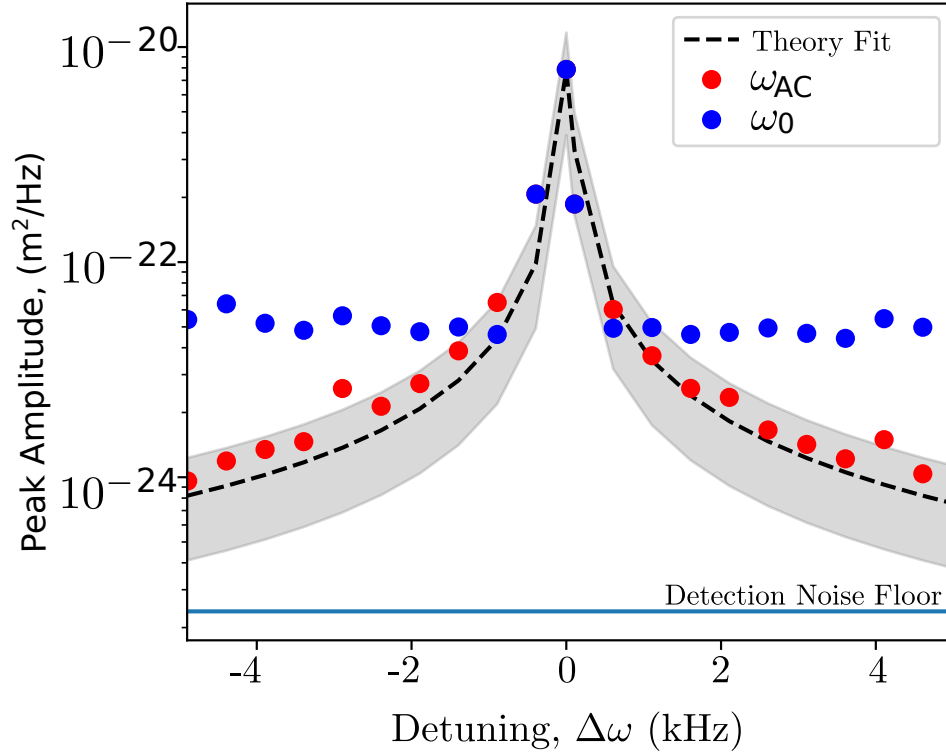


FIGURE 3.8: Fitting to the peak heights gives an AC force of $8 \pm 6 \times 10^{-20}$ N and a corresponding change of $4 \pm 3e$ at 1 V. On resonance there is an increase in signal to noise of 200:1 which gives an increased sensitivity of 4×10^{-21} N/ \sqrt{Hz} which is beyond the normal thermal limit of 3×10^{-20} N/ \sqrt{Hz} as given by Eq.(3.1).

been increased interest in gravity recently due to the discovery of gravitational waves[62] and their implications to astrophysics. LIGO has a strain sensitivity of 1×10^{-23} [63] which is a positional sensitivity of $\mathbf{SL} = 4 \times 10^{-20}$ m, where $L = 4 \times 10^3$ m, measured as a change in the relative length of the detection arms. Additionally, the gravitational wave event only lasts about 0.05 seconds, which means is far beyond the limits of the system presented here. However, there is still considerable disagreement as to the value of Newton's gravitational constant[64] and the measured value even seems to oscillate in a 5.9 year cycle[65]. Traditional methods to measure the gravitational constant involve the use of a torsion balance[66], but with an optomechanical system the particle's motion can be manipulated by simply moving a large enough mass very close to the experiment.

3.3.1 Gravitational Constant

The gravitational force between two objects of mass m_1 and m_2 is given by,

$$F_G = \frac{Gm_1m_2}{r^2}, \quad (3.43)$$

where r is the centre to centre separation and G is the Gravitational constant, $6.674 \times 10^{-11} \frac{Nm^2}{kg^2}$. The mass of the objects is taken to be $m = \frac{4}{3}\rho\pi r^3$, where $\rho = 2650 \text{ kg/m}^3$ for silica and $\rho = 11340 \text{ kg/m}^3$ for the lead test object. The separation between the centres must be greater than the sum of the masses radii, i.e. $r > r_1 + r_2$. Ideally this force would be time dependent in some predictable way so that the particle's motion is modulated at this frequency. It would be best if this modulating frequency was at the trap frequency as discussed earlier, see Fig.(3.8), but this may not be possible for large masses as the technology either doesn't exist or is very expensive. Thermal drifts are the largest source of noise and they operate in the Hz range so a target modulation frequency of at least 10 Hz is needed to avoid this. Both masses can be controlled independently along with the separation between them so there are a few different ways this experiment could work and each will be covered in detail before picking the most suitable.

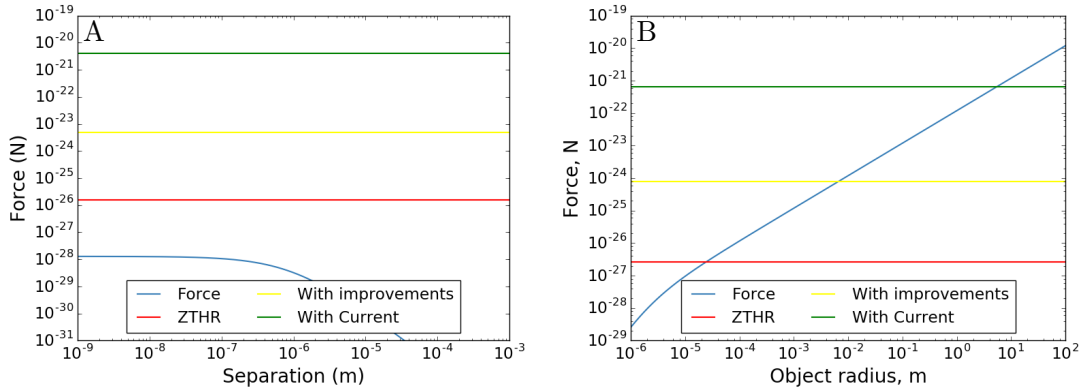


FIGURE 3.9: **A:** Force between two $\odot 1 \mu\text{m}$ particles and their separation. The green line: current force sensitivity, yellow line: expected sensitivity for $\odot 1 \mu\text{m}$ particles at 10^{-9} mbar and 4.2 K, red line is the ZTHR limit. Minimum forces are obtained using 3 hours of integration time but the force doesn't even come close to any of the limits. **B:** Force between a $\odot 300 \text{ nm}$ particle and a test mass. The radius of the test mass is increased while the separation between the two is kept constant at $1 \mu\text{m}$. At $Q = 10^9$ a the test mass would need a radius of 6.5 mm to produce a detectable force. The current system would require a test mass of 74 Tons.

The first method is to have particles of a fixed size and vary the distance between them. Fig.(3.9.A) shows Eq.(3.43) for two $1 \mu\text{m}$ particles as the separation is reduced. The change in gradient at $1 \mu\text{m}$ is due to the separation being dominated by the particle radius. Even without this gradient change though the system doesn't even come close to reaching the sensitivity requirements. It should be noted that the quantum limit assumes the ZTHR limit of $10^{-24} \text{ N}/\sqrt{Hz}$ can be reached with the given particles. For large particles this is unlikely given all the challenges presenting in the sensing section.

The force can be increased by just using a larger test mass but the increase is only linear so the mass may have to be quite large. This can be helped by keeping the separation

at the minimum of $1 \mu\text{m}$, which is the size of the laser focus. The current system would need a test mass of 74 Tons but Fig.(3.9.B) shows that with the improvements made a mass of just 13 g should be detectable. If the ZTHR is ever reached then the test object could be just $48 \mu\text{m}$ in diameter with a mass of $6 \times 10^{-10} \text{ kg}$. These are very promising numbers as they show the set up is able to measure the Newtonian constant with a relatively simple lab based experiment. However, the separation is very small and it would be preferable to have more space so that the test mass does not obscure the focusing mirror.

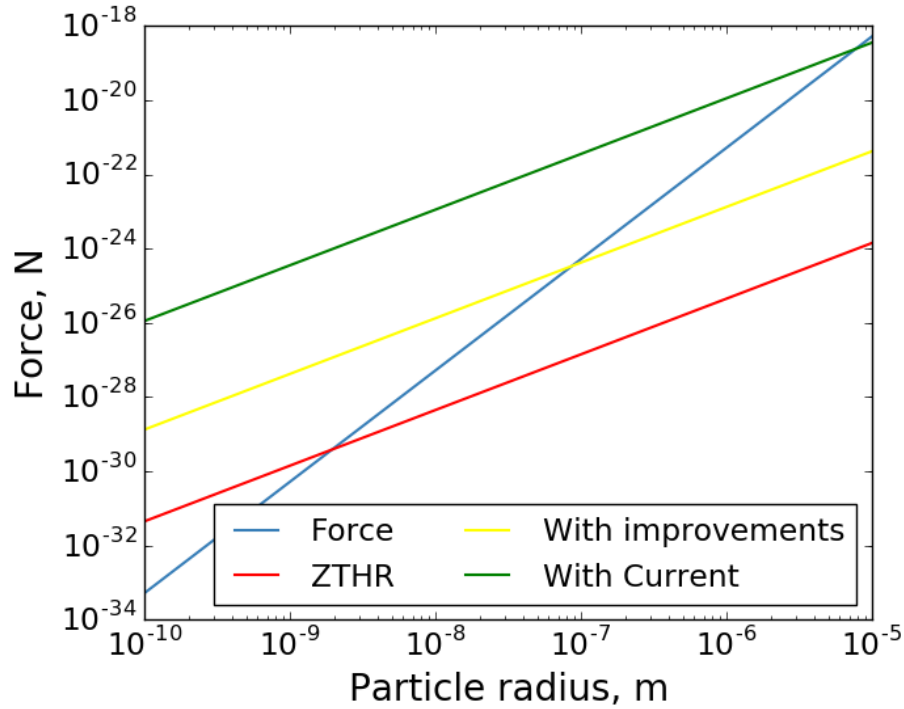


FIGURE 3.10: The test mass is fixed at 1 kg and the separation is set to 1 cm. The particle radius is then increased, which increases the force between the two objects. With the current setup the particle would have to have a radius of $7.8 \mu\text{m}$ which is not trappable. With improvements the particle's radius would only have to be 86 nm which is very realistic and at the ZTHR limit the particle can be as small as 1.9 nm .

The last idea is to have a nanoparticle and a 1 Kg mass a fixed distance apart. The nanoparticle's mass is then increased to see how large it would have to be for the gravitational force to be detectable. Again the separation is from edge to edge so that r in Eq.(3.43) becomes $r = r_t + r_p + d$, where r_t is the test mass radius, r_p is the particle radius and d is the separation distance. The integration time is taken as 3 hours, $\approx 10^4$ seconds, and the improvement line is with the chamber at 10^{-9} mbar and 4.2 K . With the current limit the particle would have to have a radius of $7.8 \mu\text{m}$. This is larger than the trap waist so wouldn't be possible with a gradient trap, although it might be possible with a scattering trap. With the cooled chamber though the particle would

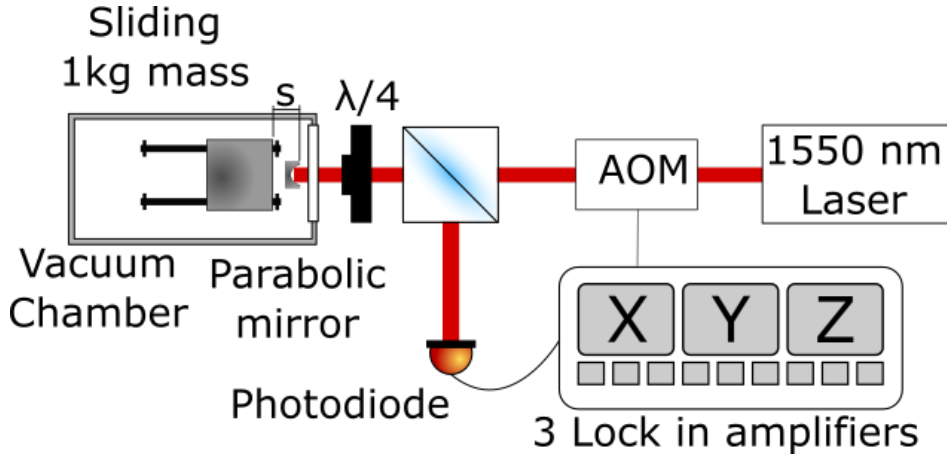


FIGURE 3.11: Schematic diagram of the proposed experiment to measure gravitational constant. The particle is trapped as normal but there is a mass behind the mirror that can move freely. The mass is then oscillated along the rails to generate a modulation on the trapping frequency. Extreme care must be taken to ensure the vibrations from the motion are not transferred to the particle resulting in a false positive.

only have to be 86 nm in radius, which is very achievable and at the ZTHR limit the diameter could be as small at 4 nm, which might even be too small to trap. A 1 kg mass should be small enough to move using piezo devices. The force can then be modulated by changing the separation distance with $\Delta r = 500 \mu m$ giving a 10% variation in the force. A simple setup is shown in Fig.(3.11) where the test mass has been placed in the vacuum chamber. This isn't required and with a separation distance of 1 cm the test mass could easily be outside of a small chamber and then its position varied with a piezo actuator. This would allow for a direct measurement of the gravitational constant, G , in a relatively simple lab based experiment. It would also be interesting to see if the gravitational force between the nanoparticle and the earth could be detected.

3.3.2 Change in local gravity

The gravitational force between any object and the earth, when the object is at sea level, is given by $F_g = mg$, where m is the test objects mass and $g = 9.81$. By Comparing to Eq.(3.43), the change in the gravitational acceleration on the particle is,

$$\Delta g = \frac{Gm_e}{(r_e + d)^2}, \quad (3.44)$$

where m_e is the mass of the earth (5.972×10^{24} kg), r_e is the mean radius of earth (6.371×10^6 m), G is the gravitational constant and d is the altitude above sea level. At sea level the force on a 100 nm diameter nanoparticle is 1.36×10^{-17} N and an altitude increase of 9 km (30,000 feet, cruising altitude a 747 aircraft) would see a change in

this force of 4×10^{-20} N. This should be detectable with the current setup and would also result in a shift in the vertical frequency (assumed to be y frequency) as with the DC electric fields. This would require the same particle to remain trapped the whole time or for enough repeated experiments to build a profile of the effect. The aim here is to produce a lab based experiment which takes advantage of the high sensitivity and integration times. With a $\varnothing 300$ nm particle at 10^{-9} mbar and 4.2 K it would be possible to detect the change in g for altitudes as low as 6.7 mm with 3 hours of integration. If the ZTHR limit can be reached then the minimum required altitude change is $23 \mu\text{m}$, which could be achieved with piezo actuators. An example setup is shown in Fig.(3.12) where the most important detail is that the light now enters/leaves the chamber via an optical fibre. This means that the chamber is detached from the rest of the setup and can be moved without disrupting detection optics. The cryo-chamber is too heavy to move 3 mm at anything other than sub-Hz frequencies, so it would be best if the mirror was instead mounted on a secondary cage that could then be oscillated in the chamber.

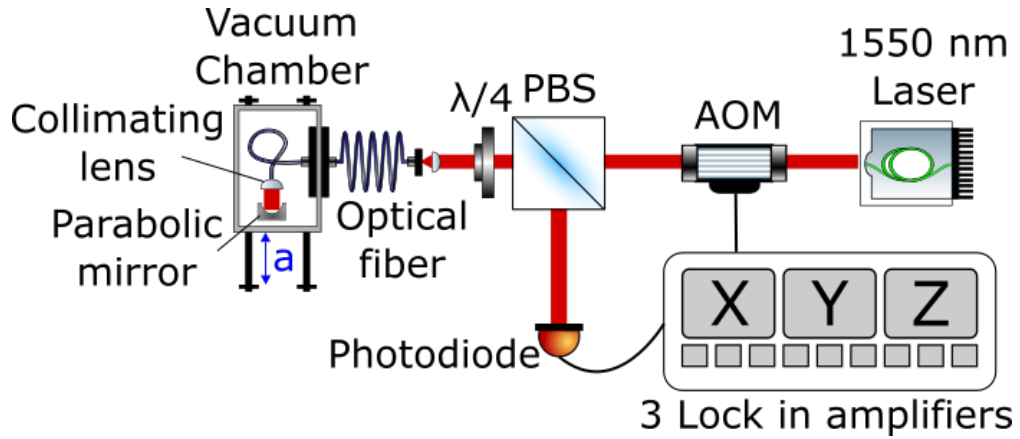


FIGURE 3.12: To detect a change in local gravity the laser light could be fed into the chamber which could then be oscillated. This would work best with a miniature chamber such as the DN16CF from Lesker[67].

3.4 Magnetic resonance force microscopy

The nucleus of an atom is composed of neutrons and protons bound together by the Strong force. Each nucleon has a spin $1/2$ which sum to give the overall spin of the nucleus, S . If the number of protons and neutrons is even then $S = 0$ as the protons/neutrons form opposite spin pairs to reach the lowest energy state. For example Carbon-12 has 6 protons which combine to give $S_p = 0$ and 6 neutrons that equally combine so that $S_n = 0$. The total nuclear spin of Carbon-12 is therefore $S = S_p + S_n = 0$. Silicon is 4.7% Silicon-29 (^{29}Si) which has an even number of protons but an odd number of neutrons at 15 so the total spin is a half-integer, in this case $S = 1/2$. In the

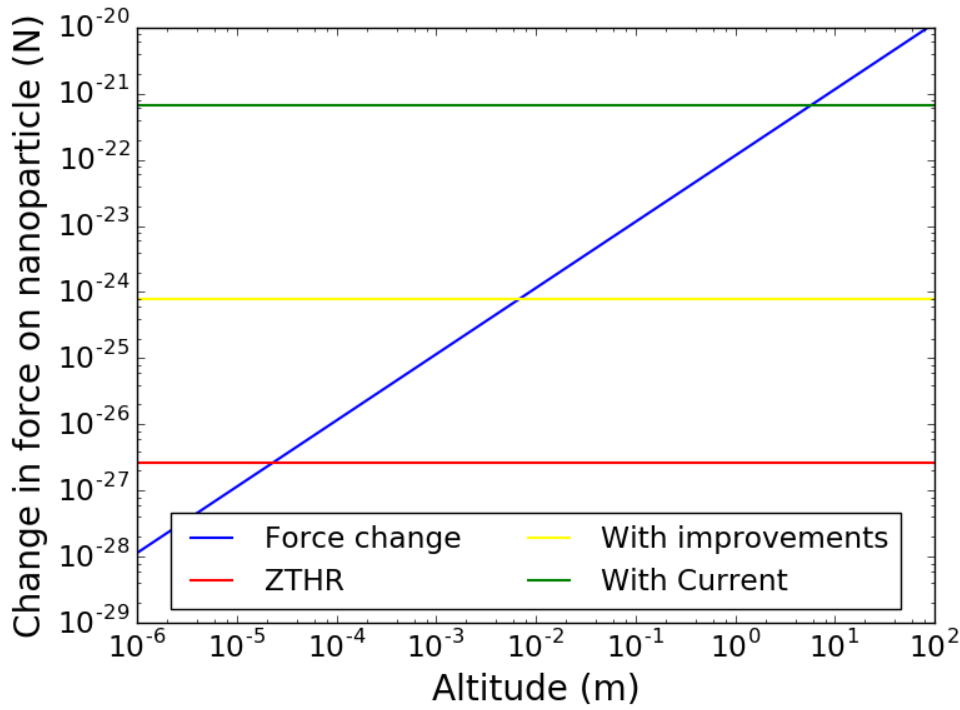


FIGURE 3.13: Change in the gravitational force on a $\varnothing 300$ nm particle for a given change in altitude. The current system would need a change of 5.6 m but at the SQL an altitude of just $23 \mu\text{m}$ should be detectable.

absence of a magnetic field these spins are orientated randomly. However in the presence of a magnetic field they will align either parallel or anti-parallel to the direction of the magnetic field, assuming $T = 0$. This can be represented as a magnetic dipole moment (μ) which can be thought of as the axis around which the spin rotates. This is shown in Fig.(3.14) where $|\uparrow\rangle$ is the low energy state, ϵ_1 , in which the magnetic moment is parallel with the magnetic field, and $|\downarrow\rangle$ is the high energy state, ϵ_2 , where the magnetic moment is anti-parallel to the magnetic field. This is the reverse of the case of electrons which would have $|\downarrow\rangle$ as the low energy state.

The classical way to describe this system is that when the magnetic moment is directed at some finite angle with respect to the magnetic field direction, the field will exert a torque on the magnetic moment. This causes it to precess round the magnetic field direction with an angular frequency known as the Larmor frequency. This Larmor frequency is analogous to the energy level splitting and is given by,

$$\begin{aligned}\omega_L &= \frac{\mu B}{\hbar} \\ &= \gamma B,\end{aligned}\tag{3.45}$$

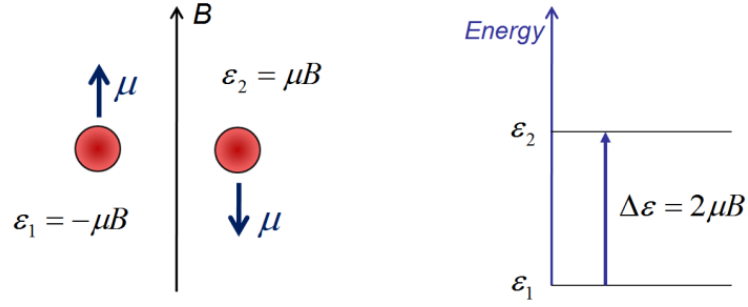


FIGURE 3.14: **A:** In the presence of a magnetic field and assuming $T = 0$, the magnetic moments align to the direction of the field with the arrow pointing from north to south. $|\uparrow\rangle$ is the low energy spin state and $|\downarrow\rangle$ is the high energy state. **B:** The energy separation between $|\uparrow\rangle$ and $|\downarrow\rangle$ is also the Larmor frequency. This energy separation increases linearly with magnetic field.

where γ is the gyromagnetic ratio which for ^{29}Si is $2\pi \times 8.4 \frac{\text{MHz}}{\text{T}}$. For a magnetic field of 0.3 T the Larmor frequency will be $2\pi \times 2.5 \text{ MHz}$ which is an energy difference between $|\uparrow\rangle$ and $|\downarrow\rangle$ of just $1.6 \times 10^{-27} \text{ J}$. The spin states will have a thermal distribution as given by the Boltzmann distribution,

$$n_j = \frac{N}{Z} e^{-\frac{\epsilon_j}{k_B T}}, \quad (3.46)$$

where n_j is the number of particles with energy ϵ_j , k_B is the Boltzmann constant, T is the internal thermal temperature, N is the total number of particles and Z is the partition function. For the two level spin system Z is given by,

$$\begin{aligned} Z &= \sum_j e^{-\frac{\epsilon_j}{k_B T}} \\ &= e^{-\frac{\epsilon_1}{k_B T}} + e^{-\frac{\epsilon_2}{k_B T}}. \end{aligned} \quad (3.47)$$

The populations of the two spin states from Eq.(3.46) are then,

$$n_1 = \frac{N}{1 + e^{-\frac{\Delta\epsilon}{k_B T}}}, \quad (3.48)$$

$$n_2 = \frac{N e^{-\frac{\Delta\epsilon}{k_B T}}}{1 + e^{-\frac{\Delta\epsilon}{k_B T}}}, \quad (3.49)$$

where $\Delta\epsilon = \epsilon_2 - \epsilon_1$. Assuming a 100 nm diameter SiO₂ particle, for a Larmor frequency of $2\pi \times 2.5$ MHz at 300 K $\Delta n = n_1 - n_2 = 0.1 < 1$. As the number of states must be integer it can be seen that $n_1 = n_2$ for long time scales. On short time scales there will be a noise source, known as spin noise, due to the populations fluctuating as $\sqrt{\Delta n}$. Some experiments are able to detect this noise[68] but it is unlikely that the nanoparticle will have enough available spins for that style of experiment to work. To drive the particle's motion a large spin imbalance is needed that can then be manipulated. This can be achieved by maximising the magnetic field and minimising the thermal temperature of the particle.

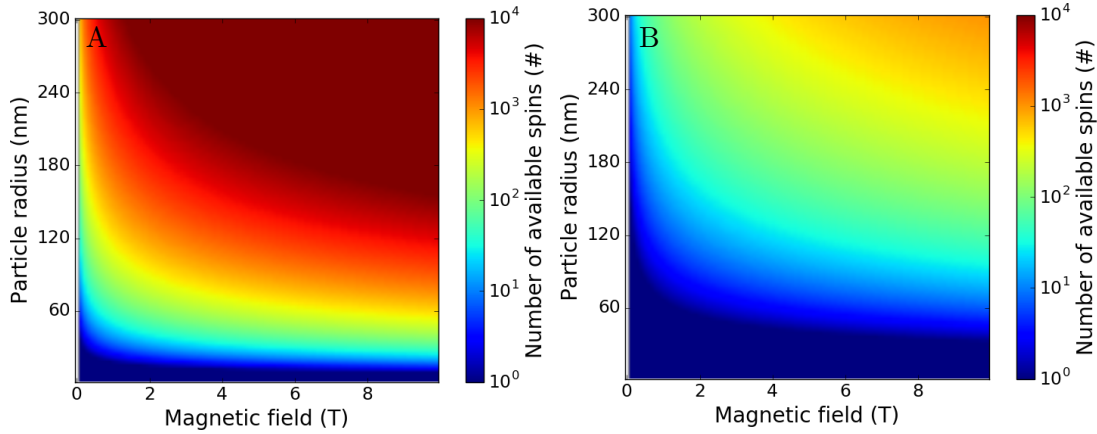


FIGURE 3.15: **A:** Heat map showing the number of available spins at 4.2 K by changing particle radius and the magnetic field strength. It is seen that it is difficult to get above $\Delta n = 10^4$ so the optimal parameters are taken to be $r = 150$ nm and $B = 5$ T, as a particle of that size have been trapped before and the magnet wouldn't have to be run at full strength for long periods of time. **B:** Similar heat map but at 300 K. Here there is a much more gradual increase in Δn but it is still possible to reach a useful number of spins. A magnetic field of 8 T and a particle radius of 300 nm would give 800 ± 30 spins to use.

Fields strengths of 10 T and temperatures of 4.2 K can be achieved with a cryogenically cooled superconducting magnet, which for a $\phi 100$ nm particle would give $\Delta n = 330 \pm 20$ available spins with the error from the spin noise. It should be noted that the abundance of Silicon-29 is assumed to be 4.7%, the natural abundance, but there are enriched nanoparticles that have a much higher concentration[69]. This can be improved by using a larger particle as seen in Fig.(3.15.A) for $T=4.2$ K and Fig.(3.15.B) for room temperature. Due to the exponential term it becomes increasingly difficult to obtain more spins above $\Delta n = 10^4$. A balance is therefore proposed where a particle with a radius of 150 nm is used with a 5 T magnetic field. This would give 4500 ± 70 spins but with a particle radius that has been trapped before. It would also allow the magnet to be run at a level that could be maintained for long integration times. The magnet is cooled by a multi-stage process involving the use of both liquid nitrogen and helium to cool copper heat transfer pipes. However, cooling the particle's internal temperature is

difficult as there is no physical contact and the very low pressures reduce the effectiveness of convection. It is also likely that the laser is depositing sufficient energy to heat the particle even if the chamber is immersed in helium. The 300 K example in Fig.(3.15.B) shows that while it is challenging, it is still possible to generate a usable number of spins at 300 K. A $\varnothing 300$ nm particle in an 8 T magnetic field at 300 K will have $\Delta n = 100 \pm 10$. The energy of the magnetic moments in a magnetic field is given by $U = -\mu \cdot B = -\hbar\gamma B$ and so the force acting on the particle is given by $\frac{\partial U}{\partial x}$ where x is taken to be the axis μ is aligned to.

$$F_{dipole} = -\Delta n \hbar \gamma \nabla B. \quad (3.50)$$

This force is plotted in Fig.(3.16) for a single spin, the 300 K example (100 spins) and the $\Delta n = 4500$ spin example as a function of the magnetic field gradient. The current experiment should be able to detect single spins with a gradient of 2.4×10^4 T/m and the improved setup should be able 30 T/m. The 300 K example (which is the most relevant to the current setup) should be detectable using a gradient of 250 T/m. The latter would require two 0.3 T magnets to be 12 mm apart. This gives a spin sensitivity of $27\mu_B/\sqrt{Hz}$ which reduces to $0.026\mu_B/\sqrt{Hz}$ for the improved setup. Of course the chamber may already be at 4.2 K given the cryogenically cooled magnetic so it is only the pressure of 10^{-9} mbar that would need to be achieved. If the ground state (ZTHR) limit can be reached then the spin sensitivity would be an impressive $0.00012\mu_B/\sqrt{Hz}$ beating many other groups[70].

If a particle is moving perpendicular to this gradient then there will be a deflection, as seen in the Stern-Gerlach experiment[71]. If the force is not modulated then there would be a frequency shift as seen with the DC coulomb force as both forces are due to anti-symmetric time invariant potentials. From the AC coulomb force it was learnt that the system is much more sensitive if the force is modulated at the trap frequency. If it is therefore possible to flip the spins so that they are always driving the particle's motion away from the trap centre, there should be a similar increase in the signal-to-noise ratio. This type of experiment is some times called a "folded Stern-Gerlach" experiment[72].

To manipulate the available spins a radio frequency pulse at the Larmor frequency is applied via a wire loop. A pulse duration of $\Delta t = 8\pi/\gamma B$ will change $|\uparrow\rangle$ into a symmetric state, i.e.

$$P_{\pi/2} |\uparrow\rangle = \frac{1}{\sqrt{2}}(|\uparrow\rangle + |\downarrow\rangle), \quad (3.51)$$

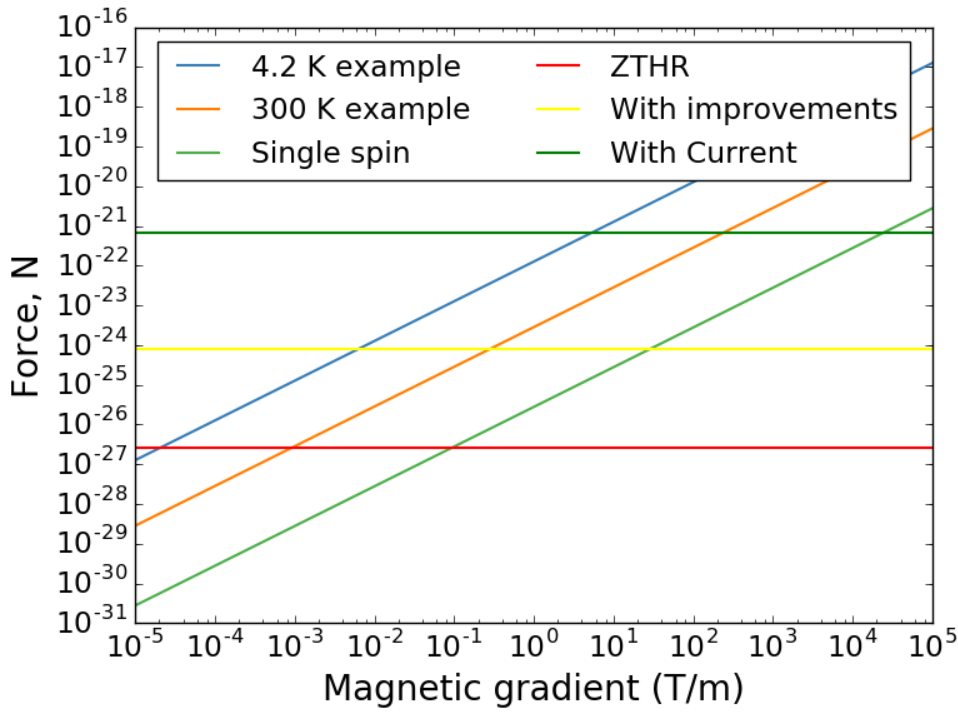


FIGURE 3.16: The expected force on the particle for a few difference parameters against the gradient of the magnetic field. To be detectable the force line must be above a the limit line for that setup as described in Sec.(3.1) where an integration time of 3 hours has been used. Even the current set up would be able to detect a single spin (using $B = 1.1 \times 10^{-3}$ T) with a gradient of 2.4×10^4 T/m. A single spin could also be detected with a gradient of 60 T/m using the improved setup.

where $P_{\pi/2}$ is the operator of the pulse. This is known as a $\pi/2$ pulse as it rotates the phase by 90° on the Bloch sphere. A pulse of twice this is a π pulse and reverses the state of a spin, i.e. $|\uparrow\rangle$ to $|\downarrow\rangle$ and $|\downarrow\rangle$ to $|\uparrow\rangle$. Once a pulse has been applied the spins will begin to re-thermalise and return to the original Boltzmann distribution. There are two main mechanisms that causes this to happen. The first is spin-lattice (longitudinal relaxation) where the spins gain or lose energy to the atomic lattice and is characterised by the time t_1 . The second is the spin-spin (transverse relaxation) mechanism where energy is transferred directly between neighbouring spins and is given by t_2 . In almost all cases $t_1 \gg t_2$ and so the free induction decay (t^*), the real measured decay time, will be closer to t_2 . For Silicon-29, $t_2 = 15 \pm 5$ msec[74] so t^* will be this as a minimum. This is more than $2\pi/\omega_0$ so the non-thermal state should stay for at least 1 trap cycle. The particle can therefore be driven with a π pulse at $2\omega_0$ such that the spin is always interacting with the gradient magnetic field to drive the particle away from the trap centre. Fig.(3.17.A) shows this diagrammatically.

Another scheme is shown in Fig.(3.17.B) and is based on work by Tao et al[73]. By taking advantage of the high gradient electromagnets found in modern hard drives they

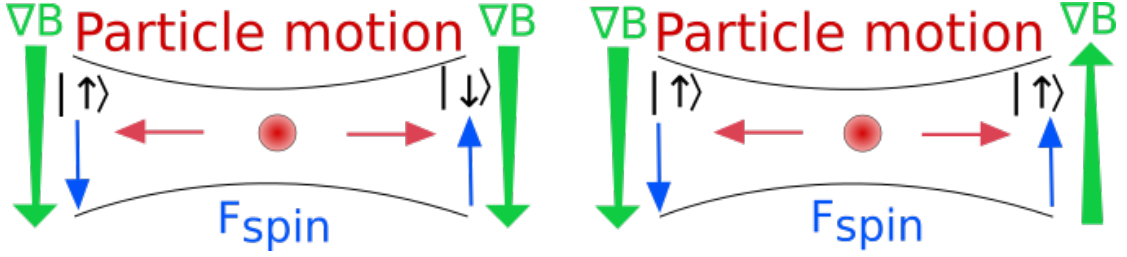


FIGURE 3.17: **A:** RF setup. A magnetic gradient is applied from top to bottom the same as in the Stern-Gerlach experiment. The particle oscillates in the laser focus and an RF π pulse is used to flip the spins at the extremes of the particle's motion. The interaction between the spins and the gradient field drives the particle's motion in the direction of the gradient. **B:** By using a setup similar to that of Tao et al[73] the need for an RF pulse can be removed. The magnetic gradient now comes from the centre of the trap motion by using the nano-scale electromagnet found in hard drives. The electromagnet can be driven by an AC signal at twice the trap frequency similar to how the PPL is used for cooling but 180° out of phase, so that it is the gradient that changes direction not the sides. These electromagnets are able to generate 2.8×10^7 T/m and would result in a much larger force for a given number of spins.

managed to reach a spin sensitivity of $0.032\mu_B \text{ Hz}^{-1/2}$. Not only does a hard drive have a high magnetic gradient of 2.8×10^7 T/m but it is also possible to modulate the magnetic field at high frequencies. The electromagnets would be placed close to the trap centre and the gradient could be modulated at twice ω_0 just as with the PPL cooling. The spins do not need to be controlled via RF pulses as the gradient field itself would be changed instead. If this system could be implemented then even the room temperature set up would have single spin sensitivity. This is shown in Fig.(3.18) where Eq.(3.42) has been used but with the spin force replacing the AC electric field. The noise floor is taken to be Eq.(3.1) at the given temperature with the pressure taken to be 10^{-5} mbar as this is readily achievable. The 100 spin ($T = 300$ K, $B = 8$ T, $r = 150 \times 10^{-9}$ m) example beats the 300 K noise floor at 10^4 T/m as predicted by the force equations. The 4500 spin example ($T = 4.2$ K, $B = 5$ T, $r = 150 \times 10^{-9}$ m) also agrees with the forces graph showing a signal to noise of 2:1 with the 4.2 K noise floor at 60 T/m. For the single spin ($B = 1.1 \times 10^{-3}$ T) a gradient force of 2.5×10^5 T/m is needed to beat the 4.2 K noise floor and 9.2×10^5 T/m to beat the 300 K noise floor, although the magnetic field would have to be 0.08 T to have a single spin at this temperature.

3.5 Conclusion

This chapter has shown an on resonance sensitivity of $4 \times 10^{-21} \text{ N}/\sqrt{\text{Hz}}$ and that with modifications the system should have a sensitivity of $\approx 10^{-24} \text{ N}/\sqrt{\text{Hz}}$ at ground state. The current limitations of the system are the amplifier noise on the detector and the frequency tracking of the PPL. The amplifier noise is thermal in origin so this

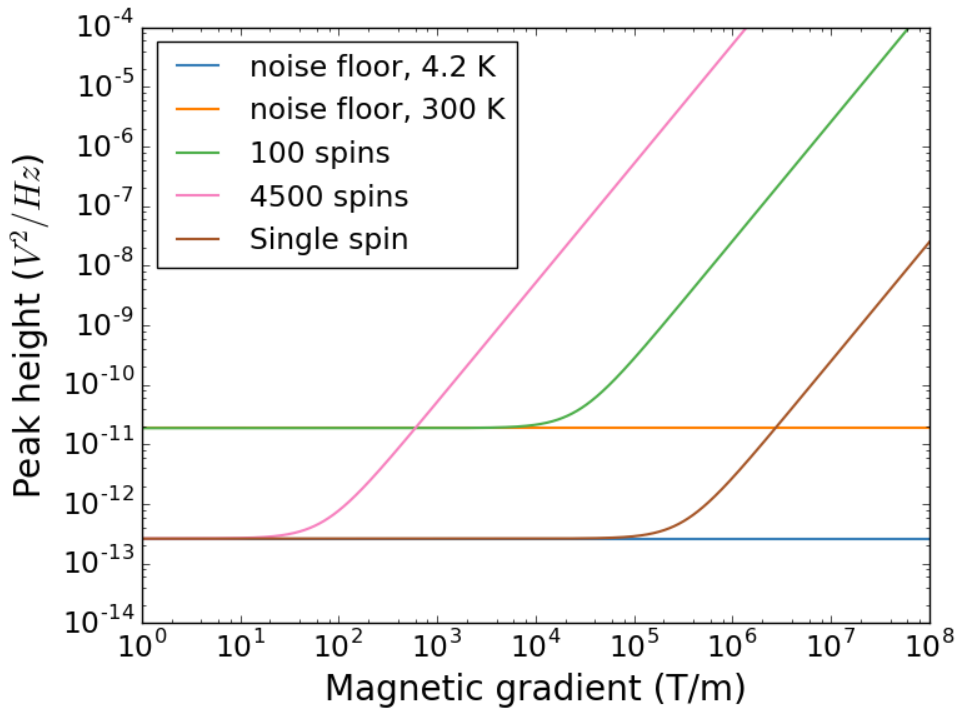


FIGURE 3.18: Expected increase in peak height against the gradient of the magnetic field. This is based on the mathematics used in the AC coulomb field but using Eq.(3.50) as the driving force. The driving is assumed to be on resonance to maximise signal-to-noise. The noise floors are taken to be Eq.(3.1) at the relevant temperature and the conversation factor (γ) is taken at 10^5 V/m so that at 300 K the noise floor agrees with measurement. The required magnetic gradients for beating the respective noise floors are in agreement with that shown in Fig.(3.16)

could be improved by implementing cooling around the detector. The PPL is harder to correct as it is a blackbox device, so the current research direction is to shift to using a field-programmable gate array (FPGA). An FPGA allows for complete control of the internal electronics so the integration time, filters, and phase/frequency tracking can all be balanced to maximise cooling. Using an FPGA would also allow other techniques to be tried such as Kalmann filtering and pulsed laser control. Kalmann filtering could increase the measurement precision of the phase and frequency while pulsed control would squeeze the position distribution and increase sensitivity on small time scales. For DC forces the slow time scale variation in the detection system due to thermal drift becomes the limiting factor. As such the smallest DC force detected was $\approx 10^{-16}$ N. One issue that did occur is damage to the needle. Through this work the needle is quoted as having a tip radius of $100 \mu\text{m}$. While this was true at the point of manufacture, minor damage to the tip occurred during the course of these experiments as shown in Fig.(3.19). This will have affected the electric field near the surface although far from the tip the needle is still point like. The exact effect this would have on the needles charge is unclear and may require finite element modelling.

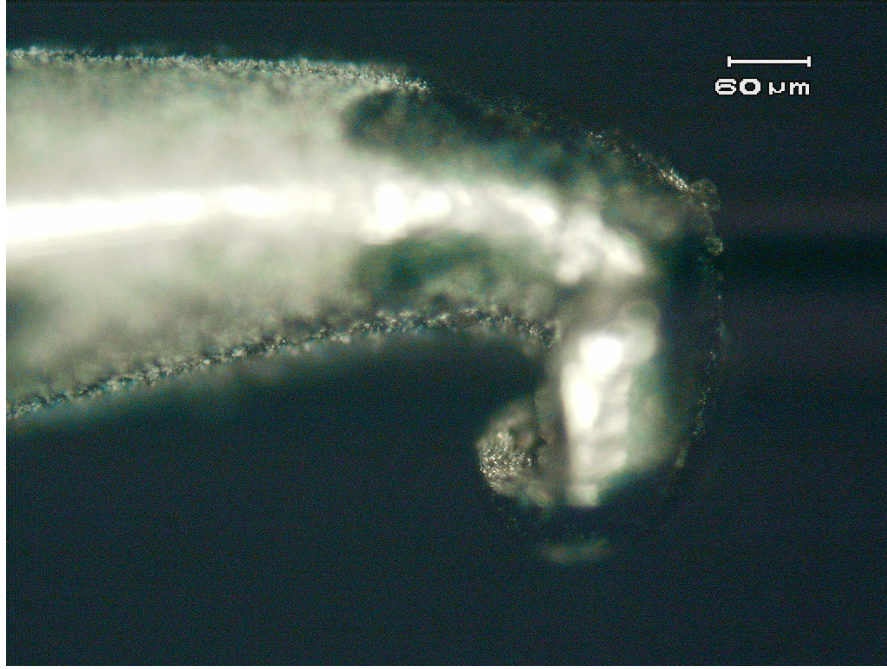


FIGURE 3.19: When manufactured the needle had a tip radius of $\approx 100 \mu\text{m}$ but during use the tip was damaged due to impact with other surfaces. It would change the electric field distribution and may have reduced the charge at the tip. This effect would need to be modelled using finite element analysis.

The remainder of this chapter discussed other forces and how they might be detected with this system or what changes would need to be made for those forces to be detectable. The most practical method to detect the gravitational force between the particle and a test mass is to use a 1 kg test mass that is 1 cm away from a $\varnothing 174 \text{ nm}$ particle. The test mass should be oscillated so that the motion of the nanoparticle is modulated at that frequency. Ideally this modulation would be at the trap frequency but that may not be possible given the challenges of moving such a large mass at high frequencies however some oscillation should be possible using a piezo actuator. A movement of just $500 \mu\text{m}$ would modulate the force by 10% which should be detectable. This would result in a force of 10^{-25} N which would require an integration time of 3000 years with the current sensitivity. For the improved setup the force should be detectable with the normal 3 hours of integration.

There are similar difficulties with measuring the change in the force between the nanoparticle and the earth, g , as the current setup would require an altitude change of 5.4 m with 3 hours of integration. With the improved set up the altitude change would only need to be 6.7 mm and at the ZTHR limit it could be as small as $23 \mu\text{m}$. The main challenge then will be moving the experiment in such a way that the vibrations of the chamber or small changes in alignment don't couple to the motion of the particle. For the alignment a fibre feed-through could be used and the vibrations require the mirror mount to be isolated.

The final ideal explored is magnetic resonance force microscopy. A spin moving through a gradient magnetic field feels a force in the direction of the field that is dependent on the alignment of the spin to the field. Sec.(3.4) gives more details but the summary is that a single spin can be detected if a magnetic gradient of $2.6 \times 10^4 T/m$ can be produced. This might be possible using the same method as used by Tao et al. where they were able to attach a hard drive arm to their experiment and produce gradients of $2.8 \times 10^7 T/m$. Even without this though the use of a cryogenically cooled superconducting magnet allows for a spin difference of 4500 ± 70 , which the improved setup could detect with a gradient magnetic field of 6 mT/m.

Detecting many of these forces requires high Q and so a pressure of 10^{-9} mbar which is in the UHV (Ultra high vacuum) range. This can be difficult and it is time consuming if the chamber has to be returned to atmosphere every time a new particle is needed. Also the current method of particle delivery involves using a water mix that leaves residue inside the chamber, requiring frequent cleaning and bake-outs to remove. It would therefore be preferable to have a vacuum compatible particle source and experiments towards this will be discussed in the rest of this thesis.

Chapter 4

Ablation

4.1 Overview of particle loading

One idea for a vacuum source is to produce the particle inside the chamber on demand. Nanoparticles are normally manufactured by a complex and well studied process first developed by Stber et al.[75]. This process allows for precise size control[76] but requires the use of solutions and so isn't usable at UHV. Another method involves a gas flow passing through a laser focus to cause the molecules to cohere into a solid particle before collection[77]. While it maybe be possible to manufacture particles in this way inside the vacuum chamber, it would be impractical for the experiment as the introduction of a gas would require a pump down phase in between each generation cycle.

Another idea could be to use two chambers, one at UHV and one at a partial vacuum. Particles would then be trapped or generated in the higher pressure chamber then passed via a travelling wave trapping through a hollow core fibre to the UHV chamber[78]. Interestingly, along with the obvious difficulties with such a system (such as the particles becoming clogged in the fibre and the alignment of a travelling wave though differing mediums) there is a more subtle complication. There is still a significant pressure gradient at the end of the fibre at UHV and it is difficult to push the particle through such a gradient. Even if it can be achieved, it is highly likely that the particle will be dropped during transfer.

For this work two other methods were explored: Laser ablation and Sonication. Laser ablation involves focusing a laser onto a silicon substrate and using the high energy density to generate nanoparticles inside the chamber directly. The sonication method involves using a peizo to shake prepared nanoparticles off of a surface[79]. This chapter will cover the work on the ablation method and Chap.(5) will cover the sonication work.

4.2 Ejection Mechanisms

The ablation of silicon results in the formation of nanoparticles over a range of sizes and via a number of different ejection methods. The dominance of each ejection method depends on a number of different parameters: pulse length, repetition rate, intensity, and the pressure. The exact relations are still a topic of study but for Silicon at least, some conclusions can be drawn based on the available evidence. To produce small particles the penetration depth, the point where the pulse energy has dropped by $1/e^2$, needs to be small. A large penetration depth will increase the amount of available material to be removed, this in turn increases average particle size. The intensity also determines the amount of material that is energised sufficiently to be released from the substrate as it is related to the energy density within the material. Together the intensity and pulse length determine the manner in which the material is released from the surface.

There are a few ejection processes and in general they all happen over the course of any single ablation cycle. However, the dominance of each effect can be adjusted by varying the characteristics of the laser system as shown in Fig.(4.1). This summary is based primarily on work done by Pantisar et al.[80], Perriere et al.[81] and Liu et al.[82]

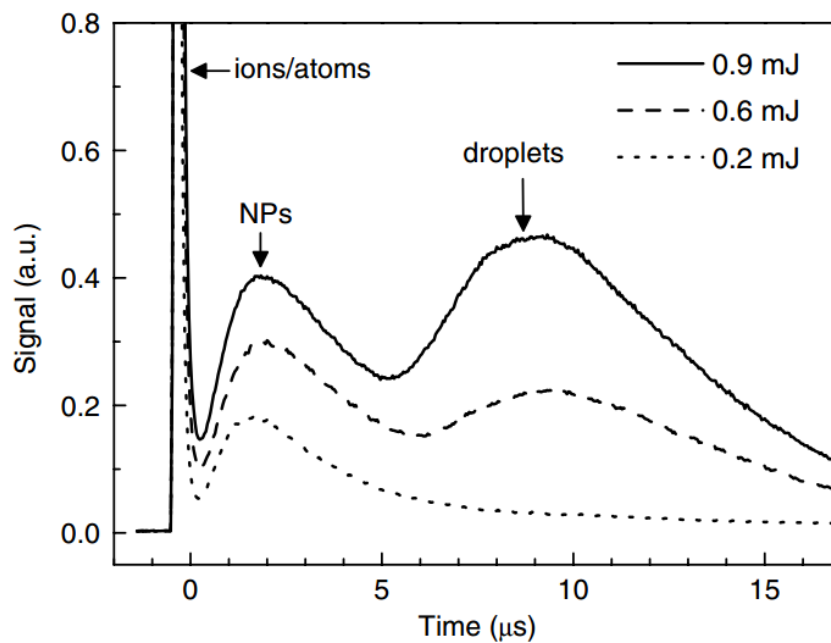


FIGURE 4.1: Particle formation mechanisms for different pulse energies as shown by Perriere et al[81]. The spot size is constant and the substrate is magnisiumoixde. Droplet formation is seen to dominate above a given energy.

Coulomb Explosion. The initial ejection from the surface after the impact of the laser pulse will be ions and electrons due to an effect known as Coulomb Explosion[83]. This happens as the high energy of the laser pulse strips the valence electrons leaving a close

packed plasma. The repulsive Coulomb force then forces the ions to leave the surface in a tight jet around 10 ns after the initial absorption of the pulse. These ions can later form nanoparticles by coalescing with together after a few microseconds of flight time if they haven't dispersed too far from one another[84]. This process is most significant with a femto-second laser and is dominant at lower powers.

Thermal Expansion. After 50 ns the laser pulse has been completely absorbed into the area of the material at the focus. This causes the material to heat up significantly compared to the surrounding material. As such it tries to expand but it is restrained by the edge material, resulting in a build up of pressure. Once this pressure reaches a critical value the surface tension is broken and the material expands rapidly expelling particles with diameters in the 1 μm to 100 nm range. This ejection also causes shock waves to travel into the material which are reflected at the hot-cool interface and then back into the expanding region. The material released from this is much larger and more solid in composition. These large chunks do not travel far and can normally be seen as a ring around the ablation region, known as reform. In most cases thermal expansion will account for the majority of the mass released from the substrate, but it is even more apparent in the nano-second pulse length range with high intensity.

Plasma ablation. If the repetition rate of the laser is high, 10kHz range, then the full ablation cycle will not be complete before the next pulse hits. If this is continued over multiple cycles it can lead to the formation of a plasma layer on the substrate surface that is constantly falling into the material below it. This results in the rapid remove of material before it has sufficient time to under go thermal expansion. It is for this reason that this technique is preferred by machinists that use laser ablation to drill into materials, as it creates clean edges and minimises debris and reform. An example of the difference between a high-repetition femtosecond (800 nm) and UV (255 nm) nanosecond pulsed laser is given in Fig.(4.2) where there is considerable reform at the edges.

4.3 Laser and power control

The laser (Surelite from Continuum) used for this experiment is a high power nanosecond Neodymium-doped Yttrium aluminium garnet (this thesis it will be referred to as just YAG) 1064 nm laser. This laser is firmly in the droplet production range via thermal expansion which is not ideal for the particle size range required for the optical trap, but it should be useful for a proof of concept. The intensity will have to be controlled to adjust the distribution of particle sizes, either by changing the focus or the laser output power. Due to the high power of this laser a remote control system was created using a Python script as an interface. This allowed the safe operation of the

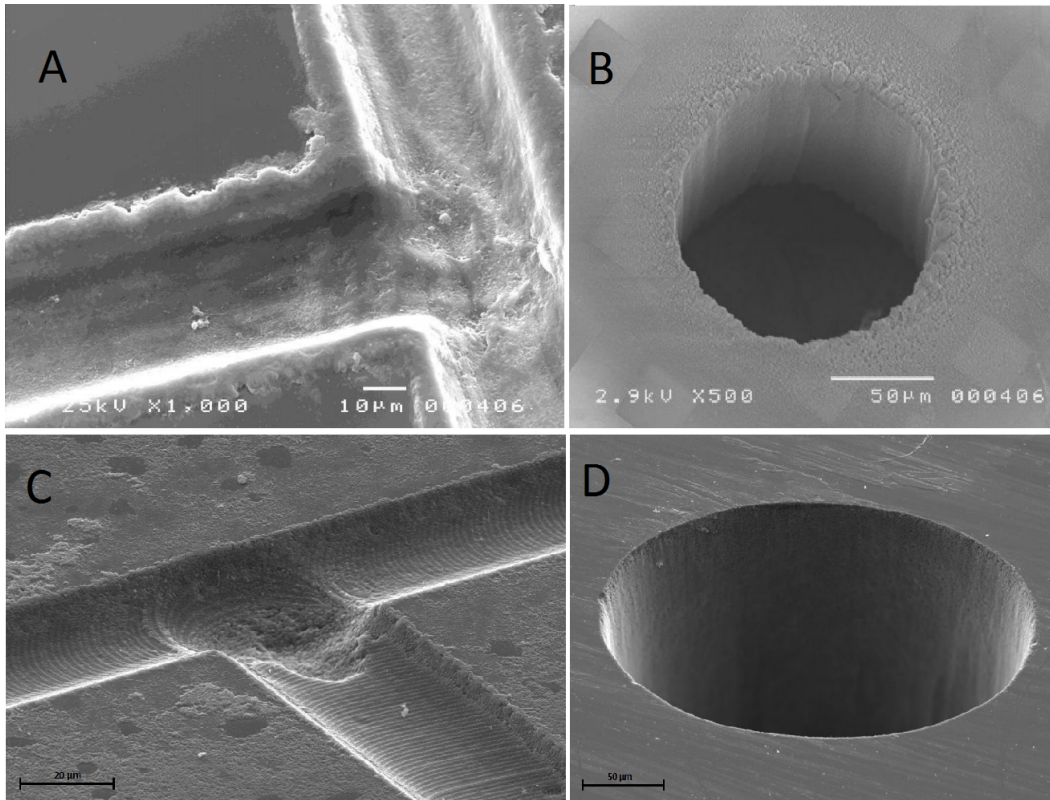


FIGURE 4.2: Comparison of holes drilled into glass from a ns pulse laser (a) and a fs pulse laser (b). The hole from the fs laser has much sharper edges and is much more circular due to the optimisation of the ejection of material via a plasma layer.[85]

YAG at high powers by allowing the operator to be safely out of the room. Locks and signage was used to prevent others from entering when the laser was active.

To control the power from the YAG a series of polarising beam splitters (PBS) and half wave plates (HWP) were placed in the beam path. Fig.(4.3.A) shows the reflected power after the first PBS as a function of angle of the HWP. High power optics must be used for this stage to prevent damage to the components and the PBS used is designed specifically for YAG lasers. The measurements were taken with the thermal detector but readings had to be stopped at 1 W (100 mJ) as even the unfocused laser began to damage the detector head.

Maximum laser output was therefore estimated to be 5.7 W with a pulse energy at 10 Hz of 570 mJ. The lowest recorded power was 79 mW at 228 degrees; this gives a pulse energy of 7.9 mJ which is still enough to damage a glass slide at the focus. To increase control and reduce the power further a second PBS designed to work at 1550 nm and a pairing HWP were used. With the first PBS taking most of the power, a second, low power PBS can be used in a second power control stage. The mis-match in design wavelength and laser wavelength in the second stage does result in a loss in efficiency of the PBS but it is still usable. Fig.(4.3.B) shows the reflected power against angle after

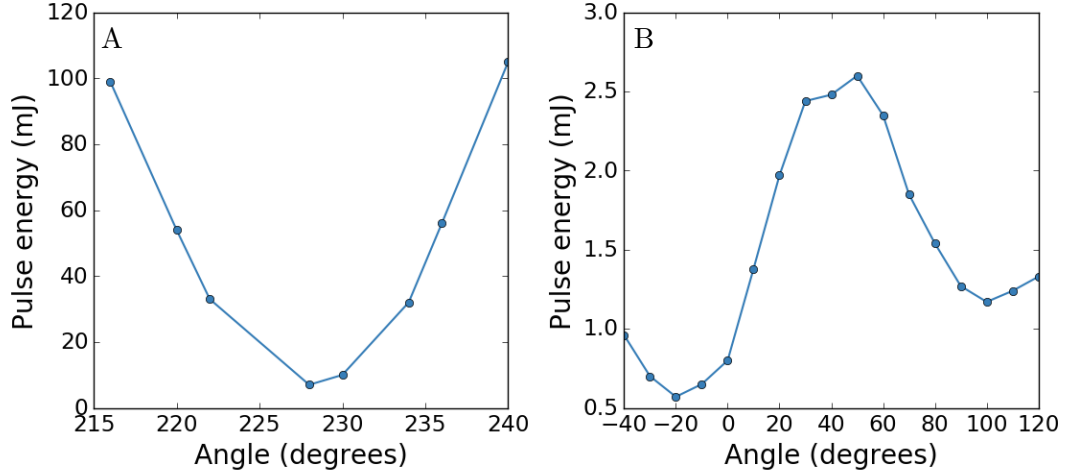


FIGURE 4.3: Pulse energy control using a pair of two polarising beam splitters (PBS). **A:** The course power control with a single PBS with an anti-reflection coating at 1064 nm. The laser can deliver up to 570 mJ but higher than 100 mJ would damage the detector. **B:** To get fine control of the laser power a second PBS was used after the first. This PBS was designed to work at 1550 nm, however it still functions well enough at 1064 nm to provide the control desired. Using this combination of PBSs it is possible to vary the power for 100 mJ to 0.6 mJ with an accuracy of 0.1 mJ.

the second stage. This allowed the pulse power to be reduced to 0.6 mJ with an accuracy of 0.1 mJ while the first PBS was set to 8.4 mJ. This energy density can therefore be controlled by using a combination of power control and by varying the focusing lens to maximise particle generation.

4.4 Particle generation

To test particle generation a chip was obtained from Paul Clark which had 200 nm of Silica on top of 525 μm of Silicon. Initial tests were done out of the chamber with an external setup to prevent damage to the trapping setup. It quickly became apparent that the laser was able to remove material from the surface once focused. The starting beam had a waist of 8 mm so that by using a lens with a 50 mm focal length the beam waist at the focus should be 2 μm using Eq.(2.9). The laser was set to a pulse energy of 20 mJ giving an intensity of $15 \text{ GW}/\text{m}^2$ which was focused on the Silica side. Fig.(4.4) shows the resulting hole bored through the chip, measuring $\approx 60 \mu\text{m}$ across and taking 16 minutes to cut. This results in the removal of 1.28 μg of Silicon at a rate of 80 ng/s . Theoretically, this could result in the production of 10^6 100 nm particles, however there will be a thermal size distribution so the exact number of useful particles is unknown.

Debris can be seen around the bore area and it was possible to trap some of the particles released during another run at atmosphere. It was not possible, however, to obtain an

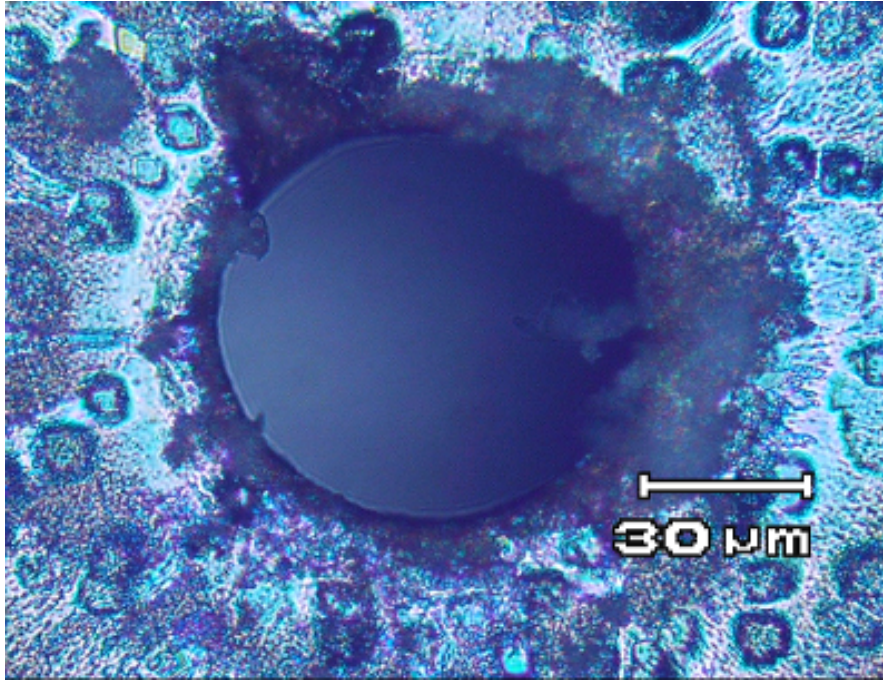


FIGURE 4.4: Hole cut through $525\ \mu\text{m}$ of Silicon using $200\ \text{mW}$ ($20\ \text{mJ}$) of power focused with a $50\ \text{mm}$ lens to give an intensity of $15\ \text{GW}/\text{m}^2$. Although the laser was aligned perpendicular to the surface the hole is not circular due to material weakness and because laser is not perfectly gaussian

accurate measurement for the size of the particles other than to say they must be in the $50\ \text{nm}$ to $500\ \text{nm}$ range as the trap does not function outside of this range. It can also be assumed that the particles are to the larger end of this scale, as the amount of scattered light was greater than that from the $100\ \text{nm}$ particles trapped previously.

4.4.1 Using 532 nm

Particle production is linked to the heating of the volume; the faster and greater the heating, the greater the number of particles produced. Silicon does absorb at $1064\ \text{nm}$ but it has a much stronger absorption in the visible as seen in Fig.(4.5)[86]. This would lead to a reduced penetration depth and so a greater number of useful particles. To this end the YAG laser was switched to its second harmonic of $532\ \text{nm}$ through the use of a lithium triborate frequency doubling crystal. The crystal is aligned to maximise the $532\ \text{nm}$ signal while the first PBS was set to transmit all of the $1064\ \text{nm}$ light into a beam dump. This means that only the $532\ \text{nm}$ light should be reflected onto the detector, although it should be noted that the PBS will still reflect some (approximately 2%), of the $1064\ \text{nm}$ light. Fig.(4.6) shows the detected power as a function of flash lamp voltage. This is a less effective method of power control than the PBS array but $532\ \text{nm}$ is so far from the design wavelength that the second PBS proved little control. Powers were measured with the thermal detector as before.

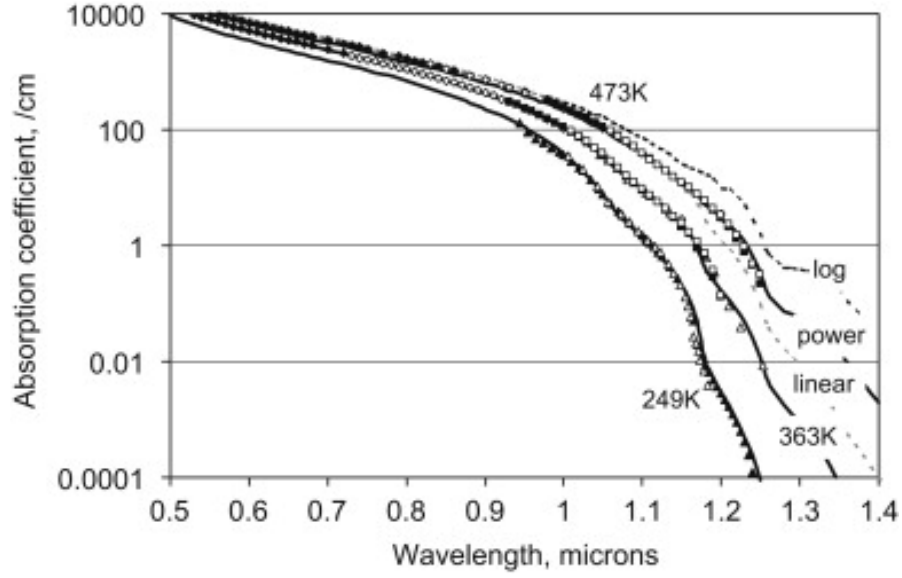


FIGURE 4.5: The absorption coefficient of silicon as a function of wavelength and for different temperatures ([86]). The absorption coefficient at 532 nm is 100 times that of 1064 nm

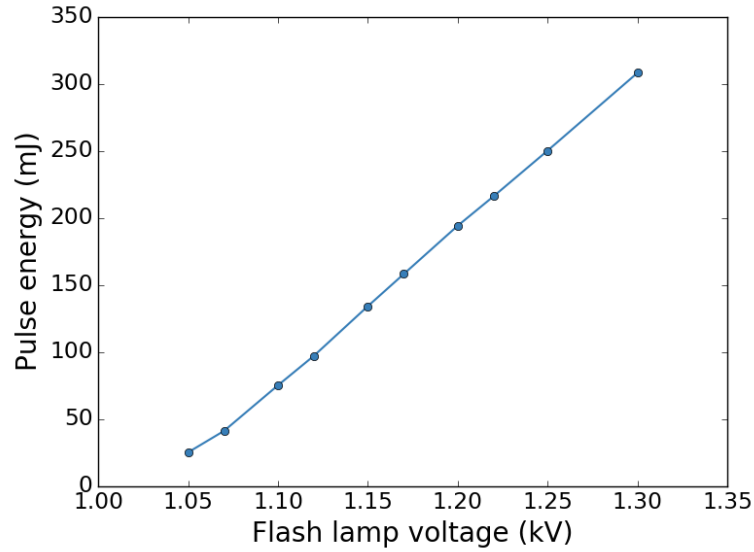


FIGURE 4.6: Laser power as a function of flash lamp voltage for the 532 nm second harmonic of the YAG laser. Measured using the thermal sensor head and using the high power PBS to filter off the fundamental wavelength of 1064 nm.

A systematic study of the ablation of silicon with a single pulse of 532 nm at different powers was carried out to find the best power for the final experiment. There needs to be significant particle generation, in the correct size range, without concurrently generating debris and reform on a scale that would affect the experiment. To explore this a chip was setup inside the vacuum chamber with the surface to be ablated facing up. This should ensure most of the material released returns to the surface to be studied. The laser was brought down perpendicularly to the surface and the chamber was pumped down to 10^{-5}

mbar to more closely mirror the final experiment. This last point is important as the presence of a buffer gas will affect particle size.

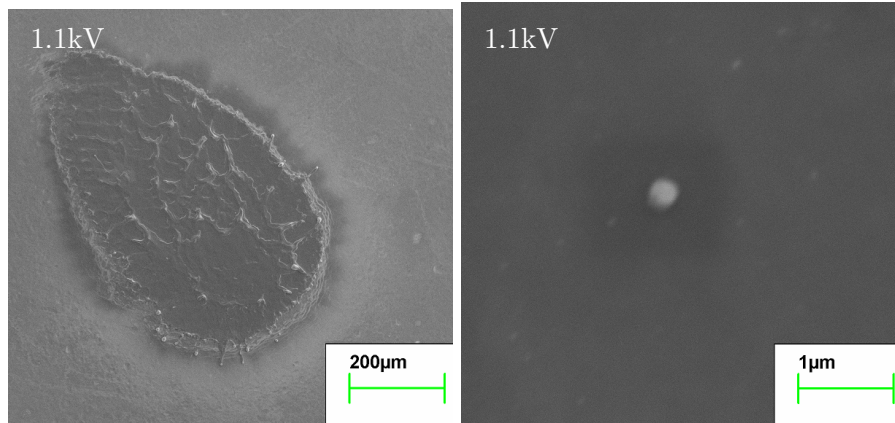


FIGURE 4.7: Pulse energy of 75 mJ. The ablated area is $720 \mu m$ by $430 \mu m$ and there is $25 \pm 5 \mu m$ of reform around the edge. Beyond the reform edge there is a distribution of nanoparticle sizes but many are in the 100 nm range and are mostly spherical with minimal deformation due to skidding along the surface on impact.

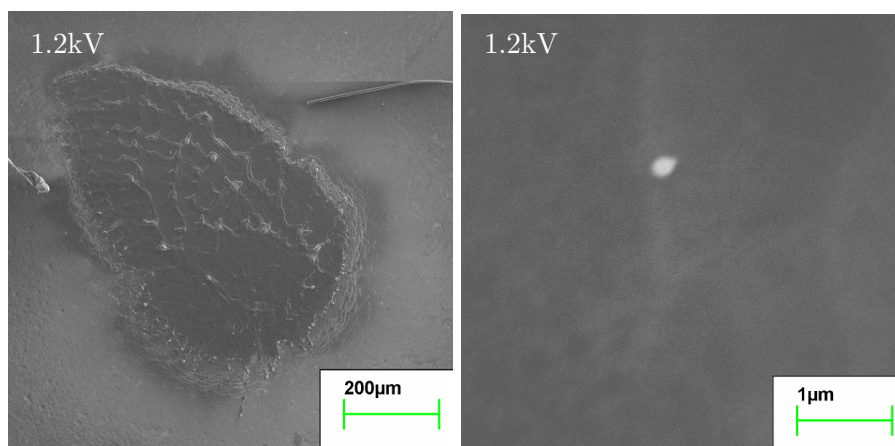


FIGURE 4.8: Pulse energy of 192 mJ. The reform edge has increased to $50 \pm 20 \mu m$ and there is an increase in particle velocity seen by the increase in tail length. There are still many usable particles beyond the reform edge.

Figs.(4.7-4.11) shows the results of these tests, showing both an overview of the focus site and also an image of the most common particles seen in the debris after a single laser pulse. The amount of reform at the edge of the focus zone is seen to increase significantly with laser power along with the velocity of the ejected particles. Trails became visible at 1.3 KV indicated not only that they are moving at high speed but also that they were larger and possibly in a liquid phase. The number of high velocity particles increased with power, as did the length of the trails so it seems fair to assume they are moving faster and/or are larger than the lower power particles. From these results it can be concluded that the lower powers are preferable for the generation of 100 nm sized particles with minimal reform and large scale debris. This is in agreement with the results from other groups discussed earlier in this report.

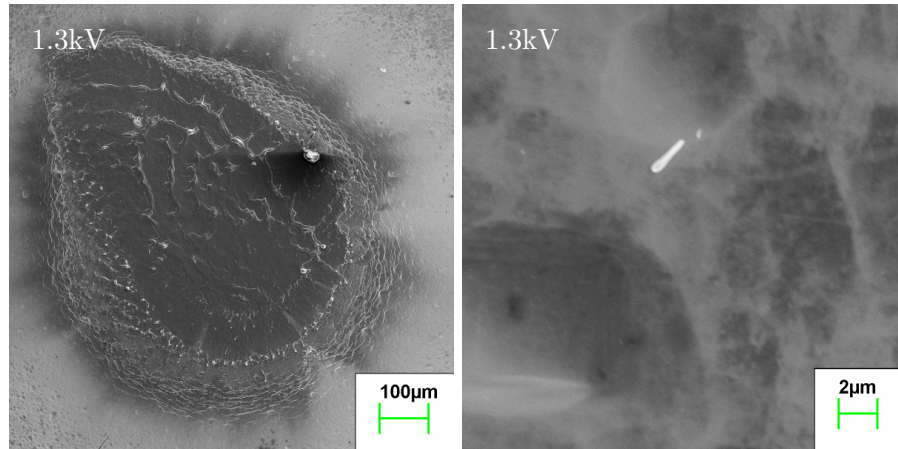


FIGURE 4.9: Pulse energy of 308 mJ. The reform edge has increased to $100 \pm 30 \mu m$ and there is now visible burning and darkening of the surface. The particles are now quite fast given by their long tails and are more in the $1 \mu m$ range.

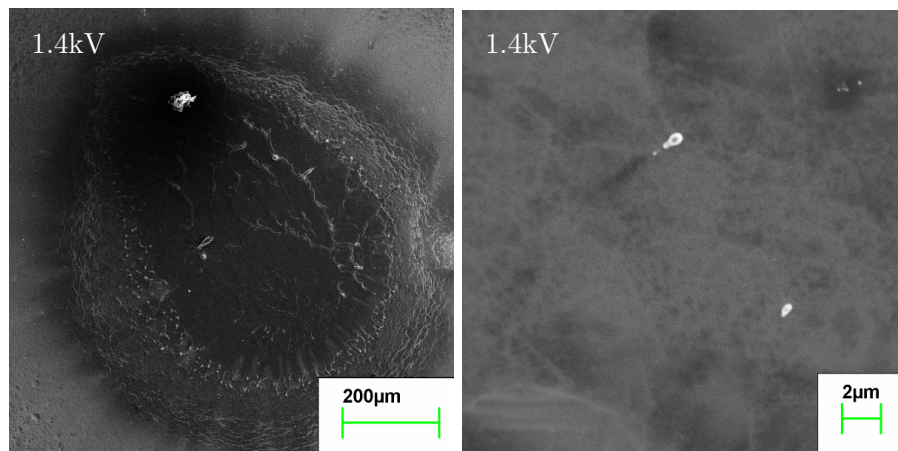


FIGURE 4.10: Pulse energy of 425 mJ. The reform edge has increased to $130 \pm 20 \mu m$ and there is considerable damage to the surrounding area. Looking further out than before it is still possible to find particles although they are large and clearly in a liquid state on impact.

4.4.2 Air trapping

Using the ablation particle generation technique while at atmosphere allows particles to flow around the chamber and become trapped. Using this technique a $\varnothing 70 \pm 3 \text{ nm}$ particle was trapped and pumped down to 3 mbar as shown in Fig.(4.12). The insert shows the trapped particle imaged with a HeNe laser and a Thorlabs CMOS. This experiment was done early in the PhD which is why the signal is noisy and the peak is low compared to later work. This method of trapping was reliable but it is still being performed at atmosphere.

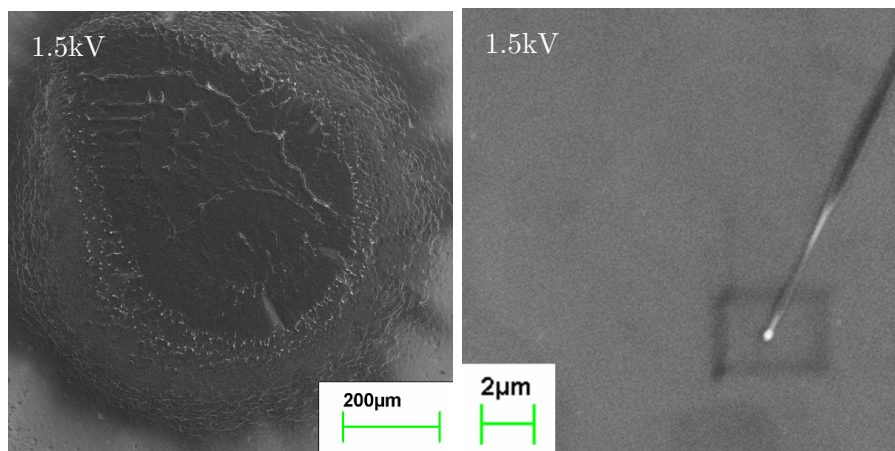


FIGURE 4.11: Pulse energy of 542 mJ. The reform edge has increased to $175 \pm 30 \mu\text{m}$ with a damaged area now extending out to 0.5 mm from the focus centre. Most particles are now $< 2 \mu\text{m}$, in a liquid state and travelling at high velocities

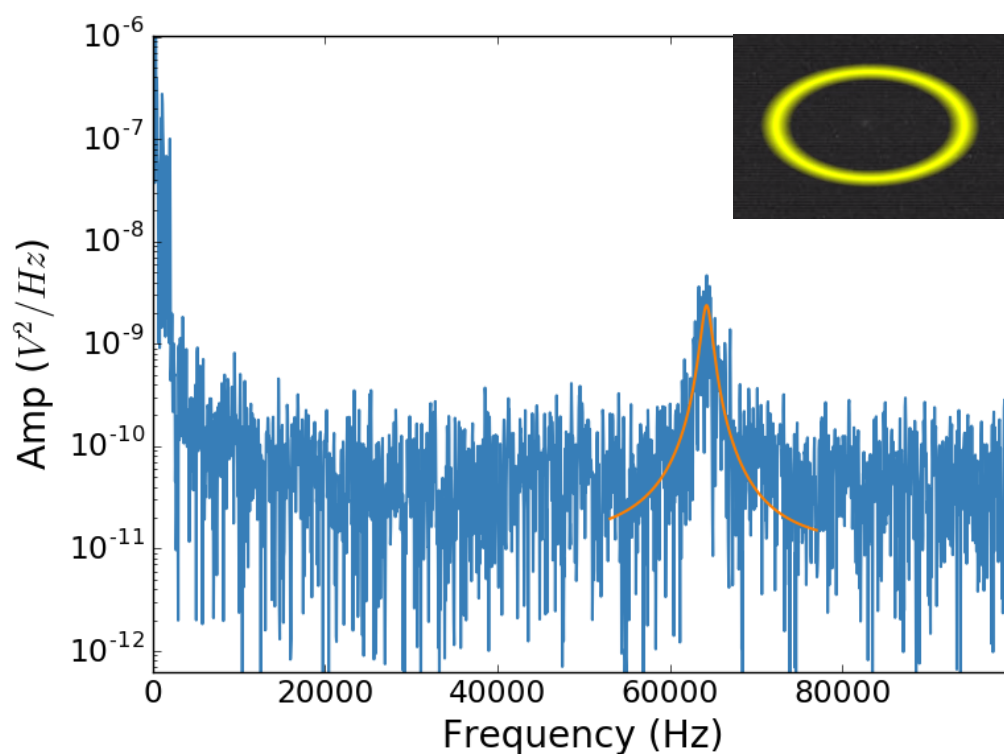


FIGURE 4.12: $\odot 70 \pm 3 \text{ nm}$ particle generated by ablation of a silicon substrate. The particle was initially trapped at atmosphere but here the Z frequency peak is shown at 3 mbar.

4.4.3 Draw backs with ablation as a source

There are a few disadvantages to using this method as a source. The particles produced are likely ionised and so will interact with any electric fields or even metals which may affect force sensitivity. Ablation also produces a lot of mess in the form of reform and particles outside of the desired range. These may be trapped by mistake or more

worryingly coat surfaces and optics. A serious issue is that ablation requires the use of very high power lasers which deposit a lot of energy near a very sensitive experimental setup. It has already been observed that the laser pulse interferes with cameras and detectors even when they are far from the vacuum chamber, so there is a serious concern that the experiment could be permanently damaged. For these reasons less aggressive methods were explored. The first was to attempt the "lift" method and the second was to use pre-made particles and remove them from a surface in a similar fashion to laser cleaning.

4.5 Thermo-mechanically induced lift

The "lift" method involves firing the laser at one side of a silicon chip (backside), thereby causing the release of particles on the other side (frontside) via the thermo-mechanical stress induced by ablation. Asenbaum et al.[87] had success with this and were able to eject a particle with a diameter of around 100 nm and cool its motion with an optical cavity. The stress of the thermal expansion on the backside causes cracks and damage on the frontside and the shockwave from a subsequent laser pulse propels the debris off the surface. The particles range from 100 nm to 1 μm in diameter with this method and have a launch velocity of 1 m/s. An attempt was made to reproduce this with Fig.(4.13) showing an SEM of a chip after 50 shots at 425 mJ pulse power focused with a 50 mm lens. There is clear damage to the frontside of the chip but no nano-particles are visible and nothing was seen at the trap site. Multiple powers were tested but it was not possible to trap any of the resulting debris for analysis. It is likely that any particles being made are either too large, or there are simply not enough of them to trap reliably.

4.6 Desorption of Particles from Glass

Desorption tests were carried out using a 250 mm focal length AR coated spherical lens and 100 nm silicon particles drop coated on to a glass slide. The idea being that the pulse laser should be able to deposit enough energy into the nanoparticles to cause them to overcome the Vann de Waals force holding them to the surface without causing damage to the nanoparticles. Removal of particles was demonstrated but it was observed that the density of nanoparticles seemed to affect the degree of damage to the glass slide and also the removal rate. The nanoparticles were simply drop coated on the slide with Isopropanol and drying effects cause particles to gather at the boundaries of the droplets.

The images shown in Fig.(4.14) show the difference in particle removal due to an increase in particle density, the right having the higher density. It can be seen that larger densities

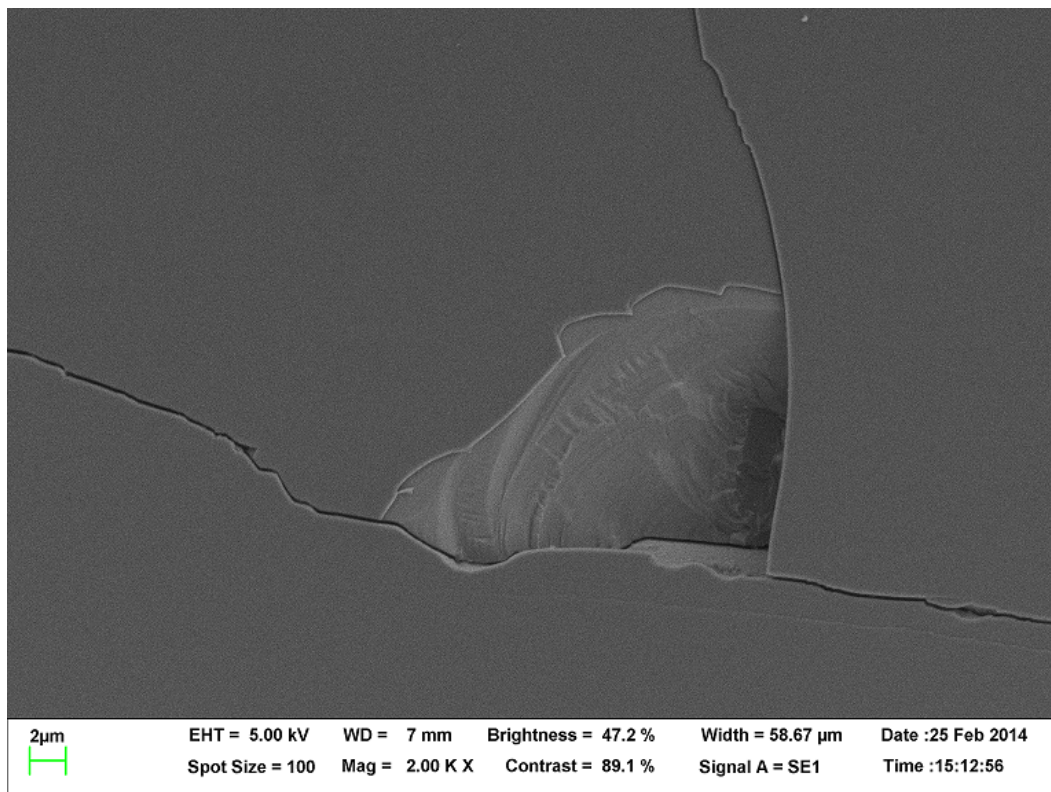


FIGURE 4.13: Back side crack and missing material from a Silicon chip after being hit with 50 shots at 425 mJ from the YAG laser. No nanoparticles are visible and it was not possible to trap any of the debris that was removed in this manor.

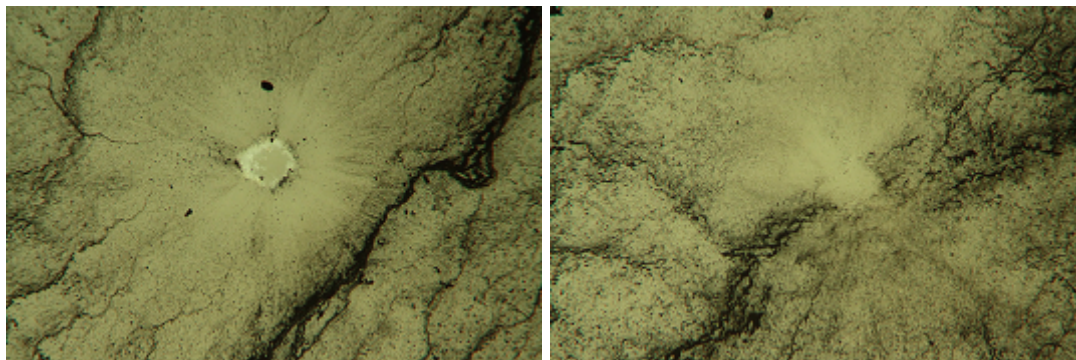


FIGURE 4.14: 100 nm Silicon particle drop coated onto glass slides then shot with a single shot at an average laser power at 25 mW. Again the damage and particle removal are related to the particle density.

prevent damage to the glass as the energy is absorbed by the nanoparticles before it can damage the glass. In both cases the particles are removed from the surface but the clumping of the nanoparticles is likely to result in large clusters of particles rather than individual nanoparticles. It would therefore be advantageous to be able to control particle density across the slide in some manner, or at least reduce the variation in particle density and make it more homogeneous.

4.7 Particle density control

It was shown in the previous section that the density of particles within the focus of the laser affected the removal rate and the damage to the underlining substrate. To fully explore this a study was performed using glass slides with differing concentrations of particles. 0.0998 g of $\varnothing 100$ nm Silicon powder was mixed and sonicated in 50 ml of Isopropanol, giving a starting concentration of 2 mg/ml. This mix was diluted further with Isopropanol in 8 ml beakers with the details of the amount of Silicon that can be expected in each mix and their concentration given in Tab.(4.1).

Beaker Label	Ratio	Amount of Silicon	Concentration
#1	Initial	16 mg	2 mg/ml
#2	1:1	8 mg	1 mg/ml
#3	1:3	4 mg	0.5 mg/ml
#4	1:7	2 mg	0.25 mg/ml
#5	1:15	1 mg	0.13 mg/ml

TABLE 4.1: Dilution rates of $\varnothing 100$ nm Silicon particles in powder form with Isopropanol. These are used later for the desorption experiments.

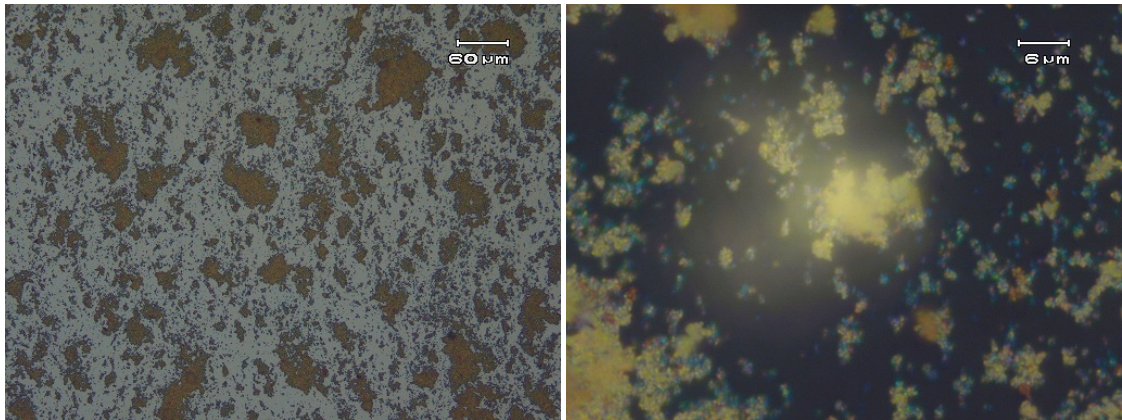


FIGURE 4.15: Initial mix. Both images are on the same area with the right image at a high magnification. There is a Large variation in cluster sizes from $60 \mu m$ down to $2 \mu m$. This makes it difficult to judge the power needed to remove the particles cleanly from the surface.

Fig.(4.15-4.19) show microscope images of the difference concentrations mentioned in Tab.(4.1). The microscope slides were cleaned by sonication for 10 minutes in Acetone and then rinsed in Isopropanol. 100 μl of fluid from the selected pot was drop coated on to the slide carefully to minimise impact force and velocity induced spread. By using the power control methods discussed in Sec.(4.3), desorption tests were performed on the slides to determine an optimum level. These again used the 250 mm focal length lens

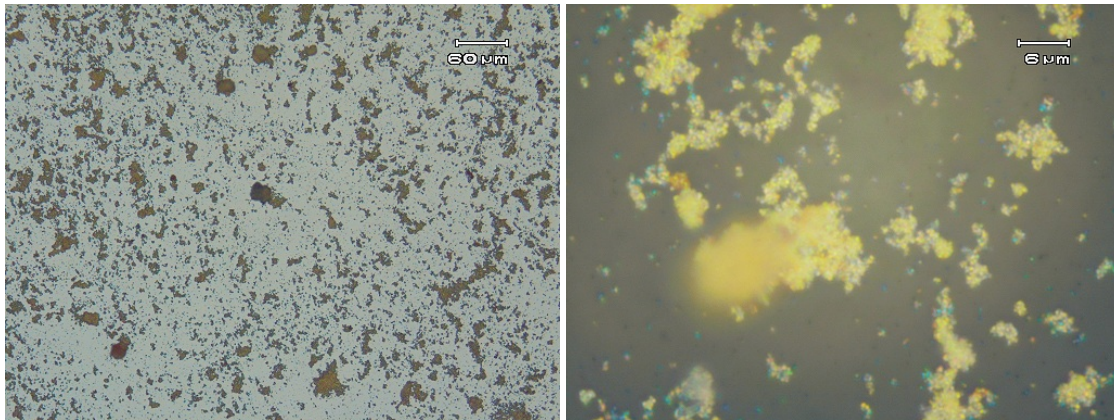


FIGURE 4.16: 2 mix: 8 mg of Silicon. Much more uniform and smaller cluster sizes.

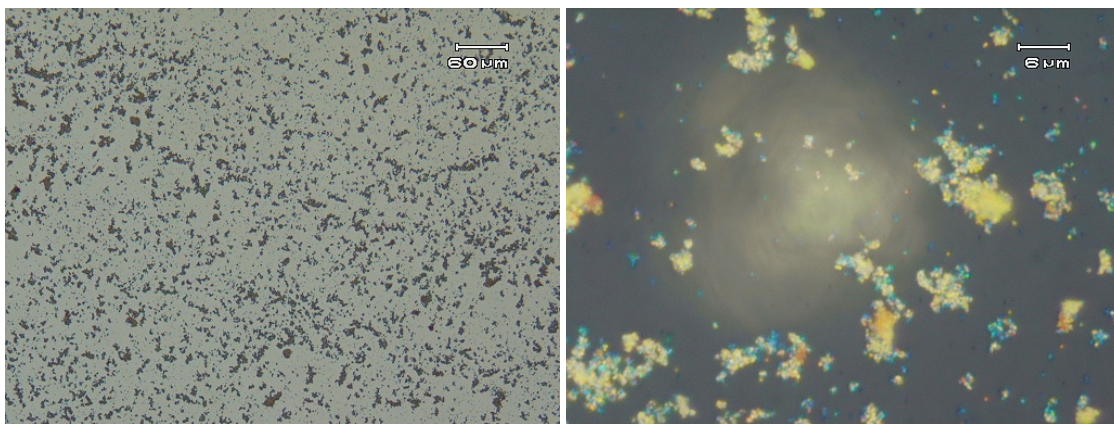


FIGURE 4.17: 3 mix: 5 mg of Silicon. The cluster size is much more uniform with a distribution of $6 \pm 2 \mu m$ although there is also a large number of sub-micron clusters.

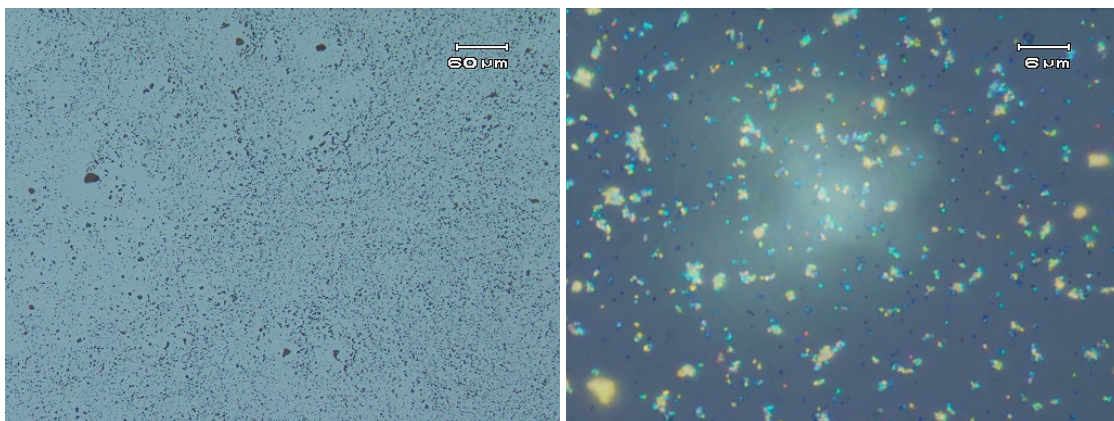


FIGURE 4.18: 4 mix: 2 mg of Silicon. The uniformity is improve further and with a distribution of $2 \pm 1 \mu m$.

and with the slide at its focus. An x indicates were the data was found to be missing at the time of writing however there is still enough to see the overall trend.

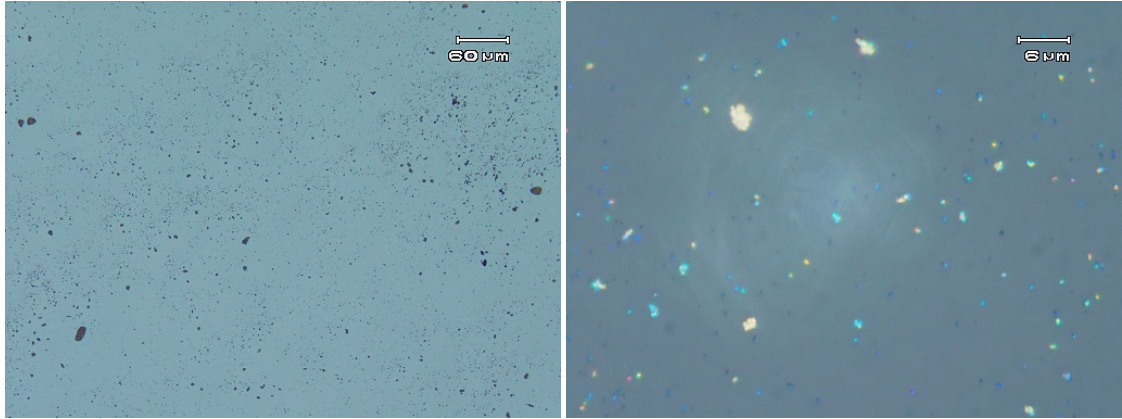


FIGURE 4.19: 5 mix: 1 mg of Silicon. Here the dilution has resulted in large spaces between clusters without much improvement in cluster size.

The laser struggled to clear all the clusters from mix 1 and 2 and even the denser mixes resulted in damage at 6 mJ. There is a fine line between lift and ablation as Fig.(4.20) shows an impact pattern very similar to the direct ablation of Silica experiments performed earlier. Mix 3 shows damage at 2.6 mJ and this would have been worse for the more diluted mixes. The best results are with mix 4 and 5 and with 1.5 mJ pulse energy. As mix 5 doesn't improve on mix 4 it was deemed best to use mix 4 (0.25 mg/ml) and a 1.5 mJ pulse. Trap attempts were made in atmosphere but nothing trapped. This is because the number of released particles is still small compared with direct ablation, but it could also be the result of damage to the particles by the laser during release.

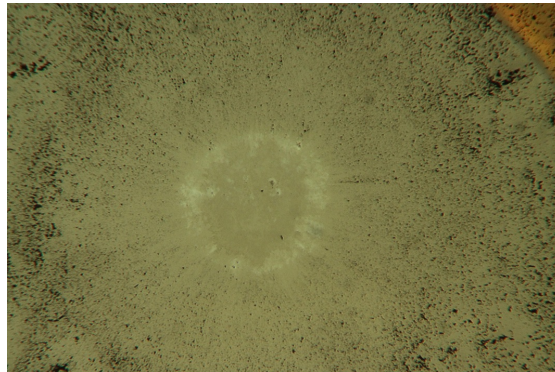


FIGURE 4.20: Ablation of Slide 2 using 80 mW of power focused with a 250 mm lens. There is substantial damage to the glass slide which could lead to the release of fragments which would effect the experiment or damage equipment.

4.8 Conclusion

It was possible to trap particles by generating them directly in the chamber using an ablating source. Due to the limits of the Nd:YAG laser used, a large number of the particles produced were too large to trap. However, as the size distribution is thermal

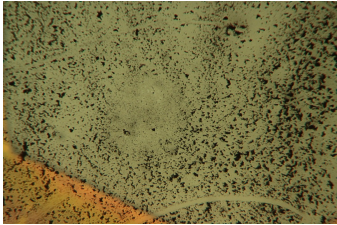
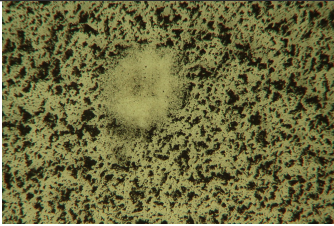
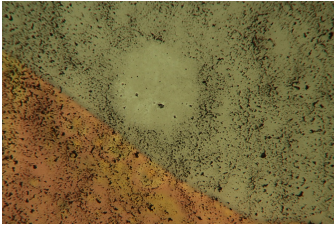
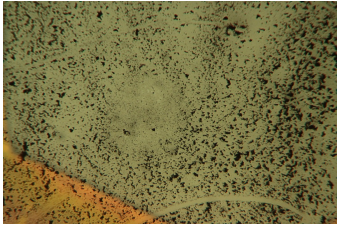
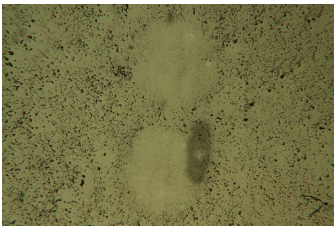
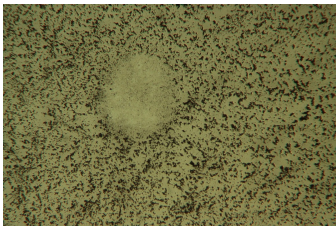
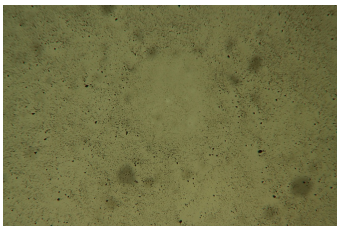

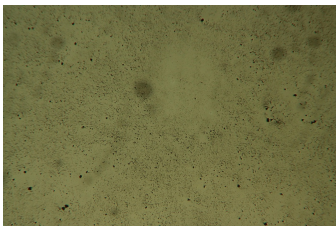
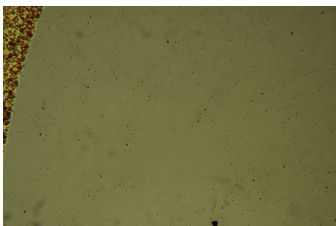
#	6 mJ	2.6 mJ	1.5 mJ
1	<div>x</div> <div></div>	<div></div> <div></div>	<div>x</div>
2	<div></div>	<div></div>	<div>x</div> <div></div>
3	<div>x</div> <div></div>	<div></div>	<div></div>
4		<div>x</div>	<div></div>
5	<div>x</div>	<div>x</div>	

TABLE 4.2: Desorption experiments performed with different concentrations and laser powers. Some images were found to be missing at the time of writing this thesis however the general effects can still be seen. At higher concentrations higher laser powers were needed to remove all of the particles. At the lower concentrations there was a fine line between removing the particles and damaging the glass as the particle density isn't uniform and this greatly affects the amount of energy absorbed.

there are still smaller particles available. An example of a particle trapped at atmosphere is shown in Fig(4.12) with a radius of 35 ± 3 nm. While promising there were still significant challenges with this method. Firstly, the particles produced at vacuum are likely to be travelling very fast and therefore passed though the trap faster than the cooling electronics can catch them. This could be solved with the FPGA but there is a larger issue. The energies involved to generate the particles are very large and are easily able to damage the measurement equipment. Given the speed of the particles

it is difficult to protect the detector and still have it be in a functional state for the cooling. Another idea was to give the particles just enough energy to leave the surface using the laser. This is less dangerous to the detector although it was discovered that the required laser power varied considerably depending on the number density of the particles in the focus. Steps were taken to produce a more uniform distribution and minimise the number of large clusters. While this worked to some extent, ultimately the particles released were either too large or the release density wasn't large enough to trap. Even at these lower powers it was still deemed too dangerous for the equipment to use this as a reliable source, so another idea was developed.

Chapter 5

Sonicating Source

5.1 Van de Waals force

If a surface is moving and then stops abruptly while an object is on it, then that object will continue moving at the original velocity. For large objects the strongest forces that will counter this movement are friction and gravity but for nanoparticles the van de Waals force (vdW) must be considered. There are many intermolecular forces and vdW can refer to one or all of three forces: the force between permanent dipoles (Keesom force), the force between a permanent dipole and a corresponding induced dipole (Debye force), or the force between instantaneously induced dipoles (London dispersion force). These forces are generally attractive but can also be repulsive depending on the dipole alignment or a negative effective Haymaker constant[88][89]. These experiments will be using Aluminium substrates and silicon particles, both of which have no permanent dipoles so the important force is the London dispersion force. This force can be modelled as a pair wise interaction between the neural molecules using the Lennard-Jones potential,

$$U_{LR}(r) = \epsilon \left(\left(\frac{r_0}{r} \right)^{12} - 2 \left(\frac{r_0}{r} \right)^6 \right), \quad (5.1)$$

where r is the separation between the molecules, ϵ is the depth of the potential well and r_0 is the turning point where $\frac{dU}{dr} = 0$ [90]. The r^{-12} term is an approximation of the repulsive force due to Pauli exclusion principle as the molecules are forced close together by an external force. For the work presented here it is enough to focus on the r^{-6} term for the attractive van der Waals force. So for $r > r_0$ Eq.(5.1) becomes,

$$U_{LR}(r) \approx \frac{-2\epsilon r_0^6}{r^6} = -\frac{C}{r^6}, \quad (5.2)$$

where $C = 2\epsilon r_0^6$. To compute the force between a particle and a plane both volumes must be summed over with Eq.(5.2). This will give the interaction energy which can then be differentiated to get the vdW force. This method is known as the Hamaker approximation[91]. For the effect of the particle on the plane the particle is assumed to be point like. The distance from the particle to a point in the plane is r . If z is the tangential distance to the planes surface from the particle, x is the depth into the plane and y is the radial distance from z then $r = \sqrt{(x+z)^2 + y^2}$ as shown in Fig.(5.1)[92].

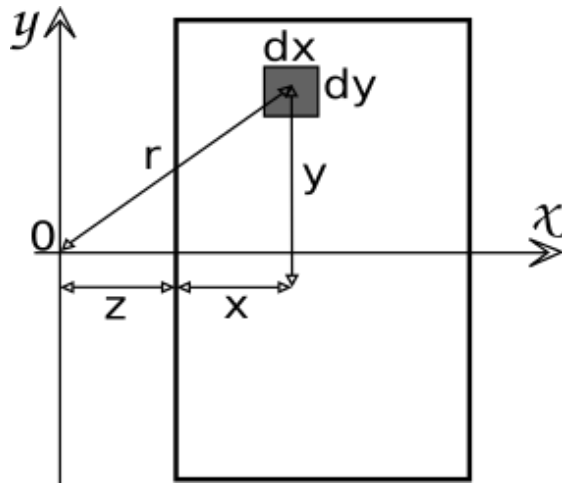


FIGURE 5.1: Coordinate system used to integrate u_1 [92]. The particle is assumed to be point like for this integral and is located at 0. The distance to the element of the ring volume is $r = \sqrt{(x+z)^2 + y^2}$ and the volume is given by $dv = 2\pi y dy dx$.

The plane can be broken up into rings of equal potential with a volume given by,

$$dv_1 = 2\pi y dy dx. \quad (5.3)$$

Bringing these together gives,

$$\begin{aligned} u_1 &= - \int_{v_1} \rho_1 \frac{C}{r^6} dv_1 \\ &= -2\pi \rho_1 C \int_0^\infty dx \int_0^\infty \frac{y dy}{((x+z)^2 + y^2)^3}, \end{aligned} \quad (5.4)$$

where ρ_1 is the number density of the material. It doesn't matter which order the integrals are performed and it is simpler to start with du_1/dy . Let $B = (x+z)^2$ as it

isn't needed and then let $u = B + y^2$ so that $du = 2ydy$ and the limits now go from B to ∞ . This gives,

$$\begin{aligned}
 \int_0^\infty \frac{ydy}{((x+z)^2 + y^2)^3} &= \int_0^\infty \frac{ydy}{(B + y^2)^3} \\
 &= \frac{1}{2} \int_B^\infty \frac{du}{u^3} \\
 &= -\frac{1}{4B^2} \\
 &= -\frac{1}{4((x+z)^2)^2}.
 \end{aligned} \tag{5.5}$$

This is then used in a similar method with the remainder of Eq.(5.4) to give the interaction energy between a molecule and a plane.

$$\begin{aligned}
 u_1 &= \frac{p_1 C \pi}{2} \int_0^\infty \frac{dx}{(x+z)^4} \\
 &= \frac{p_1 C \pi}{2} \int_z^\infty \frac{du}{(u)^4} \\
 &= -\frac{p_1 C \pi}{6} \frac{1}{z^3},
 \end{aligned} \tag{5.6}$$

where $u = x + z$ so that $du = dx$. This can then be used as the input for the interaction between the plane and a sphere. In this case the potential will have layers of equality through the sphere at a distance a from the point of the sphere closest to the surface. Let $z = r_0 + a$ where r_0 is the distance between the surface of the plane at the closest point of the sphere. A slice through the sphere will have a volume of $\pi y^2 da$. The use of intersecting chords theorem[93] gives $y^2 = a(2R - a)$ as shown in Fig.(5.2), where R is the radius of the sphere. Assuming that the particle is close to the surface compared to its radius, then the element of volume becomes $dv_2 = 2\pi R a da$.

The final interaction energy between the particle and the plane can then be computed. This is given in Eq.(5.7) with $A = \pi^2 \rho_1 \rho_2 C$ being the Hamaker constant. For this work it is taken that $A = 10^{-19}$ J.

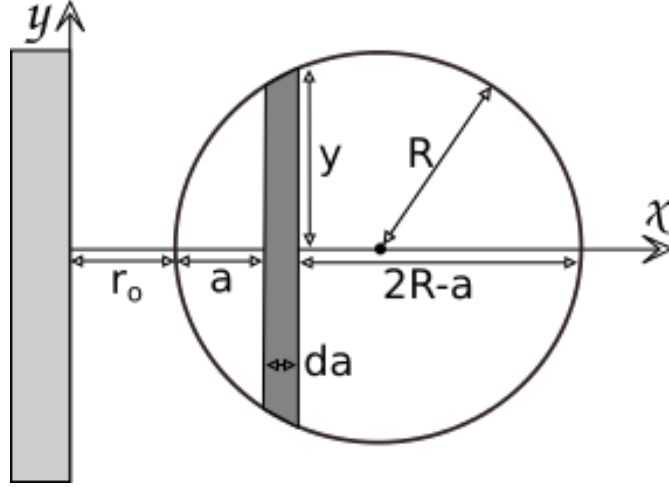


FIGURE 5.2: The coordinate system used to integrate u_2 [94]. Here there are slices of equality from the surface which have a volume of $dv = 2\pi Rada$ where it is assumed that the particle is much closer to the surface than its radius.

$$\begin{aligned}
 U &= \rho_2 \int_{v_2} u_1 dv_2 \\
 &= -\frac{\rho_2 \rho_1 C \pi}{6} \int_{v_2} \frac{dv_2}{z^3} \\
 &= -\frac{A}{6\pi} \int_0^\infty \frac{2\pi Rada}{(r_0 + a)^3} \\
 &= -\frac{AR2}{6} \int_0^\infty \left(\frac{1}{(r_0 + a)^2} - \frac{r_0}{(r_0 + a)^3} \right) da \\
 &= -\frac{AR2}{6} \left[\frac{-1}{(r_0 + a)} - \frac{-r_0}{2(r_0 + a)^2} \right]_0^\infty \\
 &= -\frac{AR}{6r_0}.
 \end{aligned} \tag{5.7}$$

The force between the particle and the surface, as a function of position, is then,

$$F_{vdw} = \frac{dU}{dr_0} = -\frac{AR}{6r_0^2}. \tag{5.8}$$

If this is related to Newton's second law of motion, $F = ma$, then the equation for the acceleration needed to remove the particles from the surface is,

$$a = \frac{AR}{6mr_0^2}, \tag{5.9}$$

where m is mass and a is acceleration. Given that the molecular bond length of Silicon is 0.235 nm[95] it is unlikely that the separation distance (r_0) between the particles and

the metallic surface will be smaller than this. For this reason a separation distance of 0.3 nm is used, giving a required acceleration of $66 \times 10^6 \text{ m/s}^2$ for a $\oslash 1 \text{ }\mu\text{m}$ particle and $6.67 \times 10^6 \text{ m/s}^2$ for a $\oslash 100 \text{ nm}$ particle. To generate this acceleration it was decided to use piezo devices, as they are able to operate at high frequencies and can be made vacuum compatible.

5.2 Piezo electronics

When placed under mechanical stress the piezoelectric effect results in some materials generating an electric field. The external stress causes a deformation of the material and the internal charges move from their original position. In the new position there is a net polarisation caused by the charge imbalance which leads to an electric field. The piezoelectric effect can be seen in a small number of materials including, crystals, ceramics, and a few biological materials such as bone[96]. The most commonly used are the piezoelectric ceramics made from Lead Zirconate Titanate (denoted as PZT and then a number to denote the standard used) which are used in everything from high performance speakers[97], sensors[98], transducers[99], generating surface acoustic waves [100], energy harvesting[101], and medical science[102].

In piezo materials the charge separation due to mechanical stress gives rise to a polarisation given by,

$$\mathbf{P} = \mathbf{d} \times \mathbf{T}, \quad (5.10)$$

where \mathbf{P} is the polarisation vector, \mathbf{d} is the strain coefficient and T is the stress vector. The resulting electric field causes a strain ($\Delta L/L$, where L is the original length) given by,

$$\mathbf{S}_{pe} = \mathbf{d} \times \mathbf{E}, \quad (5.11)$$

where \mathbf{S}_{pe} is the strain just from the piezo effect and \mathbf{E} is the electric field. The strain can be related to stress as, $\mathbf{S} = \mathbf{s} \times \mathbf{T}$ where \mathbf{s} is known as the compliance coefficient. Similarly the stress from \mathbf{S}_{pe} is given by $\mathbf{T} = \mathbf{c} \times \mathbf{S}$ where \mathbf{c} is the elastic constant[103]. This allows a pair of equations to be made,

$$\mathbf{P}_{pe} = \mathbf{d} \times \mathbf{T} = \mathbf{d} \times \mathbf{c} \times \mathbf{S} = \mathbf{e} \times \mathbf{S}, \quad (5.12)$$

$$\mathbf{T}_{pe} = \mathbf{c} \times \mathbf{S} = \mathbf{c} \times \mathbf{d} \times \mathbf{E} = \mathbf{e} \times \mathbf{E}, \quad (5.13)$$

where it has been assumed that $\mathbf{d} \times \mathbf{c} = \mathbf{c} \times \mathbf{d} = \mathbf{e}$. Recalling that $\mathbf{E} = \alpha \mathbf{P}$, where α is the polarisability, it can be seen that the relationship between stress and the electric field is given by,

$$\begin{aligned} E_{pe} &= \frac{\mathbf{P}}{\alpha} \\ &= \frac{\mathbf{d} \times \mathbf{T}}{\alpha}. \end{aligned} \quad (5.14)$$

In the case of a compressing stress the electric field will align to the poling field, with the field reversed if the material is under tension[103], but the interesting thing for the work presented here is that this effect works in reverse. That is, if an electric potential is applied across the material it will expand or compress depending on the direction of the applied field.

With this it is now possible to build the strain-charge coupled equations. For the displacement electric field this gives[104],

$$\begin{aligned} \mathbf{D}_i &= \epsilon_{ik} \times \mathbf{E}_k + \mathbf{P}_q \\ f &= \epsilon_{ik} \times \mathbf{E}_k + \mathbf{d}_{iq} \times \mathbf{T}_q, \end{aligned} \quad (5.15)$$

where ϵ_{ik} is the dielectric matrix. The total strain is[105],

$$\mathbf{S}_p = \mathbf{s}_{pq} \times \mathbf{T}_q + \mathbf{d}_{pk} \times \mathbf{E}_k. \quad (5.16)$$

In general there are 6 degrees of freedom, 3 translational and 3 shear modes. This work will only be considering the 33 mode which is the thickness mode (z) with the applied electric field also in this direction. The relation between the applied potential and the change in the thickness of the piezo is quite simple,

$$\begin{aligned} S &= \Delta z / z \\ &= d_{33} V / z \\ \therefore \Delta z &= d_{33} V, \end{aligned} \quad (5.17)$$

where Δz is the change in thickness, d_{33} is the longitudinal piezoelectric strain coefficient and V is the applied voltage. For this work PZT8 is used with $d_{33} = 280 \times 10^{-12} \text{C/N}$ so at 300 V $\Delta z = 84 \text{ nm}$. If the voltage is sinusoidal then the acceleration is,

$$a = -\Delta z (2\pi f)^2 \sin(2\pi ft), \quad (5.18)$$

where t is time, f is the resonant frequency. Combining these equations with Eq.(5.9) gives the smallest particle radius that can be released from a surface,

$$R = \sqrt{\frac{A}{d_{33} V (2\pi f)^2 8\pi \rho r_0^2}}, \quad (5.19)$$

where $\rho = 2650 \text{ kg/m}^3$ and $V = 300 \text{ V}$. For PZT8 $d_{33} = 280 \times 10^{-12} \text{C/N}$, meaning the smallest particle to be released would have a radius of $56 \mu\text{m}$ which is far too large to be useful. The displacement can be increased by using a second resonator either as a membrane or an acoustic cavity. Peter Barker's group at UCL have reported using a membrane to release $1 \mu\text{m}$ particles at 2 kHz. Assuming they are using PZT8, they must have a membrane amplitude of 1 mm which seems possible given they are essentially using a headphone speaker. To increase the displacement it was decided to use an acoustic cavity, as it will also make it easier to connect an ultrasonic horn later on.

5.3 40 kHz transducer

Ultrasonic transducers allow for multiple piezo crystals to be combined and for the resulting strain to be amplified or spread. The transducers mode has to match that of the piezo's and for multiple piezos the driving potentials have to be in-phase. The simplest way is to have just two piezos, with the positive in-between them and connect both the external faces to the negative/ground. To look at how the strain is transferred into the transducer material a COMSOL simulation was performed based on commonly available devices used in ultrasonic baths, see Fig.(5.3). It was found in simulation that the surface deformation was increased from 84 nm for just a plain piezo, up to $40 \mu\text{m}$ for the dual transducer. This would allow particles with a radius of $2.5 \mu\text{m}$ to be released, if this can be realised and coupled effectively.

A number of 40 KHz transducers were purchased from Beijing Ultrasonic. The frequency response of them was explored with Fig.(5.4) showing a sweep from 35 KHz to 45 KHz. Here the y axis is the voltage rather than a direct measurement of displacement so that a drop is a result of resonance. There is a clear drop at 39.1 KHz with a full width

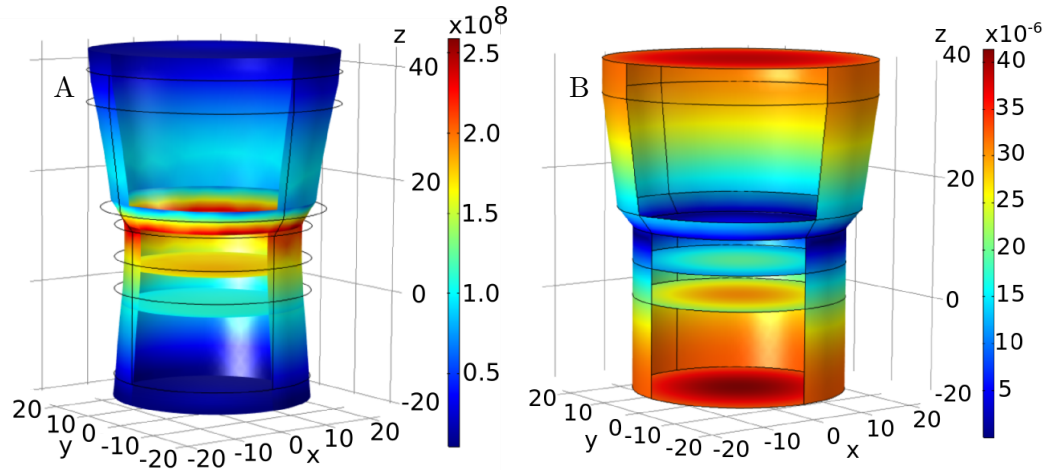


FIGURE 5.3: **A:** Stress in N/mm^2 seen in the transducer on resonance with dimensions in mm. The large stress seen near the piezos is transferred into an increased strain of the aluminium transducer. **B:** Displacement due to the induced stress. The transducer amplitude is $40\ \mu m$ for a voltage 300 V. This should allow much smaller particles to be released from the surface.

half maximum of 250 Hz. This gives a quality factor, Q , of 157 which is less than the 1000 Q mechanical quoted by the suppliers. This is likely due to the control electronics and so a resonant circuit was built by Gareth Savage based on electronics purchased from Beijing ultrasonic. However, these electronics were found to be sub-standard on the part of the supplier and so a system was built using an ENI 2100L power amplifier (first borrowed from Peter Glynne-Jones but later purchased from Test solutions). By using a signal generator the power could then be controlled programmatically allowing for precise pulse timings.

5.3.1 Particle release

Fig.(5.5) is a series of images made with 100 nm particles drop coated directly onto the surface. The transducer was setup from the bottom of the chamber so that the particles were being fired upwards and against gravity. This allowed the release velocity to be estimated with the results shown in Tab.(5.1). The voltage quoted is that supplied by the signal generator with the powers measured off the amplifier at $50\ \Omega$. The circuit was driven on resonance in each image and the chamber was at a partial vacuum of 1 mbar for a quick test. Particle release rate increases with driving power, as does the maximum height the particles reach, however they are still very close to the surface and are unlikely to be useful for trapping. The particles are likely very large and are too close to the surface anyway to be trapped. The surface of the transducer is very rough and the solution was only diluted to 5%, which is still very high. To increase both the

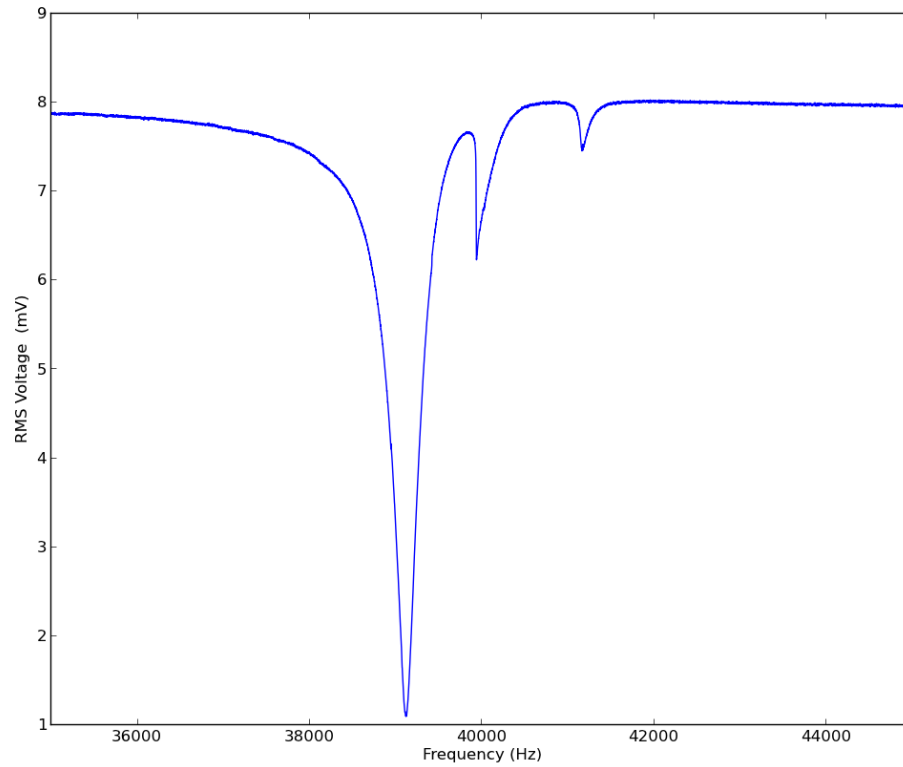


FIGURE 5.4: Frequency response of the 40 KHz transducers. There is a clear drop at 39.1 KHz with a full width half maximum of 250 Hz. This gives a quality factor, Q , of 157.

Image	Supply Voltage (mV)	Power (W)	Max height (mm)	Release Velocity (m/s)
a	100	20	0.16	0.06
b	200	30	0.22	0.07
c	300	40	0.46	0.09

TABLE 5.1: Table of results from the vertical ejection of 100 nm particles off the surface of the 40 kHz transducer. The particles were simply drop coating onto the surface without any special preparation.

transferred energy into the particles and to improve surface finish an aluminium horn was manufactured.

5.4 Ultrasonic Horn

The ultrasonic transducer purchased and used is designed to transmit the vibrations into a water bath to clean components. To achieve this the end of the transducer flairs out to spread the energy, but it would be better for particle release if all the energy was focused down to a smaller area. This is the concept of an ultrasonic horn. It is

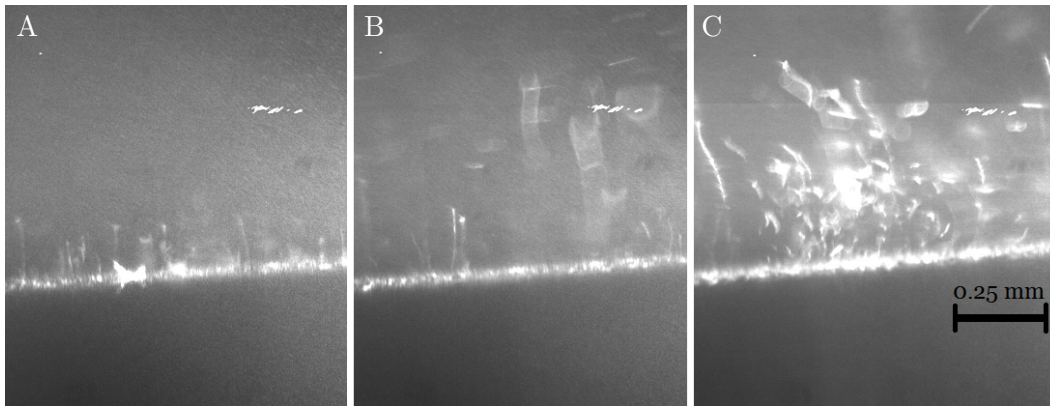


FIGURE 5.5: Particles being thrown from the surface of the 40 kHz transducer at; 20 W (a), 30 W (b), and 40 W (c), of driving power. The heights and release velocities are given in Tab.(5.1)

a device that maintains the overall length of the transducer to be a half wavelength but now with all the vibrational energy focused to a small area. A horn was designed for the transducers being used that was 1 wavelength long, preserving the overall half wavelength, and reduced the diameter down to 3 mm. This increases the energy of the oscillations by the squared ratio of the starting and finishing diameters, so that going from 45 mm to 3 mm gives an increase of 225 times. The amplitude should then increase by $\sqrt{225}$ giving 0.6 mm and allowing $\phi 1.2 \mu\text{m}$ particles to be released. This is a significant improvement but there will now be additional losses due to reflections off the new edges. These can be minimised by placing them at anti-node points or by adding gradients to try and deflect them. A full simulation would require a complete finite element analysis of the device however using the simple ideas outlined above a prototype was manufactured with Fig.(5.6) showing what it looks like attached to the transducer.

The new horn setup was then placed vertically within the vacuum chamber and the area above the tip was illuminated with 0.5 Watts of 808 nm light. The driving voltage was again supplied by amplifying the signal from the TTI TG5011 function generator using a ENI 2100L power amplifier. This allowed the transducer to be powered all the way up to its maximum of 50 watts and multiple release events were observed within the range of 10-20 watts. Vacuum tests were then performed down to 10^{-6} mbar. Fig.(5.7) shows particle release at 10^{-6} mbar with an expanded illumination beam showing clear parabolic curves. This allows the velocity to be calculated as the height can be compared to the diameter of the horn tip seen in the image, 3 mm. This gives the vertical velocities as 0.25 m/s to 0.35 m/s for those that can be calculated. There are some that do not have a maximum height and so it is estimated from the arc. The release rate is still very low so the next step is to improve the surface finish.

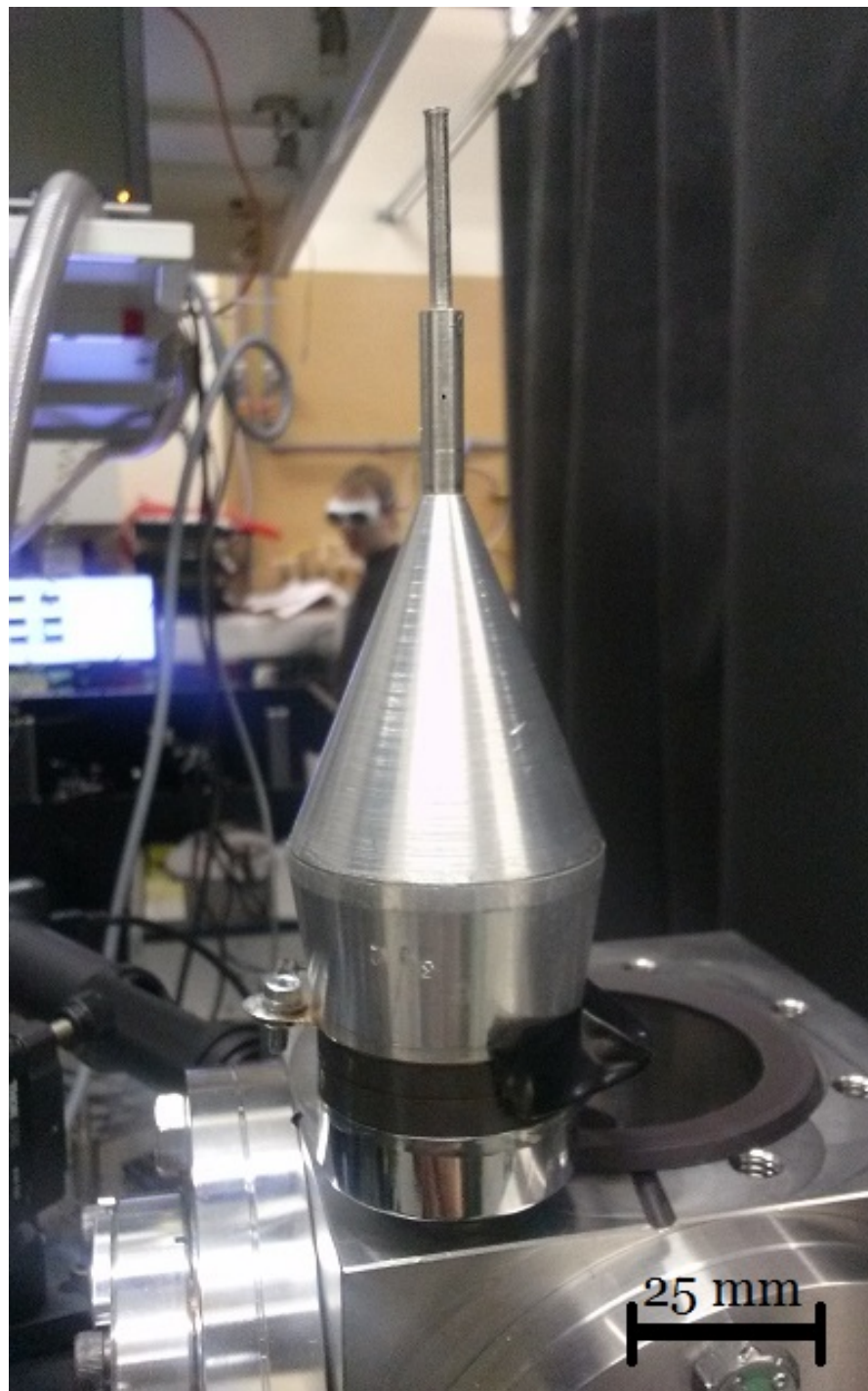


FIGURE 5.6: The prototype ultrasonic horn once finished and attached to the transducer. The length is one wavelength long and the final diameter is 3 mm giving a maximum possible increase for the oscillation energy of 225 times that without the transducer.



FIGURE 5.7: A wide illumination area of particle release at high vacuum, 10^{-6} mbar, with path arcs that allow the velocity to be calculated. The spiral path is assumed to be due to the irregular shape of particle clusters. This particle release was at 10 watts of driving power and the velocities are estimated to be 0.3 ± 0.1 m/s

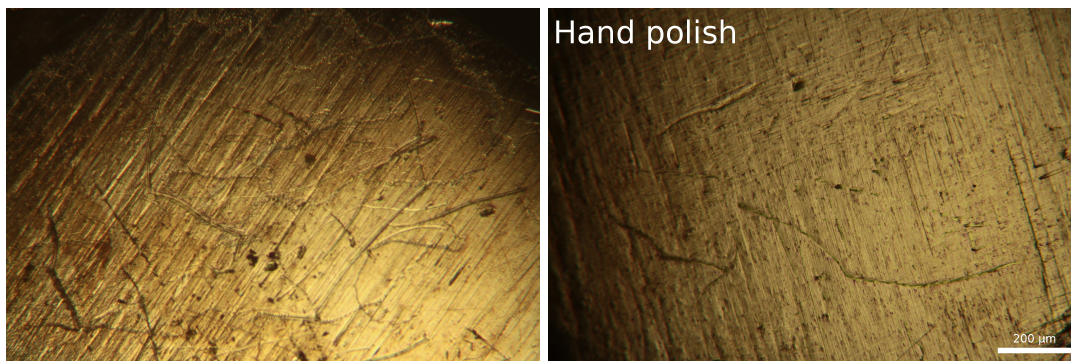


FIGURE 5.8: The surface quality of the tip of the horn before (A) and after (B) polishing with a calico polishing wheel. There is an improvement after polishing but there is still significant surface roughness. Ideally the tip should be optically flat to prevent particles from collecting in the grooves and getting stuck to each other.

5.5 Surface finish

The release rate can be increased by improving the surface finish on the tip. Fig.(5.8) shows a before and after polishing using a calico polishing wheel. There is a clear improvement but there are also still large marks that the particles cluster into as the solution dries after drop coating. Two methods were then performed in an attempt to achieve a mirror-like surface.

The first was to apply a layer of Chrome via thermal evaporation. This reduced the number of viable marks however, as shown in Fig.(5.9.A) the coating could not withstand the forces from the sonication. The other method was to send it to an external company to have a small amount diamond turned off the end. 10 tips were sent to the same

company as used for the parabolic mirror and the results are seen in Fig.(5.9.B). The finish is now mirror-like to the human eye and there are no large marks seen under the microscope. However, there are still small pits and streak marks from the manufacturing process. It may be that a different grade of aluminium would be able to achieve a better finish or that a different process like lapping would be more appropriate[106]. Either way another problem is the pooling of particles in to drying edges that results in large clusters. To remove these a new technique was developed to increase drying speed and produce a more homogeneous distribution.

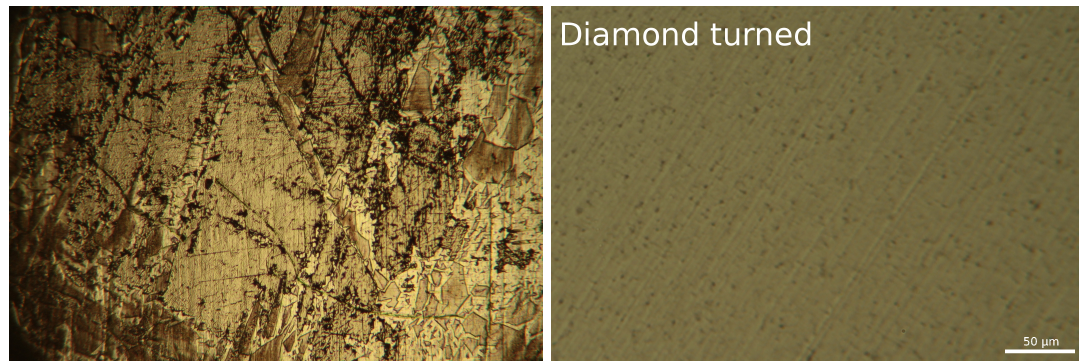


FIGURE 5.9: **A:** A layer of chrome was deposited on to the surface via thermal evaporation but after use the chrome layer has come apart under the mechanical stresses. **B:** 10 tips were sent to Symons mirror technology ltd to be diamond turned. The resulting finish is mirror like to the human eye although there are still small pits and streaks. It might be possible to improve on this in the future by using a different grade of Aluminium.

5.6 Loading

The drop coating method used for the ablation work results in small clusters and single particles but these are also spaced very far apart and low in number. To overcome this a new loading method was developed using the nebuliser and a heat gun. The aim was to dry the particle solution as fast as possible in an attempt to break up the lines that form from with a higher concentration of particles. An example of these lines is shown in Fig.(5.10.A) with $\varnothing 80$ nm SiO₂ particles at a concentration of 1:20 with deionized water. The SiO₂ particles come from the supplier in solution at a concentration of 5% so the final concentration is $265 \mu\text{g/ml}$ of SiO₂ particles to water. This would result in the $\varnothing 5 \mu\text{m}$ droplets seen in Fig.(5.10.A) containing ≈ 25 particles and the larger drying line seen at the bottom of the figure having ≈ 4400 particles. However, as the solution dries it does not deposit the particles uniformly and instead the particles are dragged with the liquid and coalesce to form the features seen. The water has been completely removed so the droplet like features are completely formed from nanoparticles and other residue. To prevent this coalescing the dilution medium was changed to methanol and a heat

gun was used to heat the backside of the glass slide. The temperature was measured using an infrared thermometer to be 160°C . The internal electrics of the nebuliser were removed and the piezo was driven directly using a signal generator. This removes the frequency tracking electronics but it also allows for more control of the driving amplitude and allows better pulse operation.

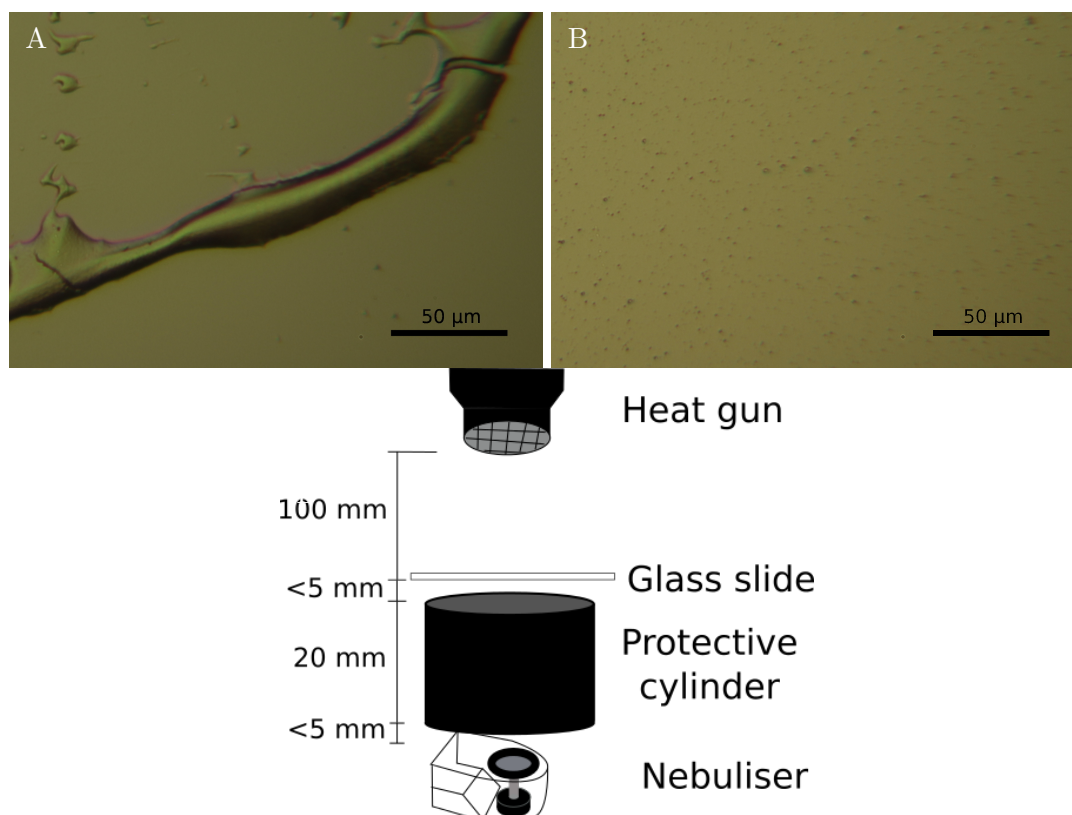


FIGURE 5.10: **A:** As the water dries it draws the particles together forming larger clusters or even structures that look like water marks. These larger clusters are completely unusable for the optical trap. **B:** By using the new drying sequence with methanol the particle distribution can be improved dramatically. There are now no large structures and many sub micron clusters. They are likely many single particles although they are too small to be imaged with the microscope. **C:** Loading setup used to produce **B**. The slide is placed on top of a plastic cylinder with the nebuliser at the bottom. The cylinder allows the spray to expand while protecting it from air currents. The back of the slide is heating with a heat gun using the sequence described.

The apparatus was arranged as in Fig.(5.10.C) and the full sequence operation was as follows,

- Heat gun turned on and system left for 120 seconds to heat slide to 160°C .
- Heat gun turned off and the Piezo driven at 179.08 kHz at 10 V for 30 seconds.
- Piezo off and heat gun on for another 120 seconds.
- Repeat 5 times in total.

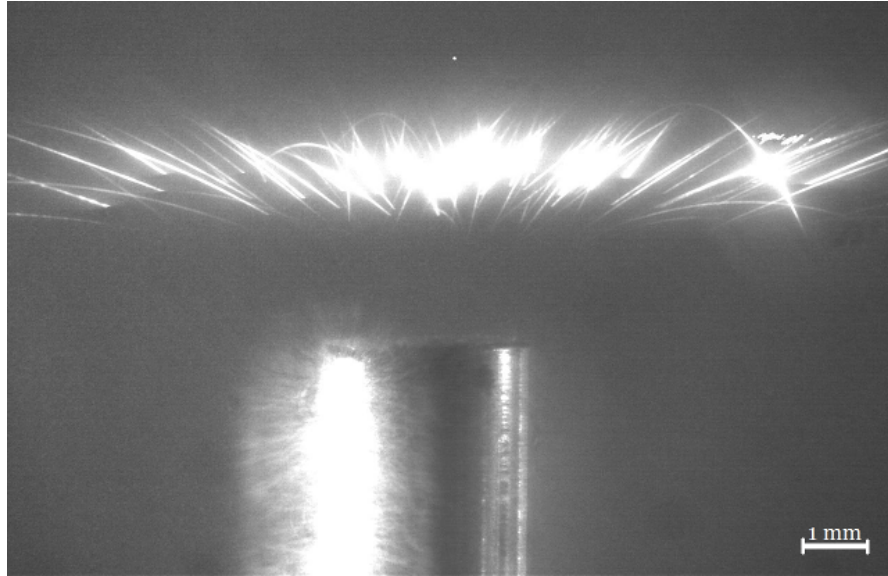


FIGURE 5.11: A larger particle release rate observed in another run at 10^{-4} mbar. This increase is likely due to a difference in particle preparation. This particle release was seen at 15 watts of driving power.

Fig.(5.10.B) shows the result after this procedure. There are no drying lines and the visible clusters are only 3 microns wide. This should result in a much larger number of individual particles and so a higher release rate. Fig.(5.11) shows a much larger release seen after the improvements to particle preparation. The transducer is driven as before at 15 W. The material that is ejected is travelling much faster than before, and so it can be assumed to be smaller. Attempts were made to trap these particles in air, however, nothing trapped. This implied that it is still only clusters with diameters $> 1 \mu m$ that are being observed or that the release density is still low. It is likely that the single particles are simply not being released from the surface in the first place due to the Van der Waals force and losses limiting the amplitude of the surface. To overcome this a much larger acceleration is needed from the piezo, which can be achieved by using a higher frequency piezo.

5.7 MHz

As noted the acceleration of the piezo surface is proportional to the square of the resonant frequency, $a \propto f^2$. So by using a 9 MHz piezo the acceleration can be increased by a factor of 192 over the 40 kHz transducer. To this aim a number of ring piezos were purchased from Piceramic[107]. These have a thickness mode at 9 MHz and a measured thickness of $250 \pm 10 \mu m$, which makes them very fragile. They can also only be run in a pulsed mode at 20 W of driving power as they will reach their Curie temperature of $250^\circ C$ in just a few seconds[108]. With $d_{33} = 500 \times 10^{-12} C/N$ these piezos will

have a maximum displacement of 150×10^{-9} nm at 300 V. This gives an acceleration of 480×10^6 m/s² and with this it should be possible to release $\varnothing 370$ nm particles from the piezo surface, assuming the Hamaker constant is still $\approx 10^{-19}$ J.

The piezos electrical response was measured after it had been mounted onto the tip of a steel rod. The steel rod will allow the piezo to be removed and reloaded easily without interfering with the rest of the experiment. This mounting did result in a shift in the resonance frequency, from 9.1 MHz to 9.6 MHz, and the formation of a few other small resonances, as seen in Fig.(5.12) but this shouldn't have too much of a negative effect.

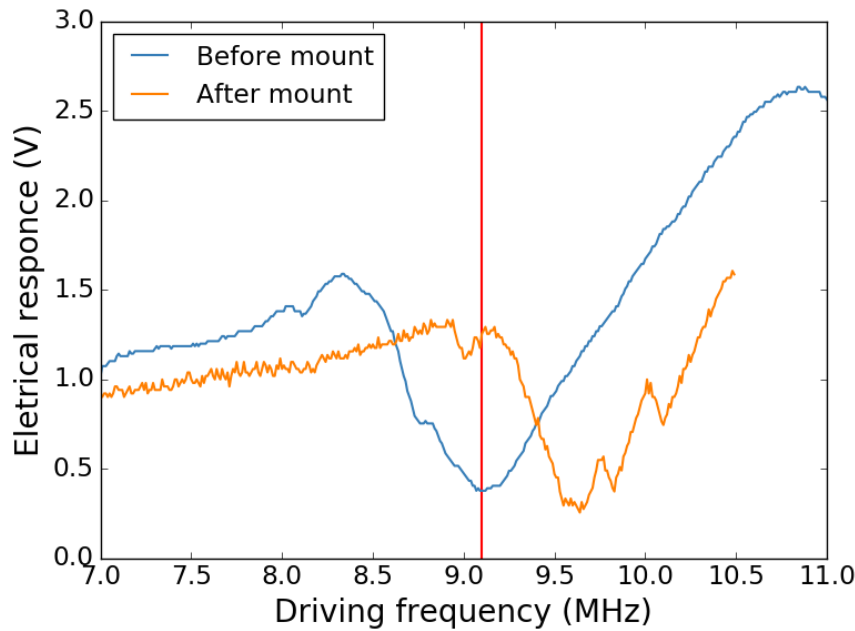


FIGURE 5.12: Electrical response of the piezo ring from PIceramic[107]. The piezo is 250 ± 10 μ m thick and has a resonant frequency of 9 MHz when just connected to electrodes, blue line. Once mounted the resonant frequency moved to 9.6 MHz and a number of other small peaks appeared, orange line. This lowers the Q but the device is still usable for testing.

The surface of the piezo was drop coated with a 0.25% concentration of $\varnothing 160$ nm silica particles in deionised water and placed as close to the trap site as possible using a translation stage. This is a higher concentration than used to produce single particles but here the priority is just to see a release event, which was observed as in Fig.(5.13). The turn on and turn off points can be seen as the piezo is close enough to the trap to scatter collectable light. The trap itself is made with a Thorlabs moulded aspheric with a design wavelength of 1550 nm. With an NA of 0.6 this lens has a larger beam waist of 1.2 μ m but for this test a deep trap is not required and the larger trapping area will in fact help. The chamber is at 4×10^{-4} mbar which is low enough to be high vacuum.

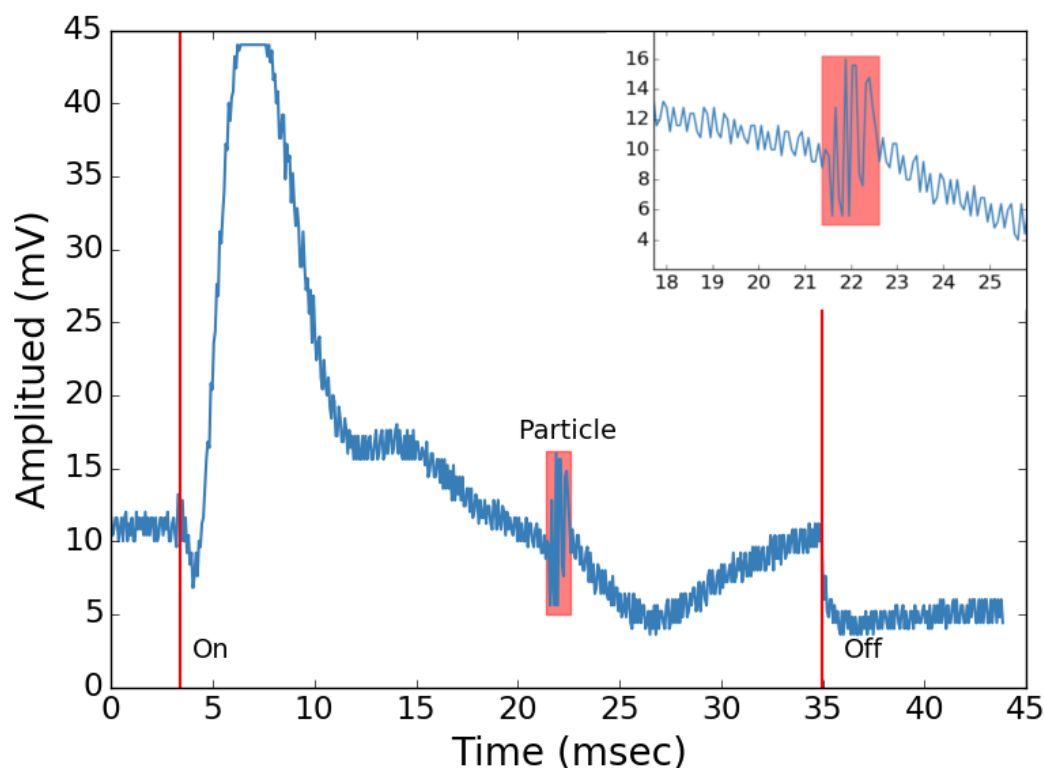


FIGURE 5.13: A 35 ms pulse from a 9 MHz piezo. There is an increase in signal at switch on from the scatter off the piezo. Once this scatter reduces there is a large event at 21 msec, where a particle is measured travelling through the trap.

In Fig.(5.13) the piezo is turned on and there is a large increase in scattered light. It is difficult to say how much of this signal is from particles leaving the piezo and how much is due to the motion of the piezo itself. After a few micro seconds at full power the piezo begins to heat and the resonant frequency shifts just enough to reduce the amplitude. The piezos also had a tendency to loosen the retaining bolts which also contributed to the change in signal. At 21.2 msec there is a sudden jump in signal that lasts for just 1.5 msec before dropping back to the same level as before the event. Given the suddenness of the transition and the magnitude of the signal change it is likely that this is a particle travelling near to or though the trap. Unfortunately there wasn't enough data to produce a PSD and obtain a trapping frequency but this is still a good indication that this method produces particles.

5.8 Conclusion

For small objects, such as nanoparticles, the Van der Waal force is very strong so a significant force is required to over come it. To achieve this force it was decided to use peizo devices as other groups had seen progress with larger particles. Using a 40 kHz

	Δz	$\Omega/2\pi$	R_{min}	a
just piezo	84nm	40 kHz	56 μm	5300 m/s^2
with transducer	40 μm	40 kHz	2.5 μm	$2.6 \times 10^6 m/s^2$
with horn	600 μm	40 kHz	663 nm	$38 \times 10^6 m/s^2$
MHz	150 nm	9 MHz	186 nm	$480 \times 10^6 m/s^2$
MHz + transducer	4 μm	9 MHz	36 nm	$13 \times 10^9 m/s^2$

FIGURE 5.14: Summation of predicted amplitude, acceleration and minimum particle radius that can be released.

PZT 8 transducer from Beijing Ultrasonic it was possible to release large clusters directly from the rough surface validating the work seen by others. Next, the use of an ultrasonic horn to focus the vibration energy allowed for smaller particles to be released at larger heights but the particle density was still very low. By improving both the surface finish of the tip and the loading method to reduce clusters, the particle density was improved greatly as shown in Fig.(5.11). Attempts were made to trap these particles both at vacuum and at atmosphere as worked with the ablation method but unfortunately they were unsuccessful. This was tried multiple times with no success and it was assumed that the particles being released were still too large. To increase the force from the piezo further a number of 9 MHz PIC151 rings were purchased from PIceramic, which also had a strain coefficient twice that of PZT 8 ($d_{33} = 500 \times 10^{-12} C/N$). Using these gave the first indication of a detection signal as shown in Fig.(5.13) but unfortunately it was still not possible to maintain the trap. The use of piezo devices as a neutral particle source is still very promising. So going forward it would be interesting to design a transducer and horn combination that can better transfer the energy into the particles. To improve the particle number density at the trap site after the release event, a way of manipulating their flight path is needed. This would allow either collimation or focusing and could potentially be achieved a number of different ways.

Chapter 6

Particle focusing

The ultrasonic sources show good indications of being a reliable release platform with kHz working well for μm particles and the MHz likely to work for nm particles. However, they are released over a wide range of angles, which results in a low particle density at the trap. It would therefore be useful to devise some way of collimating the particle and control the particle's direction after release. This way more particles can be guided to the trapping site, increasing trapping probability. It is critical that any collimation method does not reduce the already low particle flux so methods such as collimation slits are not helpful, unless the particles blocked can be returned to the tip for future release. Given the expertise in the group an interesting idea is to have a loosely focused beam aimed perpendicularly to the tip surface that would confine the particle's transverse motion, but still allow them to travel vertically to the trapping laser.

6.1 Laser focusing of particles

The particle's velocity is approximately 0.4 ms^{-1} from Fig.(5.11) and most come off at an angle of 45° or less to the vertical. This can be used to calculate the kinetic energy of the particles and then Eq.(2.20) can be used to determine the parameters needed to collimate the particles into a tight beam. As the trapping force is dependent of the particle's position in the trap the motion was broken down into small time steps and summed in a finite element simulation. The chamber is assumed to be at 10^{-5} mbar so that the thermal force is just 1.2×10^{-20} N. This means the focusing intensity can be much less than at atmosphere even though the particles are travelling faster. Even so, more power is required than the 1550 nm laser can provide so an 808 nm pump laser with a maximum power of 60 W was obtained. This was focused using a 0.04 NA lens at a distance of 30 cm. The total force on a $\odot 100 \text{ nm}$ particle in this focus is given

in Fig.(6.1.A) using 50 Watts. Fig.(6.1.B) shows the change in horizontal velocity as the particle moves through the beam for various radial distances from the centre of the focus. It can be seen that particles within a radial distance of $8 \mu\text{m}$ from the centre of the focus will be trapped after a distance of $10.8 \mu\text{m}$. This is a very small focus and so there is less than 100 particles enclosed within this area, assuming $1 \mu\text{m}$ separation of particles. Increasing the focus waist results in having to increase the laser power to very high values. For example to focus particles from a $100 \mu\text{m}$ beam waist requires 5000 W of power at 808 nm. This can be improved by using a laser with a shorter wavelength but that is still a linear relationship. It is unsurprising then, that this method didn't produce any detectable increase in trapping. Therefore other methods of particle collimation and focusing need to be explored.

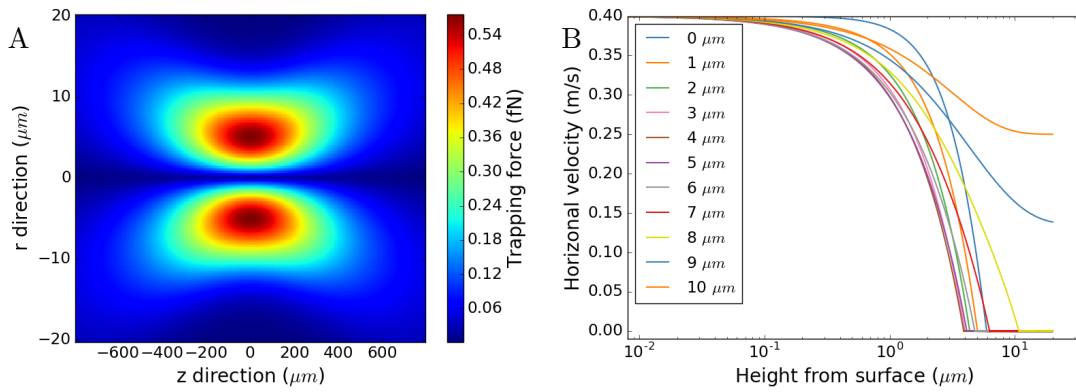


FIGURE 6.1: **A**: Gradient force near the focus of a 0.04 NA lens with 50 W of laser power and assuming a particle diameter of 100nm. This NA is less than the mirror or aspheric lens, but here the particle will already be at vacuum and will be emitted within the focus and so less intensity is needed. **B**: Radical velocity as a function of vertical height as the particle moves through the beam. Each line has a different starting point from the focus centre. Below $8 \mu\text{m}$ a $\varnothing 100 \text{ nm}$ particle should be pulled back to the beam centre.

6.2 Magnetic focusing

It has been mentioned that the particles trapped often have a charge of a few electrons. While it would be preferred if they weren't charged, it also allows the particles to be manipulated with magnetic and electric fields. This would allow for an increase in particle flux density or to even trap them within a Paul trap[109]. A simple method of focusing would be to use magnetic coils and it would have the advantage of not increasing the kinetic energy. A moving charged particle feels a Lorentz force of $\mathbf{F}_L = q\mathbf{v} \times \mathbf{B}$ which causes the particle's path to spiral, leading to a centripetal force of $\mathbf{F}_C = \mathbf{v}^2 m / r$, where r is the radius of the spiral. The complete solution for magnetic focusing is more complex

and is given by Mendel et al.[110], however, a simple understanding can be gained by looking at the balance of \mathbf{F}_L and \mathbf{F}_C . This gives a radius of,

$$r = \frac{vm}{qB}. \quad (6.1)$$

So the radius of the spiral can be reduced by increasing the magnetic field. This can be achieved by passing the particles through the centre of an electromagnetic coil. The particles that pass through the exact centre will be unaffected but the off-centre particles will spiral inwards. The optical trap would be placed at the magnetic focus but it could also be a Paul trap which would greatly increase the chance of trapping. In fact with a Paul trap it might be possible to recycle particles but this would depend on the requirements of the experiment. If the particles are travelling too fast a Stark decelerator can be used to slow them down and allow loading into the trap[111].

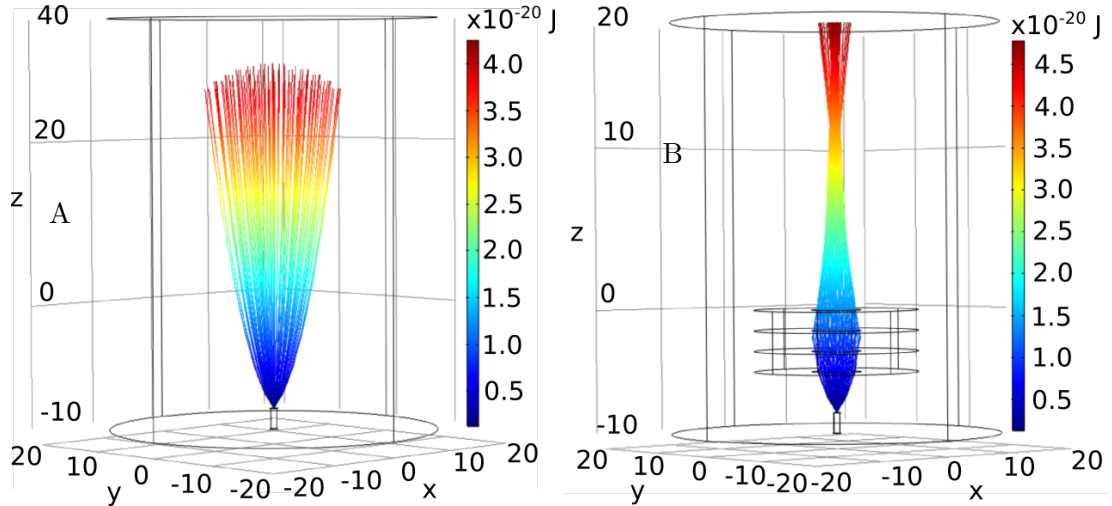


FIGURE 6.2: Path trace of unfocused (A) and magnetically focused (B) charged particles leaving a surface. $q=100e$ and the particles are assumed to have a mass of 10^{-19} kg. The coil is able to focus particles a distance of 40 mm from the ejection surface with a total velocity of 0.12 m/s and an ejection angle of 45° . This is only possible with high currents in very thin wires so it may not be useful on its own.

An example is shown in Fig.(6.2.B) with Fig.(6.2.A) showing the beam without any focusing. A beam of 10^{-19} kg particles can be focused 40 mm from the ejection surface with a starting velocity of 0.12 m/s. The parameters used are given in Tab.(6.1) which shows that a large current had to be used relative to the wire diameter, so melting could be an issue. Also most particles ejected from the piezo had a velocity of 0.4 m/s so a lot of the particle won't be focused with this method. Of course if the particles are charged anyway then it is possible to manipulate them with electric fields as already shown in Chap.(3).

Parameter	Value
Particle mass	10^{-19} kg
Total velocity	0.12 m/s
Charge	100 elementary charges
Release angle	45°
Coil current	1 A
No. Turns	5000
Wire Diameter	$1\mu\text{m}$
Coil outer radius	10 mm
Coil inter radius	3 mm
Coil length	2.5 mm
Wire material	Copper
Conductivity	6×10^7 S/m

TABLE 6.1: Simulation parameters used to produce Fig.(6.2). The diameter of the wire is quite small for this level of current so the system would have to be pulsed at the very least. Even with this high current it was only possible to focus particles with a total velocity of 0.12 m/s, meaning a lot of particles would be lost.

6.3 Electrical focusing

There are a number of ways to focus and manipulate a beam of charged particles using electric fields. Electron guns use a pair of electrodes, a hot cathode to emit electrons and an anode to accelerate the particles towards it[112]. There is a third surface called a Wehnelt cylinder near the hot cathode that has a negative bias and suppresses the emission of electrons apart from a small controlled area. This allows the source to be point like while the Wehnelt cylinder may also focus the electrons after emission. This design is not appropriate here as it would involve accelerating the charged particles further when it would be more ideal to slow them as they neared the trap. Another idea is a einzel lens or a uni-potential lens which focuses the charged particles without changing their energy[113]. This chapter will cover a dynamic variant of this where the potential is only applied once the particles are within the focusing cylinder. This can be done by applying a time delayed pulse as shown in Fig.(6.3.B) with a switch on at $4\mu\text{s}$ after release and a switch off at $8\mu\text{s}$. This method would be able to collimate even the high velocity particles and allow for a tighter focus of the slower particles[114]. Collimation of 10^{-20} kg particles travelling at 1000 m/s is shown in Fig.(6.3.A) although some particles are still lost due to the variance in particle velocity. There is some increase in the particle energy but with control this can be minimised. The parameters for the simulation are given in Tab.(6.2).

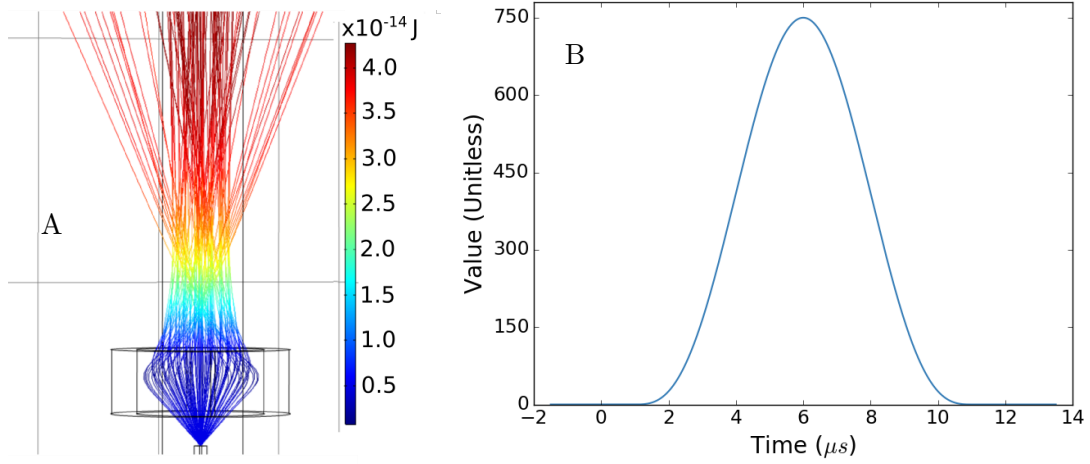


FIGURE 6.3: **A:** Path trace of charged particles being collimated using a pulsed 750 V electrode ring. The particles are released with a velocity of 1000 m/s and a mass of 10^{-20} kg. **B:** Pulse shape formed of a switch on time of $4 \mu\text{s}$ and a switch off time at $8 \mu\text{s}$. That this is able to collimation particles travelling at such high speeds show promise as a focusing method.

Parameter	Value
Particle mass	10^{-20} kg
Total velocity	1000 m/s
Charge	100q
Release angle	45°
Peak voltage	750 V
cut on	$4 \mu\text{s}$
cut off	$8 \mu\text{s}$
ring outer radius	7 mm
Coil inter radius	5 mm
Coil length	5 mm
Wire material	Copper
Conductivity	6×10^7 S/m

TABLE 6.2: Simulation parameters used to produce Fig.(6.3). The particles are travelling very fast but the electric field is still able to collimate them. The mass is smaller than most of the particles that have been used in this thesis but it still holds promise as a focusing method for slower particles.

6.4 Conclusion

The difficulty with focusing neutral nanoparticles is that the interaction cross sections tend to be very low. It is already shown that Rayleigh scattering is small and it scales as $1/r^6$, although even if it wasn't it would be difficult to design a focusing method based on scattering alone. Using the gradient force as a focusing method would be much simpler and more effective but there is still a significant set back. In order for the beam waist to enclose enough particles to make a difference the laser power needs to be very high. For example to focus all the particles in a $100 \mu\text{m}$ waist travelling with a

maximum horizontal velocity of 0.4 m/s a laser power of 5000 W is needed. This is not only difficult to produce but would also likely damage the tip of the ultrasonic horn.

The rest of this chapter therefore developed ideas for focusing charged particles. There are two main forces, magnetic and electrical. For magnetic focusing, a system was designed where the particles are released into a solenoid wire coil and the magnetic field generated by the coil could focus the particles travelling at 0.12 m/s. However, this involves using 1 A with in a 1 μm diameter wire which would likely melt the wire unless it could be pulsed fast enough. The other point is that although it could focus particles travelling at 0.12 m/s this is still less than the 0.4 m/s the released particles are travelling at.

The last idea was to use electric fields. It was already shown that the particle's motion can be readily manipulated using electric fields and so it was expected that this method would have the best result. The particles are released through the centre of a cylinder. 4 μs after the particles leave the surface a bias of 750 V is applied to the cylinder, pushing the particles away from the inner surface. After 8 μs this bias was turned off and most of the particles are now collimated. In the simulation, particles at travelling at 1000 m/s with a mass of 10^{-20} kg could be focused, giving promise that this method could be used for the particles released from both the ultrasonic tip and ablation.

Chapter 7

Conclusion

7.1 Summary

7.1.1 Force sensing

This thesis has demonstrated sensitivity down to $1.3 \times 10^{-21} \text{ N}/\sqrt{\text{Hz}}$ and, as shown in Sec.(3.1), with modifications the system should have a sensitivity of $\approx 10^{-24} \text{ N}/\sqrt{\text{Hz}}$. With this sensitivity it was possible to detect the changes in the particle's motion from both AC and DC electric fields. DC forces turned out to be difficult to measure as there was a lot of slow time scale drift in the detection system. Even so forces as low as 10^{-16} N were detected with integration times of just 10 seconds. Non-restorative forces like an electrostatic field cause the particle's average position to shift based on the polarity of the field and the charge on the nanoparticle. If the electric field is high enough, $2 \times 10^3 \text{ V/m}$, the frequency was seen to shift from its zero field value with a small skew deformation. The origin of this shift and skew is unclear. In this work the origin was taken to be due to the summing of the electric field of the laser and the applied field. This resulted in Eq.(3.37) for the PSD, which has the correct dependence on voltage for the frequency shift and is a fairly simple mathematical model. However, it failed to give reasonable values for the particle's charge, some times as high at $10^6 e$, and could not account for the skewness seen. The skewness could be added in mathematically but this adds very little physics and the data was too noisy to determine the relationship empirically. There are currently two other ideas being explored. The first is that the change in the particle's average position moves the particle far enough up one side of the trapping potential for the trap to now be non-symmetric. This is the simplest but the relationship between the movement and the trapping field is unclear. The second is that the particle is moving between two states and it is the scattering between these that causes the deformation seen. This kind of system is often referred to as Fano-like

resonance as it is similar to the effect discovered by Ugo Fano[115]. This effect has been observed in other opto-mechanical systems but not in levitated optomechanics[116][117]. Further experiments may help to solve which of these is the true origin.

Applying an AC electric field resulted in the particle's motion being driven at the AC frequency. As the driving frequency approached the natural frequency of the oscillator the signal from the driven frequency increased, resulting in a signal-to-noise of 200:1, where noise refers to the undriven PSD. With this enhancement it would be possible to beat the sensitivity limit due to thermal noise and reach $\approx 10^{-22} N/\sqrt{Hz}$. By reducing the pressure to UHV, $< 10^{-9}$ mbar, high quality factors of 10^9 can be reached. With improvements, then the sensitivity may one day be able to reach the ZTHR limit of $\approx 10^{-24} N/\sqrt{Hz}$. There are other factors that might prevent reaching this though. From a technical stand point the thermal noise from the detector and the tracking on the PLL are likely to either be current limits or limiting factors in the near future. The PLL is likely the reason the pressure couldn't go as low in the work presented here as it has been in other published work from this group. Work is now underway with a new cryogenically cooled vacuum chamber and an FPGA which should help reduce the Q and improve particle control. Water cooling the detector might be sufficient as the photodiode its self has a minimum NEP of 0.7 pW/Hz giving a positional sensitivity of 1.8×10^{-24} m/Hz, significantly less than the displacement at SQL of 8.9 pm.

As the system is improved there are two other limits that may become an issue. The first is photon recoil, were the momentum given to the particle by scattered particles is enough to change its occupation number. This is most likely to only become an issue once the phonon occupation numbers reach $n \approx 20$. As the resulting heating rate scales with r^3 , where r is the radius of the particle, it should be possible to reduce this by using a smaller particle, e.g. $r = 25$ nm should avoid this problem all together. The next challenge could be shot noise, depending on the power being used to trap the particle. Currently the detection system has a collection efficiency of 1% meaning that 99% of the signal is lost before it can be converted into an output signal. At the SQL the output signal will have an amplitude of just $87 \pm 2 \times 10^{-9}$ V with the error given by shot noise. The error is low enough here that it shouldn't be a limiting factor, however, it is close enough to be a concern if other noise sources are also near at this level.

If these challenges can be overcome and the system can reach the SQL, then there are some very interesting experiments that could be carried out, which have been detailed in this thesis. The natural progression from electrical forces is magnetic forces and in Chap.(3.4) and experiment to detect the magnetic moment of the particle was discussed. This could be done by either having a static magnetic field with a gradient of 20 T/m applied across the particle's motion and switching the spins coherently with an RF pulse,

or by having the magnetic field itself switch. The second method would be simpler and could be achieved with the high magnetic fields generated by hard drive read heads. The first method is the more traditional style and so there is a lot more literature from which to draw information.

Another force that is of constant interest is gravity. The most practical method to detect the gravitational force between the particle and a test mass is to use a 1 kg test mass that is 1 cm away from a $\phi 174$ nm particle. The test mass should be oscillated so that the motion of the nanoparticle is modulated at that frequency. Ideally this modulation would be at the trap frequency but that may not be possible given the challenges of moving such a large mass at high frequencies however some oscillation should be possible using a piezo actuator. A movement of just $500\text{ }\mu\text{m}$ would modulate the force by 10% which should be detectable. This would result in a force of 10^{-25} N which would require an integration time of 3000 years with the current sensitivity. For the improved set up the force should be detectable with the normal 3 hours of integration. To measure the force between the nanoparticle and the earth the current setup would require an altitude change of 5.4 m with 3 hours of integration. With the improved set up the altitude change would only need to be 6.5 mm and at the ZTHR limit it could be as small as $24\text{ }\mu\text{m}$. The main challenge then will be moving the experiment in such a way that the vibrations of the chamber or small changes in alignment don't couple to the motion of the particle. For the alignment a fibre feed-through could be used and the vibrations require the mirror mount to be isolated.

7.1.2 Vacuum source

To reach 10^{-9} mbar reliably the chamber has to be devoid of out gassing materials such as water. This could be a problem as the current loading method involves the use of a particle-water solution dispersed into the chamber at atmosphere. There is a build up of both particle and water residue around the whole chamber that has to be removed at times just to reach 10^{-5} mbar. To prevent this other source ideas were developed. Chap.(4) discussed work done with an ablating source that generated trappable particles directly in the chamber. Due to limits of the Nd:YAG laser used a large number of the particles produced were too large to trap, however, as the size distribution is thermal there are still smaller particles available. An example of a particle trapped at atmosphere is shown in Fig(4.12) with a radius of 35 ± 3 nm. While promising there were still significant challenges with this method. First, the particles produced are likely travelling very fast, compared to trapping frequency. This could be solved with the FPGA and fast position tracking but there is a larger issue. The energies involved to generate the particles are very large and are easily able to damage the measurement equipment.

Given the speed of the particles it is difficult to protect the detector and still have it be in a functional state for the cooling.

Another idea developed was to use an ultrasonic piezo to release dry particles from a prepared surface. This had the advantage that the particle's size range could be known before hand and also the source could be very close to the trap site. To test this idea an ultrasonic horn was developed that could be attached to a 40 kHz transducer. This focused the energy from the transducer down to a surface of just 3 mm in diameter. The surface was diamond turned to improve surface finish and the particles were loaded using a rapid heating method to minimise clusters. This method showed significant particle release but nothing could be trapped. On the assumption that the particles were too large steps towards a MHz source were taken which resulted in the first detection of a particle from an ultrasonic source at the trap site. The signal didn't last long and it is possible that it is the peizo driving the air that caused it to drop. There was insufficient data to produce a PSD but this still holds promise as a source once a transducer and even a horn have been designed.

7.2 Future work

Sensitivity: It has been mentioned repeatedly the need to move to the cryogenically cooled chamber and reduce the pressure down to 10^{-9} mbar. There is a strong indication that this will allow the system to approach the ground state and improve the force sensitivity. To that end the current PLL needs improving and ideally switching to an FGPA system.

Forces: The next action should be to measure the gravitational constant as this can be done without tampering with the rest of the set up. The biggest challenge there is making sure the vibrations of the driving piezo actuator does not interfere with the detection arm. There are some other forces that the system might be able to measure if it can reach ground state. It is unlikely that it will ever have the sensitivity to measure gravitational waves but other exotic gravitational effects might be measurable[118][119].

Vacuum source: For the source, a MHz horn needs to be designed. This could be coupled with a second trap with a larger waist, increasing trapping area. Electrical focusing could also be employed if the charge does not affect sensitivity. So long as the chamber and all components are earth during force measurements this should be possible.

Appendix A

Derivation of trapping force

The trapping force is given by,

$$F(r, z) = \frac{8Pa^3}{c} \frac{n^2 - 1}{n^2 + 2} \nabla \left(\frac{1}{w(z)^2} e^{\frac{-2r^2}{w(z)^2}} \right), \quad (\text{A.1})$$

In cylindrical coordinates $\nabla = \hat{r} \frac{\partial}{\partial r} + \hat{z} \frac{\partial}{\partial z}$ simplicity let β equal the leading constant. The force component in the \hat{r} direction is,

$$\begin{aligned} \mathbf{r} &= \beta \frac{\partial}{\partial r} e^{\frac{-2r^2}{w(z)^2}} \\ &= \beta \frac{-4r}{w(z)^2} e^{\frac{-2r^2}{w(z)^2}} \end{aligned} \quad (\text{A.2})$$

The longitudinal direction is,

$$\begin{aligned} \mathbf{z} &= \beta \frac{\partial}{\partial r} \left(\frac{1}{w(z)^2} e^{\frac{-2r^2}{w(z)^2}} \right) \\ &= \beta \frac{\partial}{\partial r} \left(\frac{1}{w(z)^2} \right) e^{\frac{-2r^2}{w(z)^2}} + \frac{\partial}{\partial r} \left(e^{\frac{-2r^2}{w(z)^2}} \right) \frac{\beta}{w(z)^2}. \end{aligned} \quad (\text{A.3})$$

The differential in the first term becomes,

$$\begin{aligned}
\frac{\partial}{\partial r} \left(\frac{1}{w(z)^2} \right) &= \frac{\partial}{\partial r} \left(\frac{1}{w_0^2} \frac{1}{1 + (z/z_R)^2} \right) \\
&= \frac{1}{w_0^2} \frac{\partial}{\partial u} \left(\frac{1}{u} \right) \frac{\partial u}{\partial z} \\
&= \frac{1}{w_0^2} \left(-\frac{1}{u^2} \right) \frac{2z}{z_R^2} \\
&= -\frac{2zw_0^2}{z_R^2 w(z)^4},
\end{aligned} \tag{A.4}$$

where $u = (1 + (z/z_R)^2)$ so $\frac{\partial u}{\partial z} = \frac{2z}{z_R^2}$ and Eq.(2.9) has been used to get the relation between beam waist and z . The second differential in Eq.(A.3 is,

$$\begin{aligned}
\frac{\partial}{\partial r} \left(e^{\frac{-2r^2}{w(z)^2}} \right) &= -2r^2 \frac{\partial}{\partial r} \left(\frac{1}{w(z)^2} \right) e^{\frac{-2r^2}{w(z)^2}} \\
&= \frac{-4r^2 z w_0^2}{e} \frac{\frac{-2r^2}{w(z)^2}}{e}
\end{aligned} \tag{A.5}$$

Bring this all together gives the total force as,

$$\mathbf{F}(r, z) = 2\beta e^{\frac{-2r^2}{w(z)^2}} \left(\hat{r} \frac{2r}{w(z)^4} + \hat{z} \left(\frac{w_0^2}{w(z)^4} - \frac{2r^2 w_0^2}{w(z)^6} \right) \right) \tag{A.6}$$

Appendix B

Technical drawings

B.1 Parabolic mirror

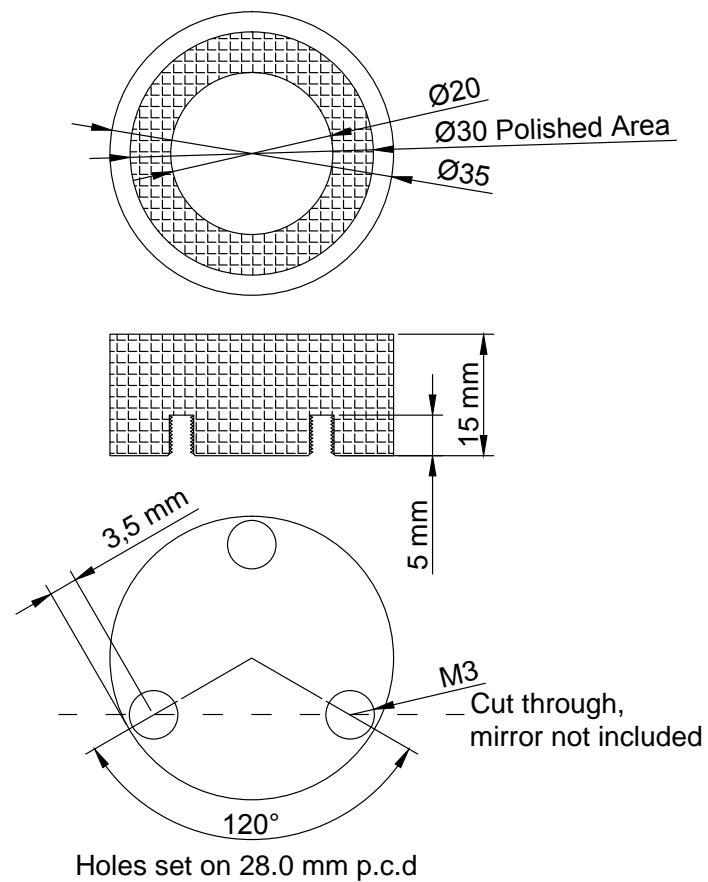


FIGURE B.1: The Autocad drawing sent to the manufacturer to produce the parabolic mirrors.

B.2 Needle

Stainless Steel 304 High voltage electrode
David Hempston, Rm3038, 8th Oct 2016

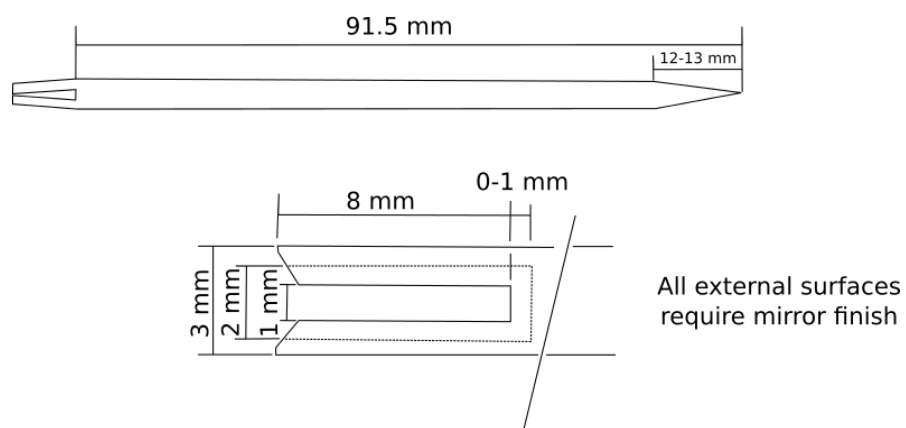


FIGURE B.2: Design drawing used to manufacture the needle using in the electric fields experiments.

Appendix C

Driven Harmonic Oscillator

Take a mass on a spring that is free to move horizontally. For a displacement x there will be a restoring force $-kx$, where k is the spring constant, and a damping force $\Gamma\dot{x}$, where Γ is the damping rate. If the other end of the spring is also attached to a piston that can also move then equation of motion is,

$$\ddot{x} + \Gamma\dot{x} + \omega_0^2 x = \omega_0^2 X, \quad (\text{C.1})$$

where ω_0 is the natural frequency and X is the piston displacement. Let the pistons motion be sinusoidal so that $X(t) = X_0 \cos(\omega t)$

$$\ddot{x} + \Gamma\dot{x} + \omega_0^2 x = \omega_0^2 X_0 \cos(\omega t), \quad (\text{C.2})$$

In the steady state solution the mass will have the same oscillation frequency as the piston, in which the frictional energy loss per cycle is exactly matched by the work done by the piston per cycle. This suggests a solution to $x(t)$ of the form,

$$x(t) = x_0 \cos(\omega t - \varphi), \quad (\text{C.3})$$

where x_0 is the amplitude of the driven oscillation, and φ is the phase lag of this oscillation (with respect to the phase of the piston oscillation). Using this as the form, the velocity and acceleration are given by,

$$\dot{x}(t) = -\omega x_0 \sin(\omega t - \varphi) \quad (\text{C.4})$$

$$\ddot{x}(t) = -\omega^2 x_0 \cos(\omega t - \varphi) \quad (\text{C.5})$$

Eq.(C.1) becomes,

$$(\omega_0^2 - \omega^2)x_0 \cos(\omega t - \varphi) - \Gamma\omega x_0 \sin(\omega t - \varphi) = \omega_0^2 X_0 \cos(\omega t). \quad (\text{C.6})$$

This can be expanded using the relations,

$$\cos(\omega t - \varphi) \equiv \cos(\omega t) \cos(\varphi) + \sin(\omega t) \sin(\varphi) \quad (\text{C.7})$$

$$\sin(\omega t - \varphi) \equiv \sin(\omega t) \cos(\varphi) - \cos(\omega t) \sin(\varphi) \quad (\text{C.8})$$

to obtain,

$$[x_0(\omega_0^2 - \omega^2) \cos(\varphi) + x_0\Gamma\omega \sin(\varphi) - \omega_0^2 X_0] \cos(\omega t) \quad (\text{C.9})$$

$$+ x_0 [(\omega_0^2 - \omega^2) \sin(\varphi) - \Gamma\omega \cos(\varphi)] \sin(\omega t) = 0 \quad (\text{C.10})$$

The only way in which the preceding equation can be satisfied at all times is if the coefficients of $\cos(\omega t)$ and $\sin(\omega t)$ separately equate to zero. In other words, if

$$x_0(\omega_0^2 - \omega^2) \cos(\varphi) + x_0\Gamma\omega \sin(\varphi) - \omega_0^2 X_0 = 0 \quad (\text{C.11})$$

$$(\omega_0^2 - \omega^2) \sin(\varphi) - \Gamma\omega \cos(\varphi) = 0 \quad (\text{C.12})$$

These two expressions can be combined to give Eq.(C.13) for the position of the mass and Eq.(C.14) for the phase.

$$x_0 = \frac{\omega_0^2 X_0}{[(\omega_0^2 - \omega^2)^2 + \Gamma^2 \omega^2]^{1/2}} \quad (\text{C.13})$$

$$\tan(\varphi) = \frac{\Gamma\omega}{\omega_0^2 - \omega^2} \quad (\text{C.14})$$

Appendix D

Quantum harmonic oscillator

For a quantum harmonic oscillator (QHO) the Hamiltonian is,

$$\hat{H} = \frac{m\omega_0^2}{2}\hat{x}^2 + \frac{\hat{p}^2}{2m} \quad (\text{D.1})$$

where \hat{x} is the position operator and \hat{p} is the momentum operator. To simplify some of the later maths let,

$$\hat{X} = \hat{x}\sqrt{\frac{m\omega_0}{\hbar}} \quad (\text{D.2})$$

$$\hat{P} = \frac{\hat{p}}{\sqrt{m\hbar\omega_0}}. \quad (\text{D.3})$$

and then the following pair of operators can be defined,

$$\hat{a} = \frac{1}{\sqrt{2}}(\hat{X} + i\hat{P}) \quad (\text{D.4})$$

$$\hat{a}^\dagger = \frac{1}{\sqrt{2}}(\hat{X} - i\hat{P}), \quad (\text{D.5})$$

so that the Hamiltonian then becomes,

$$\hat{H} = \hbar\omega_0(\hat{a}^\dagger\hat{a} + 1/2). \quad (\text{D.6})$$

The commutator for \hat{a} and \hat{a}^\dagger gives,

$$\begin{aligned}
[\hat{a}, \hat{a}^\dagger] &= \hat{a}\hat{a}^\dagger - \hat{a}^\dagger\hat{a} \\
&= \frac{1}{2} \left((\hat{X} + i\hat{P})(\hat{X} - i\hat{P}) - (\hat{X} - i\hat{P})(\hat{X} + i\hat{P}) \right) \\
&= \frac{1}{2} \left(\hat{X}^2 - i\hat{X}\hat{P} + i\hat{P}\hat{X} + \hat{P}^2 - \hat{X}^2 - i\hat{X}\hat{P} + i\hat{P}\hat{X} - \hat{P}^2 \right) \\
&= -i(\hat{X}\hat{P} - \hat{P}\hat{X}) \\
&= \frac{-i}{\hbar} [\hat{x}, \hat{p}] \\
&= 1.
\end{aligned} \tag{D.7}$$

When the Hamiltonian operates on some wave function, $|\phi\rangle$, it gives an eigenvalue, E , which is the energy of that state and the original wave function, i.e. $\hat{H}|\phi\rangle = E|\phi\rangle$. To see how \hat{a}^\dagger changes the state lets apply it to a general wave function and then apply the Hamiltonian.

$$\begin{aligned}
\hat{H}\hat{a}^\dagger|\phi\rangle &= \hbar\omega_0(\hat{a}^\dagger\hat{a} + 1/2)\hat{a}^\dagger|\phi\rangle \\
&= \hbar\omega_0(\hat{a}^\dagger\hat{a}\hat{a}^\dagger + \hat{a}^\dagger/2)|\phi\rangle \\
&= \hat{a}^\dagger\hbar\omega_0(\hat{a}\hat{a}^\dagger + 1/2)|\phi\rangle \\
&= \hat{a}^\dagger\hbar\omega_0(\hat{a}^\dagger\hat{a} + 1 + 1/2)|\phi\rangle \\
&= \hat{a}^\dagger\hbar\omega_0(\hat{a}^\dagger\hat{a} + 1/2)|\phi\rangle + \hbar\omega_0\hat{a}^\dagger|\phi\rangle \\
&= \hat{a}^\dagger\hat{H}|\phi\rangle + \hbar\omega_0\hat{a}^\dagger|\phi\rangle \\
&= (E + \hbar\omega_0)\hat{a}^\dagger|\phi\rangle,
\end{aligned} \tag{D.8}$$

where $\hat{a}^\dagger|\phi\rangle$ is a new wave function with an energy of $E + \hbar\omega_0$. This is why \hat{a}^\dagger is known as the raising operator, it raises the energy state by one unit of $\hbar\omega_0$. Similarly, \hat{a} is the lowering operator that reduces the energy by one level, until the ground state where $\hat{a}|\phi\rangle = 0$.

Bibliography

- [1] A. Ashkin and J. M. Dziedzic, “[Feedback stabilization of optically levitated particles](#),” *Applied Physics Letters*, vol. 30, no. 4, pp. 202–204, 1977.
- [2] J. Vovrosh, M. Rashid, D. Hempston, J. Bateman, M. Paternostro, and H. Ulbricht, “[Parametric feedback cooling of levitated optomechanics in a parabolic mirror trap](#),” *Journal of the Optical Society of America B*, vol. 34, 2017.
- [3] L. Hung and C. Nguyen, *High-Q Low-Impedance MEMS Resonators*. PhD thesis, EECS Department, University of California, Berkeley, Dec 2012.
- [4] A. Sawadsky, H. Kaufer, R. M. Nia, S. P. Tarabrin, F. Y. Khalili, K. Hammerer, and R. Schnabel, “[Observation of Generalized Optomechanical Coupling and Cooling on Cavity Resonance](#),” *Phys. Rev. Lett.*, vol. 114, p. 043601, Jan 2015.
- [5] V. Jain, J. Gieseler, C. Moritz, C. Dellago, R. Quidant, and L. Novotny, “[Direct Measurement of Photon Recoil from a Levitated Nanoparticle](#),” *Phys. Rev. Lett.*, vol. 116, p. 243601, Jun 2016.
- [6] J. Gieseler, B. Deutsch, R. Quidant, and L. Novotny, “[Subkelvin Parametric Feedback Cooling of a Laser-Trapped Nanoparticle](#),” *Phys. Rev. Lett.*, vol. 109, p. 103603, Sep 2012.
- [7] J. Moser, J. Guttinger, A. Eichler, M. J. Esplandiu, D. E. Liu, M. I. Dykman, and A. Bachtold, “[Ultrasensitive force detection with a nanotube mechanical resonator](#),” *Nat. Nano*, vol. 8, 2013.
- [8] R. P. Middlemiss, A. Samarelli, D. J. Paul, J. Hough, S. Rowan, and G. D. Hammond, “[Measurement of the Earth tides with a MEMS gravimeter](#),” *Nature*, vol. 631, 2016.
- [9] M. Arndt and K. Hornberger, “[Testing the limits of quantum mechanical superpositions](#),” *Nat. Phys*, vol. 10, pp. 271–277, 2014.

- [10] G. Ranjit, D. P. Atherton, J. H. Stutz, M. Cunningham, and A. A. Geraci, “[Attonewton force detection using microspheres in a dual-beam optical trap in high vacuum](#),” *Phys. Rev. A*, vol. 91, p. 051805, May 2015.
- [11] A. Arvanitaki and A. A. Geraci, “[Detecting High-Frequency Gravitational Waves with Optically Levitated Sensors](#),” *Phys. Rev. Lett.*, vol. 110, p. 071105, Feb 2013.
- [12] I. A. Martinez, E. Roldan, L. Dinis, D. Petrov, J. M. Parrondo, and R. A. Rica, “[Brownian Carnot engine](#),” *Nat. Phys*, vol. 12, pp. 67–70, 2016.
- [13] J. Bateman, S. Nimmrichter, K. Hornberger, and H. Ulbricht, “[Near-field interferometry of a free-falling nanoparticle from a point-like source](#),” *Nat. Commun.*, vol. 5, 2014.
- [14] M. Poggio, C. L. Degen, H. J. Mamin, and D. Rugar, “[Feedback Cooling of a Cantilever’s Fundamental Mode below 5 mK](#),” *Phys. Rev. Lett.*, vol. 99, p. 017201, Jul 2007.
- [15] S. Vashist, “[A Review of microcantilevers for sensing applications](#),” *AZoNano*, vol. 3, pp. 1–15, 01 2007.
- [16] H. J. Mamin and D. Rugar, “[Sub-attonewton force detection at millikelvin temperatures](#),” *Applied Physics Letters*, vol. 79, no. 20, pp. 3358–3360, 2001.
- [17] D. Rugar, R. Budakian, H. J. Mamin, and B. W. Chui, “[Single spin detection by magnetic resonance force microscopy](#),” *Nature*, vol. 430, pp. 329–332, Jul 2004.
- [18] R. Pooser and B. Lawrie, “[Ultrasensitive measurement of microcantilever displacement below the shot-noise limit](#),” *Optica*, vol. 2, pp. 393–399, May 2015.
- [19] Y. Tao, J. M. Boss, B. A. Moores, and C. L. Degen, “[Single-crystal diamond nanomechanical resonators with quality factors exceeding one million](#),” *Nat. Comms.*, vol. 5, Apr 2014.
- [20] T. Miao, D. Xiao, Q. Li, Z. Hou, and X. Wu, “[A 4 mm² Double Differential Torsional MEMS Accelerometer Based on a Double-Beam Configuration](#),” *Sensors*, vol. 17, p. 2264, Oct 2017.
- [21] Z. Miao, H. Shi, and Y. Zhang, “Real-time analysis for stochastic errors of mems gyro,” in *AOPC 2017: Space Optics and Earth Imaging and Space Navigation*, vol. 10463, International Society for Optics and Photonics.
- [22] T.-V. Nguyen, H. Takahashi, and I. Shimoyama, “Mems-based pressure sensor with a superoleophobic membrane for measuring droplet vibration,” in *Solid-State Sensors, Actuators and Microsystems (TRANSDUCERS), 2017 19th International Conference on*, pp. 1152–1155, IEEE, 2017.

- [23] H. Zhang, J. K. Jackson, and M. Chiao, “Microfabricated drug delivery devices: Design, fabrication, and applications,” *Advanced Functional Materials*, 2017.
- [24] H. B. Chan, V. A. Aksyuk, R. N. Kleiman, D. J. Bishop, and F. Capasso, “[Quantum Mechanical Actuation of Microelectromechanical Systems by the Casimir Force](#),” *Science*, vol. 291, no. 5510, pp. 1941–1944, 2001.
- [25] M. Kretzschmar, “[Particle motion in a Penning trap](#),” *European Journal of Physics*, vol. 12, no. 5, p. 240, 1991.
- [26] R. E. March, “[Quadrupole ion traps](#),” *Mass Spectrometry Reviews*, vol. 28, no. 6, 2009.
- [27] W. Itano, J. Bergquist, J. Bollinger, and D. Wineland, “[Cooling methods in ion traps](#),” *Physica Scripta*, vol. 1995, no. T59, p. 106, 1995.
- [28] S. Knünz, M. Herrmann, V. Batteiger, G. Saathoff, T. W. Hänsch, K. Vahala, and T. Udem, “[Injection Locking of a Trapped-Ion Phonon Laser](#),” *Phys. Rev. Lett.*, vol. 105, p. 013004, Jul 2010.
- [29] M. J. Biercuk, H. Uys, J. Britton, A. VanDevender, and J. Bollinger, “[Ultrasensitive detection of force and displacement using trapped ions](#),” *Nat Nano*, vol. 5, pp. 646–650, Sep 2010.
- [30] R. Maiwald, D. Leibfried, J. Britton, J. Bergquist, G. Leuchs, and D. Wineland, “[Stylus ion trap for enhanced access and sensing](#),” *Nat Phys*, vol. 5, pp. 551–554, Aug 2009.
- [31] B. D. Cuthbertson, M. E. Tobar, E. N. Ivanov, and D. G. Blair, “[Parametric backaction effects in a highQ cyrogenic sapphire transducer](#),” *Review of Scientific Instruments*, vol. 67, no. 7, pp. 2435–2442, 1996.
- [32] M. Aspelmeyer, T. Kippenberg, and F. Marquardt, “[Cavity optomechanics](#),” *Rev. Mod. Phys.*, vol. 86, pp. 1391–1452, Dec 2014.
- [33] A. G. Krause, M. Winger, T. D. Blasius, Q. Lin, and O. Painter, “[A high-resolution microchip optomechanical accelerometer](#),” *Nat Photon*, vol. 6, pp. 768–772, Nov 2012.
- [34] J. Teufel, T. Donner, M. A. Castellanos-Beltran, J. W. Harlow, and W. K. Lehnert, “[Nanomechanical motion measured with an imprecision below that at the standard quantum limit](#),” *Nat Nano*, vol. 4, pp. 820–823, Dec 2009.
- [35] H. Miao, K. Srinivasan, M. T. Rakher, M. Davanco, and V. Aksyuk, “[Cavity optomechanical sensors](#),” *2011 16th International Solid-State Sensors, Actuators and Microsystems Conference*, Jun 2011.

- [36] S. Forstner, S. Prams, J. Knittel, E. D. van Ooijen, J. D. Swaim, G. I. Harris, A. Szorkovszky, W. P. Bowen, and H. Rubinsztein-Dunlop, “[Cavity Optomechanical Magnetometer](#),” *Phys. Rev. Lett.*, vol. 108, p. 120801, Mar 2012.
- [37] A. T. Young, “[Rayleigh scattering](#),” *Appl. Opt.*, vol. 20, pp. 533–535, Feb 1981.
- [38] B. Saleh and M. Teich, “[The Gaussian Beam 3.1](#),” in *Fundamentals of Photonics*, vol. 5, ch. 3, pp. 80–107, John Wiley & Sons, Inc, 1991.
- [39] B. Richards and E. Wolf, “[Electromagnetic Diffraction in Optical Systems. II. Structure of the Image Field in an Aplanatic System](#),” *Proc. R. Soc. Lond. A*, vol. 253, no. 1274, pp. 358–379, 1959.
- [40] J. J. M. Braat and P. F. Greve, “[Aplanatic optical system containing two aspheric surfaces](#),” *Appl. Opt.*, vol. 18, pp. 2187–2191, Jul 1979.
- [41] R. Fitzpatrick, “The Clausius-Mossotti relation,” *The University of Texas at Austin*, 2002.
- [42] P. Török, P. Varga, Z. Laczik, and G. R. Booker, “[Electromagnetic diffraction of light focused through a planar interface between materials of mismatched refractive indices: an integral representation](#),” *J. Opt. Soc. Am. A*, vol. 12, pp. 325–332, Feb 1995.
- [43] T. Godazgar, R. Shokri, and S. Reihani, “[Potential mapping of optical tweezers](#),” *Opt. Lett.*, vol. 36, pp. 3284–3286, Aug 2011.
- [44] R. Grimm, M. Weidemuller, and Y. B. Ovchinnikov, “[Optical Dipole Traps for Neutral Atoms](#),” *Advances In Atomic, Molecular, and Optical Physics*, vol. 42, no. Supplement C, pp. 95 – 170, 2000.
- [45] V. N. Mahajan, “[Strehl ratio for primary aberrations in terms of their aberration variance](#),” *J. Opt. Soc. Am.*, vol. 73, pp. 860–861, Jun 1983.
- [46] R. Kubo, “[The fluctuation-dissipation theorem](#),” *Reports on Progress in Physics*, vol. 29, no. 1, p. 255, 1966.
- [47] J. Weber, “[Fluctuation Dissipation Theorem](#),” *Phys. Rev.*, vol. 101, pp. 1620–1626, Mar 1956.
- [48] S. A. Beresnev, V. G. Chernyak, and G. A. Fomyagin, “Motion of a spherical particle in a rarefied gas. Part 2. Drag and thermal polarization,” *Journal of Fluid Mechanics*, vol. 219, pp. 405–421, 1990.
- [49] J. L. Hogg, “Viscosity of air,” *Proceedings of the American Academy of Arts and Sciences*, vol. 40, no. 18, pp. 611–626, 1905.

- [50] N. F. Ramsey, “[Thermodynamics and Statistical Mechanics at Negative Absolute Temperatures](#),” *Phys. Rev.*, vol. 103, pp. 20–28, Jul 1956.
- [51] Z. Cao, Y. Wang, and H. Luo, “[Inhomogeneity of the phase space of the damped harmonic oscillator under Lévy noise](#),” *Phys. Rev. E*, vol. 85, p. 042101, Apr 2012.
- [52] P. R. Saulson, “[Thermal noise in mechanical experiments](#),” *Phys. Rev. D*, vol. 42, pp. 2437–2445, Oct 1990.
- [53] C. L. Degen, F. Reinhard, and P. Cappellaro, “[Quantum sensing](#),” *Rev. Mod. Phys.*, vol. 89, p. 035002, Jul 2017.
- [54] C. Caves, S. Nakajima, Y. Murayama, and A. Tonomura, “Quantum nondemolition measurement,” in *Foundations of Quantum Mechanics in the Light of New Technology*, ch. 1, p. 101, World Scientific, 1997.
- [55] J. Millen, P. Z. G. Fonseca, T. Mavrogordatos, T. S. Monteiro, and P. F. Barker, “[Cavity Cooling a Single Charged Levitated Nanosphere](#),” *Phys. Rev. Lett.*, vol. 114, p. 123602, Mar 2015.
- [56] W. Huang and Y. Chen, “[Generalized skew-Cauchy distribution](#),” *Statistics and Probability Letters*, vol. 77, no. 11, pp. 1137 – 1147, 2007.
- [57] D. M. Riffe, “[Classical Fano oscillator](#),” *Phys. Rev. B*, vol. 84, p. 064308, Aug 2011.
- [58] [Richter, K. and OBrien, D. P.](#), “Terrestrial planet formation,” *Proceedings of the National Academy of Sciences*, vol. 108, no. 48, pp. 19165–19170, 2011.
- [59] S. Chandrasekhar, [An Introduction to the Study of Stellar Structure \(Dover Books on Astronomy\)](#). Dover Publications, 2010.
- [60] A. Einstein, “[Die Grundlage der allgemeinen Relativitätstheorie](#),” *Annalen der Physik*, vol. 354, pp. 769–822, 1916.
- [61] C. M. Will, “[The Confrontation between General Relativity and Experiment](#),” *Living Reviews in Relativity*, vol. 17, no. 1, p. 4, 2014.
- [62] B. P. Abbott et al., “[Observation of Gravitational Waves from a Binary Black Hole Merger](#),” *Phys. Rev. Lett.*, vol. 116, p. 061102, Feb 2016.
- [63] D. V. Martynov et al., “[Sensitivity of the Advanced LIGO detectors at the beginning of gravitational wave astronomy](#),” *Phys. Rev. D*, vol. 93, p. 112004, Jun 2016.

- [64] T. Quinn, C. Parks, H. and Speake, and R. Davis, “[Improved Determination of \$G\$ Using Two Methods](#),” *Phys. Rev. Lett.*, vol. 111, p. 101102, Sep 2013.
- [65] J. D. Anderson, G. Schubert, V. Trimble, and M. R. Feldman, “[Measurements of Newton’s gravitational constant and the length of day](#),” *EPL (Europhysics Letters)*, vol. 110, no. 1, p. 10002, 2015.
- [66] J. H. Gundlach and S. M. Merkowitz, “[Measurement of Newton’s Constant Using a Torsion Balance with Angular Acceleration Feedback](#),” *Phys. Rev. Lett.*, vol. 85, pp. 2869–2872, Oct 2000.
- [67] “http://www.lesker.com/newweb/flanges/fittings_cf_crosses.cfm?pgid=cube.” Accessed: 2017-06-07.
- [68] G. Ferrand, G. Huber, M. Luong, and H. Desvaux, “[Nuclear spin noise in NMR revisited](#),” *The Journal of Chemical Physics*, vol. 143, no. 9, p. 094201, 2015.
- [69] T. M. Atkins, M. C. Cassidy, M. Lee, S. Ganguly, C. M. Marcus, and S. M. Kauzlarich, “[Synthesis of Long T1 Silicon Nanoparticles for Hyperpolarized \$^{29}\text{Si}\$ Magnetic Resonance Imaging](#),” *ACS Nano*, vol. 7, no. 2, pp. 1609–1617, 2013.
- [70] M. Poggio and C. L. Degen, “[Force-detected nuclear magnetic resonance: recent advances and future challenges](#),” *Nanotechnology*, vol. 21, no. 34, p. 342001, 2010.
- [71] T. H. Boyer, “[The force on a magnetic dipole](#),” *American Journal of Physics*, vol. 56, no. 8, pp. 688–692, 1988.
- [72] J. A. Sidles, “[Folded Stern-Gerlach experiment as a means for detecting nuclear magnetic resonance in individual nuclei](#),” *Phys. Rev. Lett.*, vol. 68, pp. 1124–1127, Feb 1992.
- [73] Y. Tao, A. Eichler, T. Holzherr, and C. L. Degen, “[Ultrasensitive mechanical detection of magnetic moment using a commercial disk drive write head](#),” *Nature Communications*, 2016.
- [74] W. Shinji and S. Susumu, “ [\$^{29}\text{Si}\$ Nuclear-Spin Decoherence Process Directly Observed by Multiple Spin-Echoes for Pure and Carrier-Less Silicon](#),” *Japanese Journal of Applied Physics*, vol. 42, no. 11B, p. L1350, 2003.
- [75] S. Werner, F. Arthur, and B. Ernst, “[Controlled growth of monodisperse silica spheres in the micron size range](#),” *Journal of Colloid and Interface Science*, vol. 26, no. 1, pp. 62 – 69, 1968.
- [76] G. H. Bogush, M. A. Tracy, and C. F. Zukoski, “[Preparation of monodisperse silica particles: Control of size and mass fraction](#),” *Journal of Non-Crystalline Solids*, vol. 104, no. 1, pp. 95 – 106, 1988.

- [77] V. de Castro, G. Benito, S. Hurst, C. Serna, M. Morales, and S. Veintemillas-Verdaguer, “[One step production of magnetic nanoparticle films by laser pyrolysis inside a chemical vapour deposition reactor](#),” *Thin Solid Films*, vol. 519, no. 22, pp. 7677–7682, 2011.
- [78] G. D., F. J., H. S., K. N., and A. M., “[Optical trapping and control of nanoparticles inside evacuated hollow core photonic crystal fibers](#),” *Appl. Phys. Lett.*, vol. 108, 2016.
- [79] P. Z. G. Fonseca, E. B. Aranas, J. Millen, T. S. Monteiro, and P. F. Barker, “[Non-linear Dynamics and Strong Cavity Cooling of Levitated Nanoparticles](#),” *Phys. Rev. Lett.*, vol. 117, p. 173602, Oct 2016.
- [80] H. Pantisar, H. Herfurth, S. Heinemann, P. Laakso, R. Penttila, Y. Liu, and G. Newaz, “LASER MICROVIA DRILLING AND ABLATION OF SILICON USING 355 NM PICO AND,” in *Laser Microprocessing Conference*, pp. 278–287, 2008.
- [81] J. Perrière, C. Boulmer-Leborgne, R. Benzerga, and S. Tricot, “[Nanoparticle formation by femtosecond laser ablation](#),” *Journal of Physics D: Applied Physics*, vol. 40, no. 22, pp. 7069–7076, 2007.
- [82] C. Y. Liu, X. L. Mao, R. Greif, and R. E. Russo, “[Time Resolved Shadowgraph Images of Silicon during Laser Ablation: Shockwaves and Particle Generation](#),” *Journal of Physics: Conference Series*, vol. 59, pp. 338–342, Apr. 2007.
- [83] M. Hashida, H. Mishima, S. Tokita, and S. Sakabe, “[Non-thermal ablation of expanded polytetrafluoroethylene with an intense femtosecond-pulse laser](#),” *Opt. Express*, vol. 17, pp. 13116–13121, Jul 2009.
- [84] S. Kuroda, S. Kaihara, Y. Fujii, T. Kinoshita, and M. Adachi, “[Modeling of particle generation in laser ablation plasma](#),” *Journal of Aerosol Science*, vol. 50, pp. 38–56, Aug. 2012.
- [85] D. M. Karnakis, M. Knowles, K. Alty, M. Schlaf, and H. Snelling, “[Comparison of glass processing using high-repetition femtosecond \(800 nm\) and UV \(255 nm\) nanosecond pulsed lasers](#),” *Proc. SPIE 5718, Microfluidics, BioMEMS, and Medical Microsystems III*, vol. 5718, pp. 216–227, 2005.
- [86] M. A. Green, “[Self-consistent optical parameters of intrinsic silicon at 300K including temperature coefficients](#),” *Solar Energy Materials and Solar Cells*, vol. 92, pp. 1305–1310, Nov. 2008.

- [87] P. Asenbaum, S. Kuhn, S. Nimmrichter, U. Sezer, and M. Arndt, “[Cavity cooling of free silicon nanoparticles in high vacuum.](#),” *Nature communications*, vol. 4, p. 2743, Jan. 2013.
- [88] A. Milling, P. Mulvaney, and I. Larson, “[Direct Measurement of Repulsive van der Waals Interactions Using an Atomic Force Microscope](#),” *Journal of Colloid and Interface Science*, vol. 180, no. 2, pp. 460 – 465, 1996.
- [89] L. Seung-woo and M. Wolfgang, “[Repulsive van der Waals Forces for Silica and Alumina](#),” *Journal of Colloid and Interface Science*, vol. 243, no. 2, pp. 365 – 369, 2001.
- [90] J. E. Jones, “[On the Determination of Molecular Fields. II. From the Equation of State of a Gas](#),” *Proceedings of the Royal Society of London A: Mathematical, Physical and Engineering Sciences*, vol. 106, no. 738, pp. 463–477, 1924.
- [91] H. C. Hamaker, “[The Londonvan der Waals attraction between spherical particles](#),” *Physica*, vol. 4, no. 10, pp. 1058 – 1072, 1937.
- [92] S. Alvo, S. Lambert, M. Gauthier, and S. Rgnier, “[A van der Waals Force-Based Adhesion Model for Micromanipulation](#),” *Journal of Adhesion Science and Technology*, vol. 24, no. 15-16, pp. 2415–2428, 2010.
- [93] P. Glaister, “[Intersecting Chords Theorem: 30 Years on](#),” *Mathematics in School*, vol. 36, no. 1, pp. 22–22, 2007.
- [94] J. N. Israelachvili, “[11 - Contrasts between Intermolecular, Interparticle, and Intersurface Forces](#),” in *Intermolecular and Surface Forces (Third Edition)* (J. N. Israelachvili, ed.), pp. 205 – 222, San Diego: Academic Press, third edition ed., 2011.
- [95] M. J. Winter, “[Size of silicon in several environments](#),” 2012.
- [96] A. A. Marino, R. O. Becker, and S. C. Soderholm, “[Origin of the piezoelectric effect in bone](#),” *Calcified Tissue Research*, vol. 8, no. 1, pp. 177–180, 1971.
- [97] K. Hye, K. Kunmo, L. Sung, P. Kang-Ho, and K. Jongdae, “[High Performance Piezoelectric Microspeakers and Thin Speaker Array System](#),” *ETRI Journal*, vol. 31, pp. 680–687, 2009.
- [98] M. Haq, S. Bhalla, and T. Naqvi, “[Fatigue Damage Assessment of RC Column using PZT Sensors](#),” *Procedia Engineering*, vol. 173, pp. 1223 – 1230, 2017.
- [99] S. Hirsch, S. Doerner, S. Schimpf, R. Lucklum, P. Hauptmann, and B. Schmidt, “[A new device with PZT ultrasonic transducers in MEMS technology](#),” *Journal of Physics: Conference Series*, vol. 34, no. 1, p. 475, 2006.

- [100] S. Chu, T. Chen, I. Tsai, and W. Water, “[Doping effects of Nb additives on the piezoelectric and dielectric properties of {PZT} ceramics and its application on {SAW} device](#),” *Sensors and Actuators A: Physical*, vol. 113, no. 2, pp. 198 – 203, 2004.
- [101] M. Kang, W. Jung, C. Kang, and S. Yoon, “[Recent Progress on PZT Based Piezoelectric Energy Harvesting Technologies](#),” *Actuators*, vol. 5, no. 1, 2016.
- [102] M. S. Vijaya, *Piezoelectric Materials and Devices: Applications in Engineering and Medical Sciences*. CRC Press, 2016.
- [103] S. D. Ravinder and V. Maurizio, *Robotic Tactile Sensing*, pp. 195–245. Springer Netherlands, 2013.
- [104] D. J. Griffiths, *Introduction to Electrodynamics (3rd Edition)*. Prentice Hall, 1999.
- [105] “Ieee standard on piezoelectricity,” *ANSI/IEEE Std 176-1987*, 1988.
- [106] C. Agbaraji and S. Raman, “[Basic observations in the flat lapping of aluminum and steels using standard abrasives](#),” *The International Journal of Advanced Manufacturing Technology*, vol. 44, no. 3, pp. 293–305, 2009.
- [107] “<https://www.piceramic.com/en/products/piezoceramic-components/rings/>.” Accessed: 2017-06-08.
- [108] “<http://piezomat.org/materials/270>.” Accessed: 2017-06-08.
- [109] P. Wolfgang, “[Electromagnetic traps for charged and neutral particles](#),” *Rev. Mod. Phys.*, vol. 62, pp. 531–540, Jul 1990.
- [110] J. T. Mendel, “[Magnetic Focusing of Electron Beams](#),” *Proceedings of the IRE*, vol. 43, pp. 327–331, March 1955.
- [111] V. Meerakker, Y. T. Sebastiaan, P. Smeets, N. Vanhaecke, R. T. Jongma, and G. Meijer, “[Deceleration and Electrostatic Trapping of OH Radicals](#),” *Phys. Rev. Lett.*, vol. 94, p. 023004, Jan 2005.
- [112] M. Hoseinzade, M. Nijatie, and A. Sadighzadeh, “[Numerical simulation and design of a thermionic electron gun](#),” *Chinese Physics C*, vol. 40, no. 5, p. 057003, 2016.
- [113] D. W. O. Heddle, *Electrostatic lens systems*. Bristol Philadelphia: Institute of Physics Pub, 2000.
- [114] A. A. Trubitsyn, E. Y. Grachev, and D. Y. Tarabrin, “[Focusing of charged particles by electric field lenses with a pulsed voltage source](#),” *Technical Physics Letters*, vol. 42, no. 4, pp. 384–386, 2016.

- [115] U. Fano, “[Effects of Configuration Interaction on Intensities and Phase Shifts](#),” *Phys. Rev.*, vol. 124, pp. 1866–1878, Dec 1961.
- [116] K. Qu and G. S. Agarwal, “[Fano resonances and their control in optomechanics](#),” *Phys. Rev. A*, vol. 87, p. 063813, Jun 2013.
- [117] D. A. Rodrigues, “[Fano-Like Antiresonances in Nanomechanical and Optomechanical Systems](#),” *Phys. Rev. Lett.*, vol. 102, p. 067202, Feb 2009.
- [118] H. Hamber and S. Liu, “[On the quantum corrections to the newtonian potential](#),” *Physics Letters B*, vol. 357, no. 1, pp. 51 – 56, 1995.
- [119] J. F. Donoghue, “[Leading quantum correction to the Newtonian potential](#),” *Phys. Rev. Lett.*, vol. 72, pp. 2996–2999, May 1994.